UNIVERSITY OF THE WESTERN CAPE

MAGISTER SCIENTIAE

The Effects of Environment on radio-loud AGN Activity in Stripe 82

Author:
Sthabile Kolwa

Supervisors:
Prof. Matt JARVIS
Dr Kim MCALPINE

A thesis submitted in fulfilment of the requirements
for the degree of Magister Scientiae

in the

UWC Astrophysics Group
Department of Physics

June 2016

Keywords

Catalogues - galaxies
Radio continuum - galaxies
Accretion-disk physics
Black-hole physics
Evolution - galaxies
Environment - galaxies
Surveys - galaxies
Active - galaxies
Photometry - infrared
Statistics - galaxies

Declaration of Authorship

I, Sthabile Kolwa, declare that *The Effects of Environment on radio-loud AGN Activity in Stripe 82* is my own work, that it has not been submitted for any degree or examination in any other university, and that all the sources I have used or quoted have been indicated and acknowledged by complete references.

Full name: Sthabile Kolwa

Signed:

Date:

"Sanity is not statistical."

George Orwell in his novel, *Nineteen Eighty-Four*

UNIVERSITY OF THE WESTERN CAPE

Abstract

Natural Sciences
Department of Physics

Magister Scientiae

The Effects of Environment on radio-loud AGN Activity in Stripe 82

by Sthabile Kolwa

We investigate the link between environment and radiative accretion efficiency using a sample of 8946 radio-loud AGN detected at $1-2$ GHz in the *SDSS Stripe 82* region. We quantify their environments using the surface-density parameter, Σ_{N}, which measures galaxy density based on distances to N^{th} nearest neighbours. Comparing Σ_2 and Σ_5 between AGN and control galaxies, we obtain relative densities that quantify the degree of galaxy clustering around each AGN. Using this, we examine the relation between density and the HERG-LERG dichotomy (accretion-modes) classified using a 1.4 GHz luminosity ($\mathrm{L}_{1.4\mathrm{GHz}}$) threshold. Our results indicate that, in the low-redshift interval ($0.1 < z < 0.2$), LERGs occupy environments denser than the field. At intermediate redshifts ($0.2 < z < 1.2$), both LERGs and HERGs occupy regions denser than the field. Spearman's rank tests show that correlations between density and $\mathrm{L}_{1.4\mathrm{GHz}}$ in both redshift intervals are weak. We conclude that the absence of a strong correlation is confirmation of the idea that galaxy density plays a more secondary role on AGN activity and also, accretion-mode classification (both measured using $\mathrm{L}_{1.4\mathrm{GHz}}$). It is likely that the rate of gas accretion or properties of galactic-scale magnetic fields correlate more strongly with $\mathrm{L}_{1.4\mathrm{GHz}}$, hence being primarily influential.

Acknowledgements

Thank you to the SKA Division of the National Research Foundation for funding my studies continuously for five years and counting. Dr McAlpine, your attention to detail is superb, you're a champion. Prof Jarvis, thanks for the trip to Oxford and all the wisdom that you have shared. Mother and family, thank you for your continual support.

Contents

List of Figures

List of Tables

Abbreviations

2MASS	**2** **M**icron **A**ll **S**ky **S**urvey
AGN	**A**ctive **G**alactic **N**ucleus
DR	**D**ata **R**elease
FIRST	**F**aint **I**mages of the **R**adio **S**ky at **T**wenty centimetres
HERG	**H**igh **E**xcitation **R**adio **G**alaxy
JVLA	Karl G. **J**ansky **V**ery **L**arge **A**rray
LERG	**L**ow **E**xcitation **R**adio **G**alaxy
NVSS	**N**ational Radio Astronomy Observatory **V**ery Large Array **S**ky **S**urvey
SCR	**S**earch **C**one **R**adius
SDSS	**S**loan **D**igital **S**ky **S**urvey
UKIRT	**U**nited **K**ingdom **I**nfra**R**ed **T**elescope
UKIDSS	UKIRT **I**nfrared **D**eep **S**ky **S**urvey
UV	**U**ltra**v**iolet
WISE	**W**ide-field **I**frared **S**urvey **E**xplorer

Chapter 1

Introduction

In this introductory chapter, we outline the goals of this work and their link to previous studies on AGN environments. Our own study places particular focus on the influence of environment on nuclear activity in the radio continuum which spans a frequency-range of $10^7 - 10^9$ Hz. The method for data analysis is explained and a history of radio galaxies is given. In addition to this, we highlight the importance of radio observations for AGN studies and the value of multiwavelength data for probing different structural components of AGN. The *Unified AGN Model* explains the emergence of various AGN classes. We describe it and also discuss the standard for quantifying radio-loudness. We also define accretion-mode dichotomy and detail attributes of the two specific AGN classes it refers to. These are the high-excitation and low-excitation radio galaxies (HERGs and LERGs), sometimes called radiative-mode and jet-mode galaxies. We summarise research that contextualises the question of whether a causal link between environments of AGN and their nuclear activity exists. Before concluding the chapter, we explain how WISE photometry can be useful for classifying radio sources with sufficient circumnuclear dust.

1.1 Overview

We aim to study the relation between accretion-rate in active galactic nuclei (AGN) and galaxy density. Accretion, in this context, refers to the collapse of gas onto accretion disks encircling central supermassive black-holes (SMBHs) in radio galaxies (Urry and Padovani, 1996). Gravity exerted by a SMBH attracts gas, causing it to fall into its potential well, forming an accretion disk as a result of angular momentum conservation. During collapse of a gas cloud, angular momentum is lost. To conserve this quantity, it increases elsewhere in the system. The result is that angular momentum is carried away from the central rotation axis, forming a disk. The conservation principle is obeyed because some of the gas particles in the system orbit at larger radii than before to compensate for the initial angular momentum loss. Matter in the disk is heated as a result of viscosity. This leads to thermal energy from the accretion disk ionizing neutral hydrogen (HI) in the gaseous medium, liberating electrons that interact with galactic magnetic fields. Electrons then undergo centripetal acceleration around magnetic field lines producing radio emission which contributes to a synchrotron spectrum that peaks in the radio continuum (Antonucci, 1993).

The radio-selected sources we study here are classified under accretion-mode dichotomy. This is a classification scheme that describes radio galaxies as being either HERGs or LERGs (jet or radiative-mode). Their classification depends largely on spectral-line measurements. One of the important lines for this is [OIII] (Buttiglione et al., 2010; Jackson and Rawlings, 1997). In HERGs, equivalent- widths of [OIII] are considerably broader than they are in LERGs. Another distinguishing factor is the Eddington-scaled mass accretion rate which is greater in HERGs than it is in LERGs. HERG accretion rates are $1 - 10\%$ the Eddington rate while LERG accretion is, generally, $< 1\%$ of this (Best and Heckman, 2012; Heckman and Best, 2014).

The rate of gas accretion onto the disk around a SMBH is directly proportional to radiative accretion efficiency which is the conversion rate of gas into energy that can be measured as a radio-flux density. We quantify this process by differentiating the mass-energy equivalence principle in a non-relativistic reference frame (where $v \ll c$) i.e. $E = Mc^2$ (Einstein, 1905). We then substitute $L = \dot{E}$, knowing that luminosity is a rate of energy transfer. The result is equation 1.1 which contains the radio-luminosity (L_R) and mass accretion rate ($\dot{M}_{acc}$). Radiative efficiency is denoted by ϵ and light-speed by c.

$$L_R = \epsilon c^2 \dot{M}_{acc} \tag{1.1}$$

This proves that the radiative efficiency or nuclear activity of an AGN can be approximated via its radio-luminosity. Knowing this relation, we are able to examine the correlation between AGN activity and measurable aspects of an AGN's environment. Several independent but often causally connected factors within this environment may influence AGN nuclear activity. In this study, we consider only one of these: the proximity of galaxies with respect to one another or the galaxy density. To measure this, we use the surface-density parameter (Σ_N) defined in equation 1.2. In this expression, d_N is distance to the N^{th} nearest companion to a galaxy for which surface-density is measured (the target galaxy). N is the total number of galaxies enclosed within a circular projected area on the sky in which surface-density is quantified (Dressler, 1980).

$$\Sigma_N = N/\pi d_N^2 \tag{1.2}$$

Surface-density parameter can be used to measure the galaxy density. This is just one way of quantifying the environment. There are other methods and each probe a different attribute of a galaxy's medium. It is, generally, likely that more than one factor in the environment can cumulatively impact the evolution of an AGN. Hence, looking for a direct correlation between accretion-mode and density without adding constraints to other factors related to the environment may lead to spurious results.

Other than galaxy density, the physical state of gas in an AGN's environment is likely to influence the accretion rate. A cold and dense gas supply facilitates efficient radiative accretion and enhances nuclear activity in radio AGN (Sabater et al., 2013). In some cases, the availability of cold gas causes an upsurge in accretion rate that can, over time, transform a LERG into a HERG (Janssen et al., 2012). The opposite case occurs when hot and diffuse gas from the intracluster medium fuels the AGN, slowing accretion. This is speculated to be the reason for less efficient accretion rates in LERGs (Hardcastle et al., 2007). What this evidence collectively suggests is that gas accretion in AGN (referred to as a secular process) is likely a primary trigger and sustaining fuel source for AGN activity. Whereas density and one-on-one galaxy interactions carry a more secondary influence.

A causal link between mergers and secular processes has been suggested (Mauch and Sadler, 2007a). Theory postulates that cold gas is driven toward the nuclear region as a result of tidal disturbances during a galaxy interaction. Gas infall then increases radiative accretion efficiency. In such a scenario, more than one environmental factor is seen to affect AGN accretion. Yet once again, secular process play a primary role.

In addition to this, galaxy density and stellar mass are strongly correlated (Park and Choi, 2009). In this study, when testing for correlations between environment and radiative accretion efficiency, we constrain stellar mass. We do this to prevent the mass-density relation from being embedded into our results.

We compate our findings to those from previous studies on AGN environments. When doing this, we take into account the extent to which surface density is measured. It is possible that measured galaxy density differs depending on the extent or distance scale on which it is measured. In the case of surface-density parameter, this is extent is determined by N in equation 1.2.

The wavelength range used to select AGN may also bias a sample. This is due to the fact that components of an AGN emit differently, depending on their physical nature. Thus, it is likely that similar types or classes of AGN emerge when selected in specific wavelength ranges. In other words, X-ray, optical and radio AGN may each represent different types of AGN thus we separate them.

We select our AGN in the radio continuum due to the fact that the detrimental effects of dust are reduced in the radio while optical wavelengths experience a higher degree of dust absorption. Also, LERGs are only identifiable in radio wavelengths as a result of their radio emission (Heckman and Best, 2014) and the relatively low flux density of their emission and ionisation features which makes their optical spectra appear almost featureless (Best, 2004). Since both accretion-modes are radio galaxies, the radio continuum is probably the best way to select them.

This kind of classification is done in Sabater et al. (2013) where a sample of SDSS galaxies are classified as optical and radio AGN. Quantifying the environments of both types in terms of density, the study finds that the optical AGN favour less dense environments than the radio AGN.

LERGs are only identifiable by their radio emission making them comparable to the radio AGN in Sabater et al. (2013). HERGs, however, are detectable in the radio and optical continua. In this sense, they are similar to the optical AGN defined by Sabater et al. (2013). If this comparison holds true for the environments of HERGs and LERGs, we should expect HERGs to occupy less dense regions than LERGs.

We may not observe this, however, and it could be because this comparison is simply incorrect. Another reason for our results contradicting previous studies is redshift. Since redshift intervals represents evolutionary epochs, comparing galaxies at different redshifts is the same as comparing them at different stages of their evolution. There is a definite possibility that the relation between environment and nuclear activity indeed evolves with cosmic time.

1.2 Brief History of AGN

The establishment of AGN as a class of astrophysical objects was a gradual process, spurred on by the identification of unusual features in galactic spectra. Observations that ultimately led to their discovery were the spectral studies of galaxies like NGC 1068. Astronomers, Fath (1909) and Slipher (1917), worked on galaxy spectra with broad emission and absorption features and found them unusual. They were unlike the spectra of regular spiral galaxies that only featured stellar absorption lines (Shields, 1999).

Decades later, in 1943, Seyfert would undertake a spectral study of six spirals with highly excited nuclear emission. In these, Balmer lines were measured to be wider than those of diffuse nebulae (HII regions). If Doppler broadening widened the Balmer lines, it would mean that, on average, photons in these spirals were more energetic than those in HII regions. This could not be possible. Hence, some other physical mechanism had to be responsible for the measured line-widths. The objects he found also had unusually high surface brightnesses. They given the name *Seyfert galaxies*, and became known as a distinct type of AGN.

The discovery of more AGN classes came about after the birth of radio astronomy which is now a fundamental observational tool for AGN studies. One could say that it began with Karl Jansky at the Bell Telephone Labs. He was the first to measure radio emission from Sgr A* (the Galaxy's nucleus) in 1935. It then followed through with Grote Reber who built a reflecting radio receiver in his back-yard, using it to conduct a 160 MHz survey showing evidence of radio emission from Cygnus and Cassiopeia i.e. Cyg A and Cass A (Shields, 1999).

As observational radio astronomy gained speed, theoretical ideas to explain the production of radio emission from AGN were postulated. Alfvén and Herlofson (1950), suggested that cosmic-ray electrons interacting with magnetic fields emit radio waves via synchrotron processes (Burbidge, 1959). After this, came the *twin exhaust model* of Blandford and Rees (1974) which sought to explain bipolar jets which have yet to be fully understood.

Mounting evidence for the existence of radio galaxies came in 1954 when Cassiopeia and Cyg A were found to coincide positionally with known galaxies (Baade and Minkowski, 1954). In 1963, these radio sources were named 3C 48 and 3C 273[1]. Although their spectra seemed to have stellar origins, their high redshifts, z = 0.37 and z = 0.16 respectively, suggested otherwise. Sources with optical magnitudes of ~ 12.6 (for 3C 273) and ~ 16 (for 3C 48) located at Mpc-scale distances could not be of stellar origin. They were suggested to be distant galaxies that were generating energy at vast rates, objects we call *active galaxies*.

Other observational evidence for similar galaxies was given in the form of point sources on photographic plates. These sources appeared optically bluer than stars and were found to overlap with sky positions of already known 3C Catalogue radio sources (Ryle and Sandage, 1964). Collectively, they went on to be called *quasi-stellar objects* or quasars and formed their own AGN class.

Today, Seyferts and quasars amongst other similar types of galaxies fall under the term *AGN*. In addition to this, some universal agreement on the structure of AGN as an entire group of astrophysical objects has been reached (described fully in Section 1.3.1). It is referred to as the *Unified AGN Model*. Although the physics to thoroughly explain their powering mechanisms has not yet been formulated, the acceptance of this unifying picture is motivated by the fact that, as yet, no better alternatives have been put forward to explain what physical structures are responsible for AGN observations (Schneider, 2006).

Multiwavelength studies are useful for probing various attributes of AGN structures. For instance, we detect synchrotron processes and accretion disk variability in the radio and X-ray continua. X-ray variability is used to measure the sizes of nuclear regions in active galaxies (Gaskell and Klimek, 2003). From optical surveys, we obtain galactic spectra that reveal chemical signatures. In the mid-IR, nuclear dust re-emission is detected while the far-IR probes star-formation.

---

[1] 3C is the abbreviation for the Third Cambridge Catalogue, a 159 MHz survey (in 1959) which was, subsequently, revised at 178 MHz (in 1962).

1.3 AGN Characteristics

Here, we detail the physical components of AGN and discuss methods for detecting each. We also describe the Unified AGN Model which suggests that AGN, in general, share a common structure. The observation of different classes of AGN is a result of viewing angle. We describe differences between broad and narrow-line regions in AGN. We also explain the effects of absorption which obscures the broad-line region in some classes of AGN (Antonucci, 1993).

1.3.1 Unified AGN Model

AGN consist of SMBHs with masses, $\mathrm{M_{BH}} \sim 10^6 - 10^{10}\ \mathrm{M}_\odot$. This range is based on limits brought about by observations. At low enough redshifts, where gas kinematics are adequately resolved, Doppler line-broadening in optical spectra help constrain $\mathrm{M_{BH}}$. With line-widths being proportional to gas velocity, $\mathrm{M_{BH}}$ can be estimated via equation 1.3 where $\mathrm{v_{eff}}$ is the effective gas velocity, estimated from half-intensity levels of spectral lines (Dibai, 1977).

Reverberation-mapping in the broad-line region (BLR) also constrains $\mathrm{M_{BH}}$ (Khorunzhev et al., 2012). Although, not as thorough as other methods for estimating $\mathrm{M_{BH}}$, the fundamental plane provides a reasonable correlation between $\mathrm{M_{BH}}$, X-ray luminosity ($\mathrm{L_X}$) and radio-luminosity ($\mathrm{L_R}$) (Merloni et al., 2003).

$$\mathrm{M_{BH}} = \mathrm{v_{eff}^2 R/2G} \tag{1.3}$$

Accretion describes the infall of gas into a SMBH's gravitational potential well. During this process, angular momentum loss by gas particles spiralling in occurs. This loss is compensated by an increase in angular speeds of gas particles further away from the axis of the disk's rotation. As angular momentum is transported outwards, an accretion disk forms around the central SMBH. Hereafter, gas from the AGN's surrounding medium continues to fall onto the accretion disk, fuelling the system's radiative processes (Abramowicz, 2013).

X-ray continuum emission originates from the accretion disk and corona. The corona is an optically thin medium that envelopes outer layers of the disk and undergoes heating through viscous damping. This process facilitates energy exchanges between both disk and corona. A corona heated above a specific threshold will transition into a hot plasma in which soft X-ray photons experience inverse Compton scattering which explains the hard X-ray emission observed (Liu et al., 2002).

Viscous heating alone does not fully explain X-ray emission in AGN. Coronal heating through reconnecting magnetic-field lines which dissipate energy into the corona has been suggested as a source. While observations still provide limited resources for understanding X-ray AGN emission, numerical models of accretion disks and the corona have been useful in developing theory on this matter (Liu et al., 2015).

In the optical, AGN spectra reveal specific signatures in their ionisation and emission lines that make density, temperature and sizes of gas cloud regions surrounding the AGN measurable. In relation to equivalent-widths (EWs) of these features, we use the general terms *broad* and *narrow* to specify where spectral features have been widened by pressure, Doppler effects, etc. In AGN, there are distinct broad and narrow line regions (BLR and NLR) (as seen in Fig. 1.1) where spectral line fluxes of each type originate. Generally, EW of lines increase closer to the SMBH due to Doppler (thermal) line-broadening brought about by energetic gas particles moving at relatively high speeds. In such observations, the full-width half maxima (FWHM) of emission and ionisation features e.g. CIV, Lyα, [OIII], MgII, Hα in the UV-optical continuum of AGN have revealed broad velocity line measurements of $\sim 10^3 - 10^4$ km/s. Narrow line velocities are measured between $\sim 300 - 500$ km/s (Ghisellini, 2012).

Spectral lines result from electronic transitions in atomic gas within an AGN's surrounding medium rather than its accretion disk. Doppler shifting of spectral lines features would be observed if they originated from the disk given that it rotates. The spectral features would then be *double-horned*. AGN spectra featuring only narrow emission lines are called type 2 whereas type 1 AGN spectra contain both broad and narrow features. Forbidden transitions e.g. [OIII] have their origins in the NLR where gas densities of

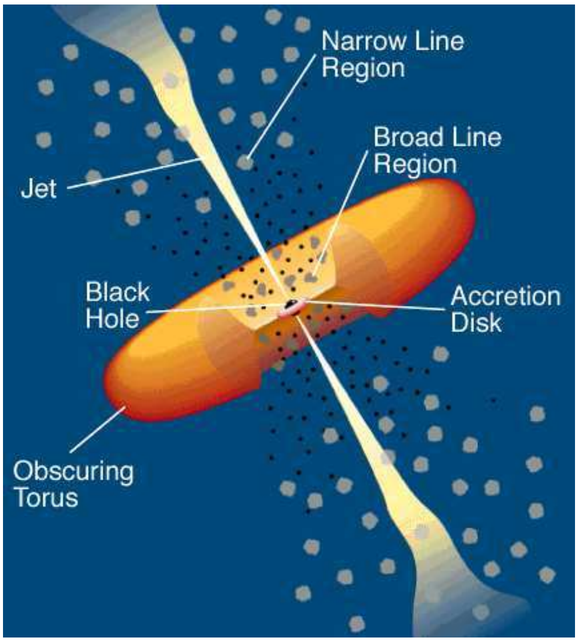

Figure 1.1: Schematic of a typical AGN. The BLR region exists in closer proximity to the central SMBH than the NLR. Gas collapsing onto the accretion disk fuels the AGN (secular process) (Urry and Padovani, 1996).

$\sim 10^3$ cm^{-3} are measured i.e. low gas-density regions. In comparison, gas densities in the BLR measure $10^9 - 10^{11}$ cm^{-3} (Ghisellini, 2012).

The locations of the BLR and NLR in an AGN with respect to an observer's viewing angle result in the emergence of various AGN classes. This concept is called the Unified AGN Model which suggests that all AGN share a similar structure but belong to classes as a result of their orientation with respect to the observer's line-of-sight. Depending on the viewing angle, the BLR can be obscured by a circumnuclear dusty torus (shown in Fig. 1.1). Although obscured, the BLR can still be seen when BLR photons undergo Thomson scattering. This refers to the process of free electrons being scattered by photons in the ionized BLR region. Scattering angles of $\sim 90°$ from the initial trajectories occur in order for photons to be observed (Antonucci and Miller, 1985).

The torus of an AGN typically measures $< 1 - 2$ pc in diameter. This fact has, however, yet to be confirmed through direct observations from a ground-based telescope. Ideally, a resolution of $\lesssim 0''.33$ would be adequate to perform this task (Mason, 2014). Despite this limitation, reverberation-mapping has been effective at determining torus radii. This involves measuring the time-delay (or lag-time) of photons from the nucleus that are

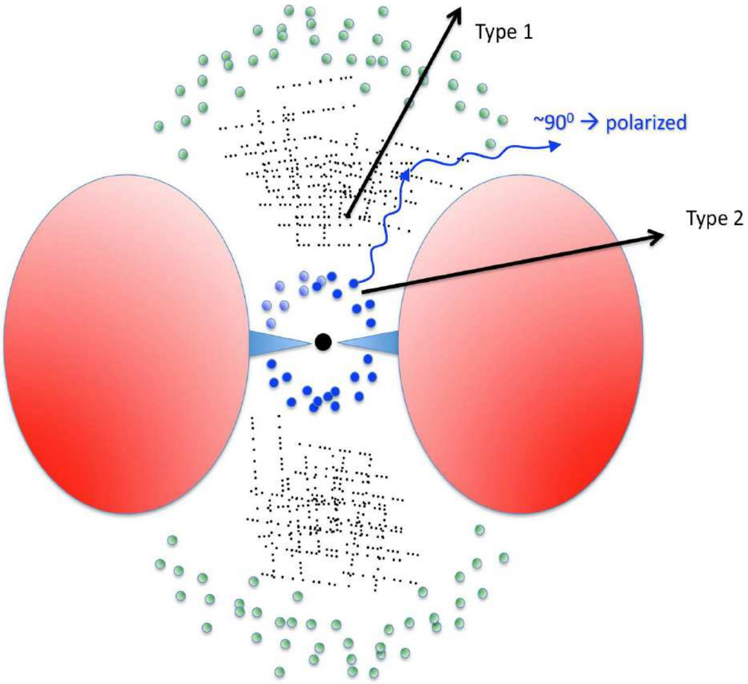

FIGURE 1.2: A distinguishing attribute between type 1 and 2 AGN is dust-obscuration of the BLR (blue dots). The dust exists as a torus (in red) that is optically thick to radiation from the BLR. Polarized BLR flux is observed when BLR photons are scattered by free electrons (black dots) into orientations $\sim 90°$ from their initial trajectories (Ghisellini, 2012). The NLR is not obscured by dust.

refracted in the BLR. This lag-time, denoted by τ, provides approximates the radius of the BLR using the relation, $\tau = \mathrm{R}/\mathrm{c}(1+\cos\theta)$. Lag-time has been estimated using optical and near-IR observations of nearby Seyfert 1 galaxies. In these cases, the relation between lag-time and optical-luminosity was found to be, $\tau \propto \mathrm{L}^{0.5}$ (Suganuma et al., 2006).

Near and mid-IR interferometry have also been used to resolve the AGN torus in sources such as NGC 1068, a Seyfert 2 located at a 14.4 Mpc distance. This was done using the MID-infrared Interferometric Instrument (MIDI) and Very Large Telescope Interferometer (VLTI). The resolved torus measured 2.1 pc in height and 3.4 pc in diameter. Interferometry provides a more direct method for both observing and measuring the size of a torus than reverberation-mapping (Jaffe et al., 2004).

1.3.2 Radio-Loudness

The sample we examine in this work consists of sources detected in the $1-2$ GHz range (in the radio continuum). We argue that this sample consists primarily of AGN because of the quantity of sources with 1.4 GHz luminosities $> 10^{23}$ W/Hz. This argument is based on evidence which states that for $\mathrm{L}_{\mathrm{NVSS}} > 10^{23}$ W/Hz[2], most radio sources at redshifts $\lesssim 0.2$ are AGN rather than star-forming (SF) (Mauch and Sadler, 2007b).

We call our sources *AGN*, a term that refers to a class of objects with inhomogeneous features (Czerny et al., 2005) but unified by a common structure. Such inhomogeneities emerge in designations such as radio-loud (RL) and radio-quiet (RQ) which refer to a source's level of radio-loudness and are determined via the R-parameter. This is defined as a ratio of the the 5 GHz (radio) fluxes to 4400Å B-band (optical) i.e. $\mathrm{R} = \mathrm{F_r}/\mathrm{F_o}$ (Ishibashi and Courvoisier, 2011). In light of this, a source is classified as RQ for $\mathrm{R} = 0.1 - 1$ and RL when $\mathrm{R} = 10 - 100$ (Kellerman et al., 1989).

The parameter, $\mathrm{R_X}$, is also used to distinguish RL from RQ AGN. The definition for this is $\mathrm{R_X} = \nu\ \mathrm{L}_\nu\ (5\ \mathrm{GHz})/\mathrm{L}(2-10\ \mathrm{keV})$ (Terashima and Wilson, 2003). $\mathrm{R_X}$ correlates well with the R-parameter and is useful in cases where dust reduces optical flux through absorption. Since, the torus is optically thin to the X-ray continuum, $\mathrm{R_X}$ provides a suitable alternative for measuring the radio-loudness of obscured (type 2) AGN. The boundary between RL and RQ AGN is drawn at the $\log \mathrm{R_X} = -2.755 \pm 0.015$ below which Seyfert 1's (RQ galaxies with $\mathrm{R} < 1$) dominate. Above this threshold, low-luminosity RL AGN are in the majority (Panessa et al., 2007).

---

[2] The NVSS stands for the NRAO VLA Sky Survey which is a 1.4 GHz imaging survey conducted.

1.4 Accretion-Mode Dichotomy

Radio sources can be classified by way of the accretion-mode dichotomy. This is a classification scheme that describes the attributes of two distinct classes of radio galaxies (RGs). It also forms an integral part of our analysis in which we examine the link between accretion-mode and galaxy density. We refer to these two classes of AGN as high and low excitation radio galaxies (HERGs and LERGs) based on relative gas excitation levels in each (Best and Heckman, 2012). Schematic drawings of each type are shown in Fig. 1.3.

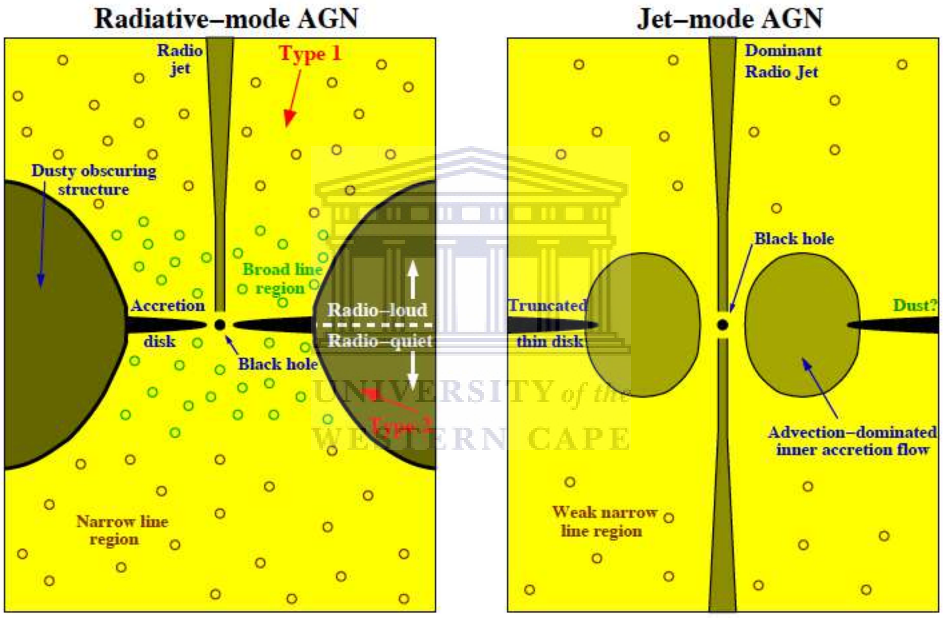

FIGURE 1.3: Schematic drawing of radiative-mode (HERGs) and jet-mode (LERGs). Radiative-mode sources feature accretion disks, NLRs and BLRs that may be obscured by a dusty torus. When RL, radio jets are observed in HERGs. RQ HERGs do not feature jets. LERGs have dominant radio jets and are relatively devoid of dust. A thin, truncated accretion disk exists and local gas is only weakly ionized.

The upper limit for accretion onto the disk is set by the errors on observed mass accretion rates. We quantify these rates relative to the Eddington accretion limit ($\dot{\mathrm{M}}_{\mathrm{Edd}}$). This defines the point at which a disk becomes unstable and susceptible to disintegration due to radiation pressure i.e. when $\mathrm{M} > \dot{\mathrm{M}}_{\mathrm{Edd}}$. Below this limit, of course, stable mass accretion continues. Hence, measured $\dot{\mathrm{M}}$ is generally expressed as a fraction of $\dot{\mathrm{M}}_{\mathrm{Edd}}$.

HERGs are sometimes referred to as radiative-mode, cold-mode or quasar-mode galaxies. They are described as 'fast accretors' due to their relatively high accretion rates. In general, accretion efficiency is quantified as a fraction of the Eddington-scaled accretion rate: $\dot{\mathrm{M}}_{\mathrm{Edd}}$. In HERGs, accretion onto the SMBH ($\dot{\mathrm{M}}_{\mathrm{BH}}$) is $0.01 - 1\dot{\mathrm{M}}_{\mathrm{Edd}}$. Cold, dense gas is considered a source for collapsing gas in these AGN (Best and Heckman, 2012; Heckman and Best, 2014).

LERGs can also be called jet-mode, hot-mode or radio-mode galaxies. Their accretion rates are $\dot{\mathrm{M}}_{\mathrm{BH}} < 0.01\dot{\mathrm{M}}_{\mathrm{Edd}}$, indicative of less efficient accretion. This makes them 'slow accretors' in comparison (Best and Heckman, 2012). The fuel supply in LERGs is speculated to originate from diffuse and hot intra-cluster media. This concept, however, has yet to be confirmed due to the fact that diffuse gas is, at present, difficult to detect (Hardcastle et al., 2007).

Black-hole and stellar mass (M_{BH} and M_{*}) differ between HERGs and LERGs. On average, M_{BH} of hot-mode RGs exceed those in cold-mode RGs by a small margin, as Fig. 1.4 suggests. LERGs are redder (optically) than HERGs for sources with similar masses and radio-luminosities. This is likely to be a result of ongoing SF in HERGs. We also know that LERGs have comparatively larger M_{BH} and M_{*} than HERGs for low-redshift radio sources. Optical emission lines have also been found to be more prominent in HERGs than LERGs (Best and Heckman, 2012).

These arguments are strengthened by observations made before accretion-mode was established. Sources with strong emission features were observed as low-luminosity, optically blue galaxies, with low velocity dispersions (σ_{v}) and mass-to-light ratios (M/L). These galaxies sources contained young stellar populations and had low M_{BH} and M_{*} compared to those with weak lines in their emission spectra (Smith et al., 1990). It is likely that these strong-line blue galaxies are, in fact, HERGs with their weak-line counterparts being LERGs.

Equivalent-widths (EWs) of spectral lines are used to determine accretion-mode. In the titles, HERG and LERG, high and low-excitation refer to the strength (determined by the EW) of the ionisation and emission lines in galactic spectra. HERGs feature narrow and strong ionisation line because gas is ionised to a higher degree (larger EW for ionisation

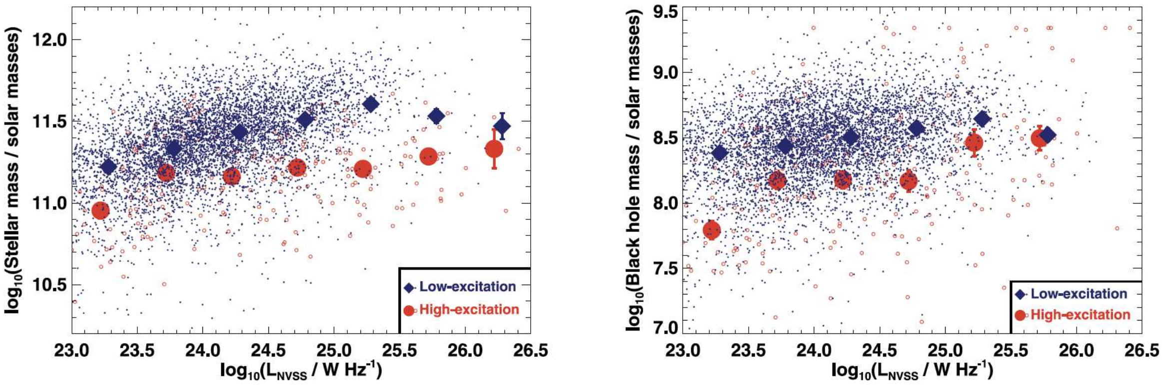

FIGURE 1.4: Stellar and BH mass (M_* and M_{BH}) as functions of NVSS radio-luminosity (L_{NVSS}). High and low-excitation refer to HERGs and LERGs, respectively. The red and blue points denote mean mass per L_{NVSS}-bin. Overall LERG M_{BH} and M_* exceed those of HERGs over the $10^{23} - 10^{26}$ W/Hz interval (Fig. 7 in Best and Heckman, 2012).

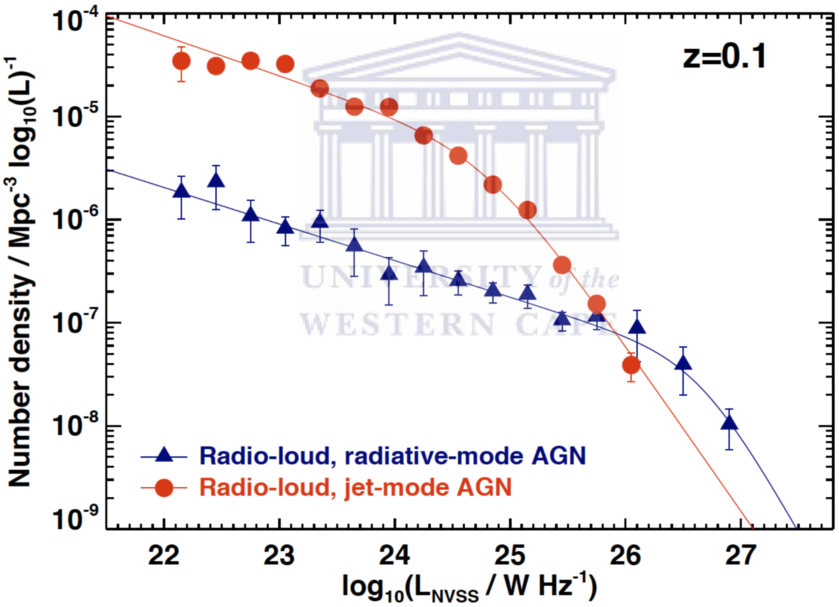

FIGURE 1.5: The NVSS local radio-luminosity function derived for HERG and LERG populations separately. LERGs dominate the population for $L_{NVSS} \lesssim 10^{26}$ W/Hz. Above this limit, HERGs become more prevalent (Fig. 11 in Heckman and Best, 2014).

features) than it is in LERGs. In LERGs, spectral lines are weak and sometimes even absent (Heckman and Best, 2014). It turns out that for the weakest radio sources, found at the lower limits of the radio continuum, classification by way of ionisation lines may not be possible at all. This is because spectral line strength is proportional to radio flux (Rawlings and Saunders, 1991; Tadhunter et al., 1998).

An example of ionisation lines being used to classify radio sources is given in Laing et al. (1994). In this work, a 3CR radio AGN sample is classified into HERGs or LERGs using line flux ratios. For a source to be a HERG, the conditions [OIII]5007/H$\alpha > 0.2$ and EW$_{\mathrm{[OIII]}} > 3$Å must be met. Otherwise, radio sources are classified as LERGs. A similar classification scheme is given in Buttiglione and Capetti (2010) who define an excitation index (EI). In this, EI $= 0.95$ marks an approximate dividing limit between HERG and LERG populations. For the 2Jy radio source population in Tadhunter et al. (1998), low-excitation sources are distinguishable from other sources in terms of their [OIII]5007/[OII]3727, [OIII]5007/L$_{\mathrm{R}}$ and [OII]3727/L$_{\mathrm{R}}$ line ratios[3].

To carry out a full classification of the Sloan Digital Sky Survey (SDSS) radio sources in Best and Heckman (2012), a 5-tiered classification scheme based on findings in the literature described above is formulated. In some cases, all the ionisation lines needed to classify sources may not be present hence the need for a multiple-level classification. When applied to Best and Heckman (2012) SDSS radio sources, the 5-tiered scheme proves to be consistent with EI and EW$_{\mathrm{[OIII]}}$ of literature diagnostics (shown in Fig. 1.6). There is, however, contamination of LERGs along the EW$_{\mathrm{[OIII]}} = 3$Å line. In terms of the EI = 0.95 threshold suggested by Buttiglione and Capetti (2010), however, the classification is in good agreement.

In the same SDSS radio source sample (Best and Heckman, 2012), LERGs dominate the population for 1.4 GHz radio-luminosities $< 10^{26}$ W/Hz (shown in Fig. 1.5). Since LERG spectra often contain weak or absent spectral lines, the radio continuum is comparatively better at detecting them. HERGs can be selected in the optical and radio continua, however, due to the relative strength of their ionisation lines. Since dust is optically thin to radio wavelengths, synchrotron emission from these sources is still detected.

The difference in these two RG populations is also observed in their evolution. Changes in HERG and LERG populations with cosmic time have been quantified using V/V$_{\mathrm{max}}$ tests. When applied to the Best and Heckman (2012) radio source sample, results indicate that HERG fractions multiply with redshift for radio luminosities in the range, $10^{23} - 10^{27}$

---

[3] Next to the description of an ionisation line is its characteristic wavelength e.g. the [OIII]-line has a central wavelength of 5007Å. L$_{\mathrm{R}}$ is the radio-luminosity.

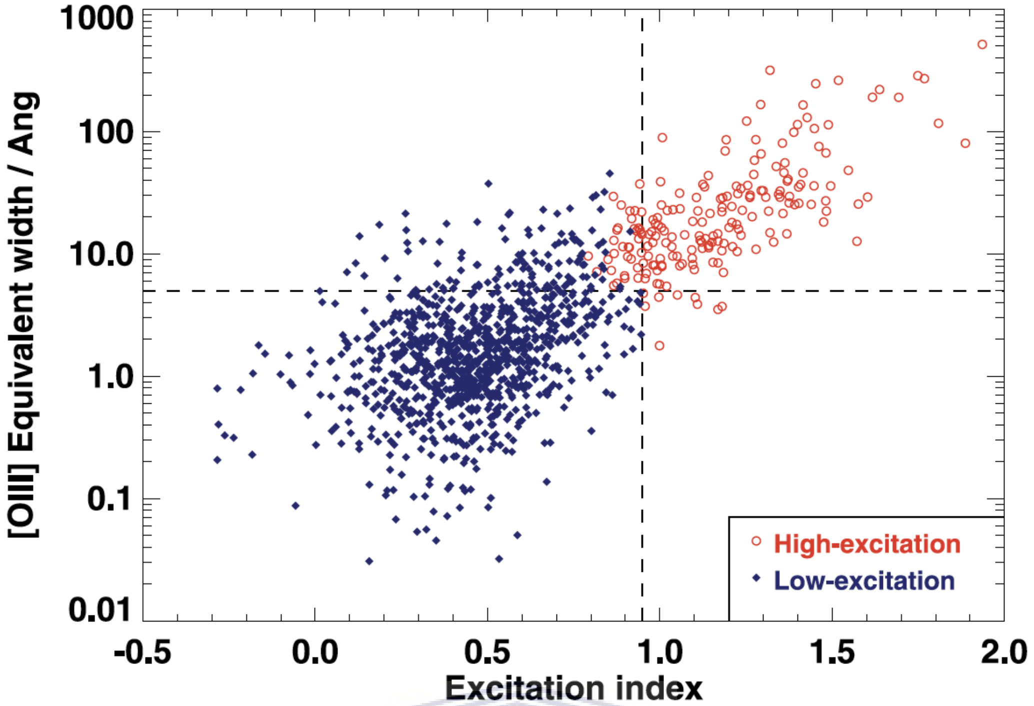

Figure 1.6: The $EW_{[OIII]}$-EI plane for SDSS radio sources characterised as HERGs (high-excitation) and LERGs (low-excitation). The classification is consistent with the EI = 0.95 threshold proposed in Buttiglione and Capetti (2010) (Fig. 1 of Best and Heckman, 2012)

W/Hz. LERG fractions, however, remain constant, indicating minimal evolution in these objects over a redshift range of $0.01 < z < 0.3$ (Best and Heckman, 2012).

1.5 AGN Environment

It is a known fact that the medium in which an AGN resides has some influence on it its observable attributes. In this work, we pay close attention to activity at the nucleus quantified by radio emission. Generally, more than one aspect of the environment may affect the evolution of an AGN simultaneously. For instance, secular processes (gas infall onto the accretion disk) and galaxy interactions (tidal disturbances) could mediate accretion rates in opposite ways. This may occur when collapsing gas is displaced by tidal forces exerted during a galaxy interaction.

The likelihood of galaxy interactions occurring sometimes depends on how clustered AGN environments are. This stems from the notion that the probability of galactic mergers increases when galaxies are in close proximity i.e. in high galaxy density environments (Coziol and Plauchu-Frayn, 2007). However, even in the absence of merger events, tidal effects can disrupt the gas and stellar distributions of interacting pairs (Toomre and Toomre, 1972; Farouki and Shapiro, 1981). Events such as these are predicted to either trigger or quench nuclear activity depending on the availability and distribution of gas (Karouzos et al., 2014).

On the contrary, in low galaxy density environments, tidal force strengths that exceed the expected pattern (linear trend between density and tidal force) have been observed (Verley et al., 2007). This implies that mergers and other galaxy interactions are also possible in voids or less clustered regions. Hence, a directly proportional relation between density and mergers does not always hold.

Another environmental influence is secular processes. This refers to the physical state and motion of gas in the local environment of an AGN. Theory has suggested that gas collapsing onto AGN accretion disks originates from either a hot extended intracluster medium or cold reservoirs located closer to an AGN. In accordance with accretion-mode, gas too may be dichotomous in its physical state being either hot and diffuse or cold and dense. Both forms of gas are understood to affect mass accretion rate and hence accretion efficiency differently (Hardcastle et al., 2007).

One main factor that differentiates galaxy interactions from secular processes is the spatial extent of their influence. Therefore, when looking at evidence of environment influencing AGN activity, it helps to consider the distance scale on which environment is quantified. This may define what attribute of the environment is ultimately measured.

When examining AGN environments, we make note of the wavelength range in which AGN are selected. This can determine what attributes of the AGN's structure are being probed. This is due to the fact that each AGN component emits uniquely in specific portions of the AGN's spectral energy distribution. This is elaborated on in Section 1.3. Hence, when comparing results from previous studies, we consider the wavelength ranges in which an AGN sample has been selected. Because there is a strong likelihood that objects selected differently belong to different classes of AGN.

1.5.1 Galaxy Interactions and AGN

Several instances of observational evidence have indicated that galaxy interactions may trigger nuclear activity in AGN. In addition to this, simulations have also been used to show how these interactions may lead to the formation of AGN and also fuel them throughout their life-spans.

Gas-rich mergers modelled by N-body simulations, in particular, have shown that tidal forces can drive collapsing gas to the central nucleus of a galaxy, leading to the formation of a bar. During this process, gas within the inner half of a galaxy's disk falls into the compact centre of its nuclear region (Barnes and Hernquist, 1991). More recently N-body and hydrodynamical simulations have further reinforced this idea (Newton and Kay, 2013; Barai et al., 2014).

In terms of optical observations, evidence has been put forward to support the idea that galaxy interactions are closely related to nuclear activity in AGN. We see this for, SDSS-selected AGN ($0.05 \leq z \leq 0.095$). When these sources are classified as Seyfert 1 and 2 (Sy 1 and 2) galaxies, they are found to reside in almost identical environments, in terms of large-scale density. On the same sample, a larger fraction of Sy 2 than Sy 1 galaxies are found in close-pair systems with radii, $r \leq 100$ kpc. What links mergers to close-pair separation is the fact that tidal forces become stronger with increasing distance proximity between two AGN. Since Sy 2's are more powerful radio emitters than Sy 1's, the fact that they are incident in pairs more often than Sy 1's may indirectly suggest a link between galaxy interactions (as traced by pair membership) and AGN activity (as measured by radio-luminosity) (Sorrentino et al., 2006).

Another set of SDSS AGN has provided a similar result, indicating that nuclear activity increases with pair proximity. We see this in Ellison et al. (2011) where the fraction of AGN (f_{AGN}) increases by a factor of ~ 2.5 for projected separations, $r_p < 40h_{70}^{-1}$ kpc (close companionship). A similar result has been obtained in Silverman et al. (2011). In this work, the f_{AGN} is greater by a factor of ~ 2.6 for AGN pair separations < 75 kpc and radial velocity offsets of $\Delta V_r \sim 500$ km/s (shown in Fig. 1.7).

On yet another sample of SDSS AGN ($0.02 \lesssim z \lesssim 0.14$), evidence presented that supports the idea that AGN activity is triggered by galaxy interactions (Hwang et al., 2012). Consistent with previous arguments, in Manzer and Robertis (2014) optical AGN ($0.01 < z < 0.2$) are found to have a 25% higher probability of residing in groups than in the field. This evidence supports the idea that local environment plays a role in AGN formation.

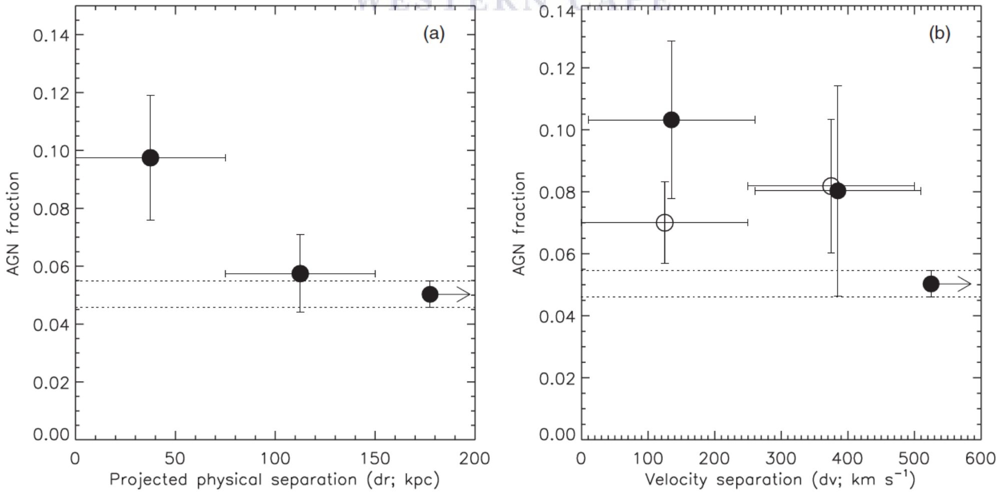

FIGURE 1.7: AGN fraction as a function of projected separation (in kpc) (left) and velocity (in km/s) (right) for zCOSMOS AGN pairs (Fig. 5 of Silverman et al., 2011).

AGN detection in the X-ray continuum is possible because of accretion disk heating (Reynolds, 2015). Hence, X-ray data provides another method for detecting AGN. Type 2 X-ray AGN (2$-$10 keV range) are similar to RL AGN in that both undergo fast accretion for sources at the low M_*-limit. These X-ray AGN are found to favour environments where mergers and interactions are more probable (Tasse et al., 2011), thus providing a link between mass accretion rate and environment.

All of the observations cited above suggest that galaxy interactions play somewhat of a role in sustaining and also sparking nuclear activity in optical and X-ray AGN. Most of the evidence in these cases has been given in the form of an association between AGN fraction and projected separations or galaxy density. If the quantity of AGN in a population increase with galaxy density, this implies that tidal forces may strengthen or initiate nuclear activity.

Evidence supporting the link between galaxy interactions and AGN activity is not always found, however. In Miller et al. (2003), the idea of mergers driving AGN activity of SDSS AGN in the redshift range $0.05 \leq z \leq 0.095$ is not favoured. Measured AGN fractions, in this case, require higher merger rates than what is measured or estimated by observations and models. This is seen in Fig. 1.8 where the AGN fraction remains constant with density. Hence, mergers are less likely to drive optical nuclear activity.

In some cases, major mergers have been found to affect only the most luminous AGN (10^{43} erg/s $< L_{bol} < 5 \times 10^{46}$ erg/s) for $z < 3$. This suggests that the AGN-merger relation only applies in special cases (Treister et al., 2012). AGN fractions in samples of disk galaxies ($1.5 < z < 2.5$) have been found to exceed those for spheroid galaxies. Based on the understanding that disk galaxies are less likely to have undergone interactions than spheroids, this evidence suggests that AGN are not always linked to tidal disturbances (Kocevski et al., 2012).

Comparisons between X-ray AGN and quiescent galaxies ($0.3 < z < 1.0$) have revealed little to no difference in distortion of galactic disks. This may be a result of a lack of recent mergers to alter the disk structure of these active galaxies (Cisternas et al., 2011).

Hence, as much as there is evidence to support the link between galaxy interactions and AGN, there is also a fair amount suggesting that no such link exists. It is also possible, however, that the disparate nature of results presented here may easily be a result of

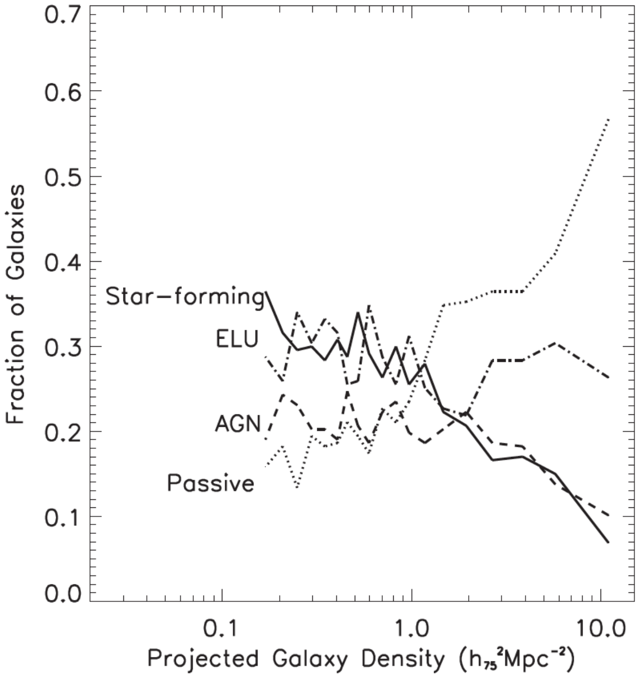

FIGURE 1.8: Galaxy fraction as a function of projected density in h_{75}Mpc^{-2}. AGN fraction remains most constant with density. Passive and SF galaxies fractions increase toward over-dense and under-dense environments, respectively (Fig. 8 of Miller et al., 2003).

selection effects based on wavelength-detection of AGN samples and also the different methods for environment measure being used.

1.5.2 Secular Processes and AGN

Other than galaxy interactions, gas supplied by an AGN's environment may affect the rate of accretion or nuclear activity measured. Although these two environmental attributes are probed differently, it is possible that they are causally linked or work in tandem. Some theories suggest that the physical state of gas affects the rate of gas infall, implying that these processes are not mutually exclusive.

This idea is tested in Sabater et al. (2015), where the local galaxy density and PCA2 parameter (a tracer of galaxy interactions) quantify environment. Optical AGN activity, here, is traced by the median $\log_{10}(L_{[OIII]}/M_{BH})$. Since sSFR and M_* depend on environment, they are both constrained. This is accomplished by creating sub-samples for combinations of high and low sSFR and M_* (as shown in Fig. 1.8). AGN activity as a function of both density parameters is examined. Results of this depict an anti-correlation between AGN activity and environment. This may indirectly suggest that AGN activity is perhaps affected, to a larger degree, by cold gas accretion instead.

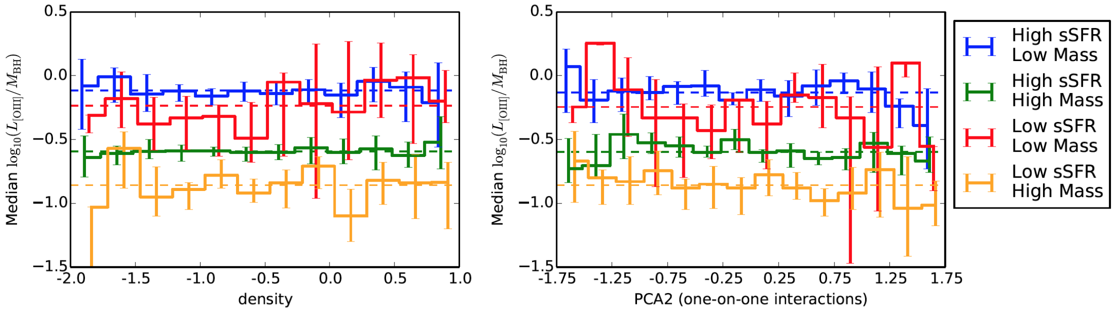

FIGURE 1.9: AGN activity is denoted by median log $L_{[\mathrm{OIII}]}/M_{\mathrm{BH}}$. Environment is quantified by local galaxy density and PCA2. The blue, green, red and orange lines signify different combinations of sSFR and M_* (shown in the legend). Dashed lines for each of these represent the means in each case (Fig. 5 of Sabater et al., 2015).

In Sabater et al. (2013) environment is quantified using a local density parameter and tidal force estimator. In the results of this work, the optical AGN fraction (0.03 < z < 0.1) increases with decreasing density. For radio AGN, the opposite is found to be true. These results and others in the study collectively suggest that abundance of cold gas determines the level of nuclear activity. Also that the cold gas supply is largely controlled by the local galaxy density and interactions.

The density of radio AGN environments for high and low-luminosity sources are compared to those of normal galaxies in Malavasi et al. (2015). The low-luminosity sources are observed to favour over-dense environments. This finding is consistent with the idea that low-luminosity AGN, where accretion is slower and less efficient, are driven by hot, diffuse gas. The high-power sources are found to occupy under-dense regions where it is likely that cold gas fuels AGN activity.

Hence, there is much evidence to suggest that the physical state of infalling gas affects the accretion rate and hence radiative efficiency of an AGN. It is also possible that for galaxy interactions influence gas kinematics and temperature in a complex way. In general, an argument for one environmental factor bearing a sole influence on AGN activity is unrealistic. It is very likely that secular processes are a primary determinant with galaxy density and tidal interactions playing a secondary role.

1.6 AGN Environment and Accretion-Mode

The goal of this work is to determine the link between accretion-mode (the HERG-LERG dichotomy) and environment. To do this, we consider previous studies that examine the relation between accretion-mode and environment at low-redshift. Later on, we compare them to our own results to establish a clear picture of this relation within predefined redshift intervals.

In radio-loud AGN ($0.02 < z < 0.1$), group or cluster membership has been shown to carry a stronger influence on nuclear activity than local galaxy density (Best, 2004). This occurs in all environments except for those with the lowest densities where AGN activity is minimal. AGN occupying low density environments have high radio luminosities comparable to those of HERGs (Best and Heckman, 2012). Based on this evidence, we expect that, at low-redshifts, HERGs occupy regions with low galaxy densities.

Since, the environment contains gas that fuels AGN through accretion. It is probable that each member of the accretion-mode dichotomy are fuelled differently. Due to the fact that accretion efficiency is higher in HERGs than LERGs, HERGs may be fuelled by cold gas of local origin and LERGs by hot gas from the intracluster medium. Hot gas fuelling is still only speculated in theory. Some reasonable observational evidence is still required to fully verify it (Hardcastle et al., 2007).

On an SDSS radio-loud (RL) sample classified into accretion-modes, evidence depicting a relation between cold gas and AGN activity has been found. This is shown in Janssen et al. (2012) where the sample is divided into red, green and blue classifications by way of 4000Å break strengths (D_{4000}). Results indicate that for HERGs and LERGs, the hosting probability for blue galaxies (fraction of galaxies that are blue) has a stronger dependence on SFR (seen in Fig. 1.10). The interpretation states that cold gas in a LERG enhances the probability of an AGN becoming a luminous RL AGN. Depending on the availability of cold gas, a LERG may evolve into a HERG through continuing accretion.

Galaxy interactions have also been found to contribute to AGN activity in low M_* X-ray selected AGN at redshifts, $0.1 < z < 1.2$. Such sources are found in regions that have

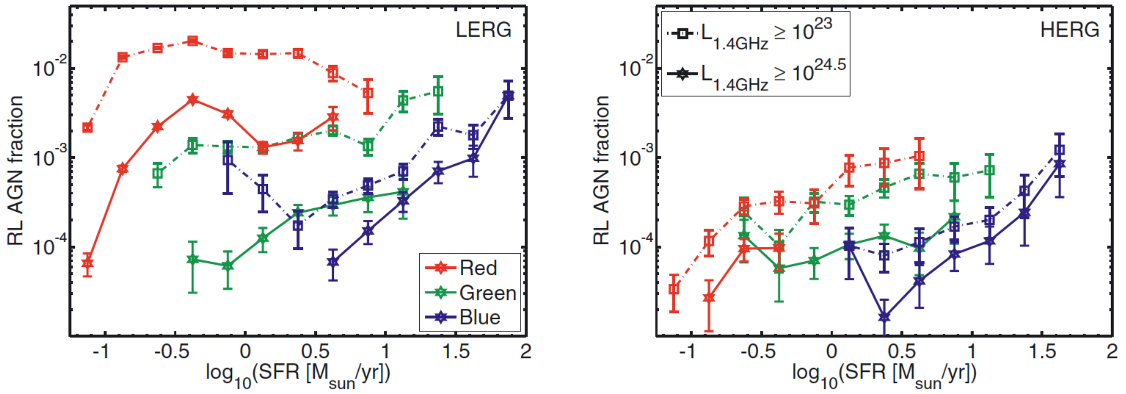

FIGURE 1.10: Radio-loud AGN fraction is a function of SFR in $M_\odot$/yr. SFR of radio-loud LERGs and HERGs are classified as red, green and blue based on 4000Å break strengths (Fig. 6 of Janssen et al., 2012).

large-scale underdensities and small-scale overdensities such that interactions are likely to occur. These sources are also observed to have mid-IR excesses consistent with efficient radiative accretion that is dust-obscured. The high M_* found in clusters and groups are massive ellipticals fuelled by hot gas (Tasse et al., 2008). We find that these sources are similar to LERGs. It is possible that they actually are.

An alternative explanation for AGN fuelling is given in Ellison et al. (2015), where gas is understood to have two possible origins: large-scale environment and stellar winds from evolved stars. This is made clear by the radio-loud LERG fraction ($0.01 \leq z \leq 0.2$) in SDSS galaxy pairs for which no correlation between AGN fraction and pair proximity is measured implying that environment on a larger scale or stellar winds from an unstable stars, perhaps drive nuclear activity more than local galaxy density.

Much of the evidence presented so far on the relation between environment and accretion-mode, or classifications similar to it, have been based on low-redshift samples. The radio data in this work extends to higher redshifts i.e $z \sim 1.2$ and is also 100 deg^2 wide. Hence, it strikes a good balance between low-redshift, shallow, wide area surveys and high redshift, deep, narrow-beam surveys by being both relatively deep and wide. This allows us to inspect this relation on new kind of dataset, giving us fresh insight into the role of galaxy density on nuclear activity measured in the radio continuum.

1.7 Thermal Dust Re-emission in WISE

Thermal dust re-emission can be traced in mid-IR wavelengths (spanning $3.4 - 22$ μm). This is a wavelength range covered exclusively by the Wide-Field Infared Survey Explorer (WISE) bands W1 (3.4 μm), W2 (4.6 μm), W3 (12 μm) and W4 (22 μm). Dust exists in the interstellar medium (ISM) of galaxies and is traced in the mid-IR through its re-radiation of absorbed UV-optical photons. The origin of this radiation is protostellar and OB-type stellar populations. Given this link, dust can also be taken as a tracer of star-formation (Asabere et al., 2014).

Photons are absorbed and re-emitted by dust in the torus of an AGN. The effect is optical and UV radiation that is dimmed and reddened resulting in sub-mm and mid-IR continuum emission. Dust temperatures range from $20 - 200$ K and dust grain have sizes ranging from $1 - 100$ nm. Grain sizes are therefore of the same order of magnitude as UV-optical wavelengths explaining why dust absorbs UV-optical wavelengths the most.

In Wright et al. (2010), different classes of objects are shown to occupy specific regions of the WISE two-colour diagram. In this, the colour index [W1 - W2] (W12) is depicted as a function of [W2 - W3] (W23) for Vega-system (standard for WISE) magnitudes (shown Fig. 1.11). This diagram provides a useful and approximate diagnostic for predicting classes and types of objects based on WISE data.

Another WISE diagnostic for classifying radio sources into HERGs and LERGs is provided by Gürkan et al. (2014). The diagnostic shows how WISE data can distinguish HERGs from LERGs in populations of radio-loud AGN (as seen in WISE two-colour diagrams for several radio source samples in Fig. 1.12). A rather discernible divide between LERGs and HERGs is visible on both plots. The mid-IR AGN wedge from Mateos et al. (2012) identifies luminous AGN that have a high likelihood of being dust-obscured and is shown in Fig. 1.12. Hence, in the diagram, the presence of a small group of LERGs (and NLRG) inside the wedge supports the idea that these sources are less likely to have dusty torus structures (Heckman and Best, 2014).

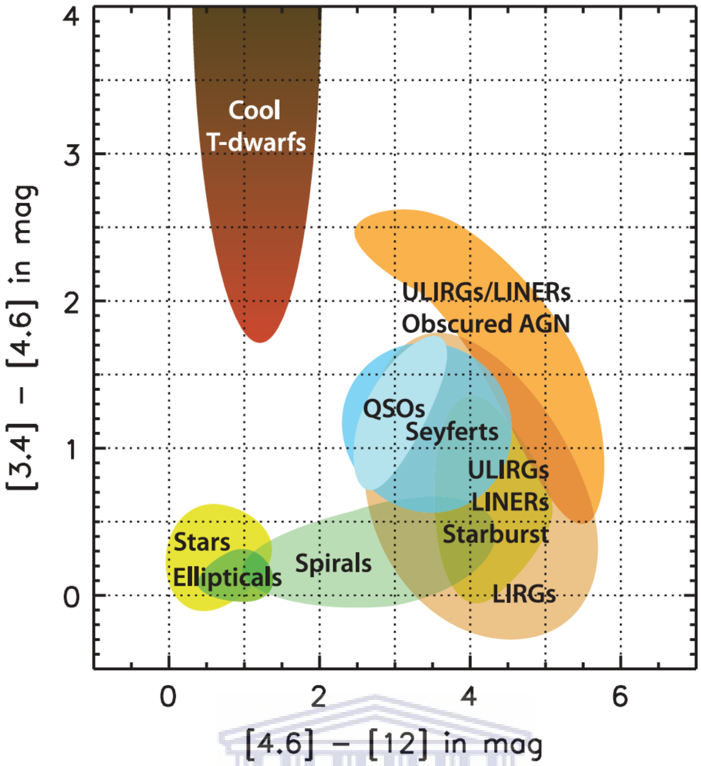

FIGURE 1.11: W12 is a function of W23. Location of source on the WISE two-colour diagram indicates AGN classification and/or morphology (Fig. 12 of Wright et al., 2010).

WISE colour indices and luminosities are perhaps mores useful at classifying sources where dust re-emission occurs. WISE diagnostics used on sources without dust structures may simply fail to work due to weak mid-IR detections brought about by insufficient dust. .

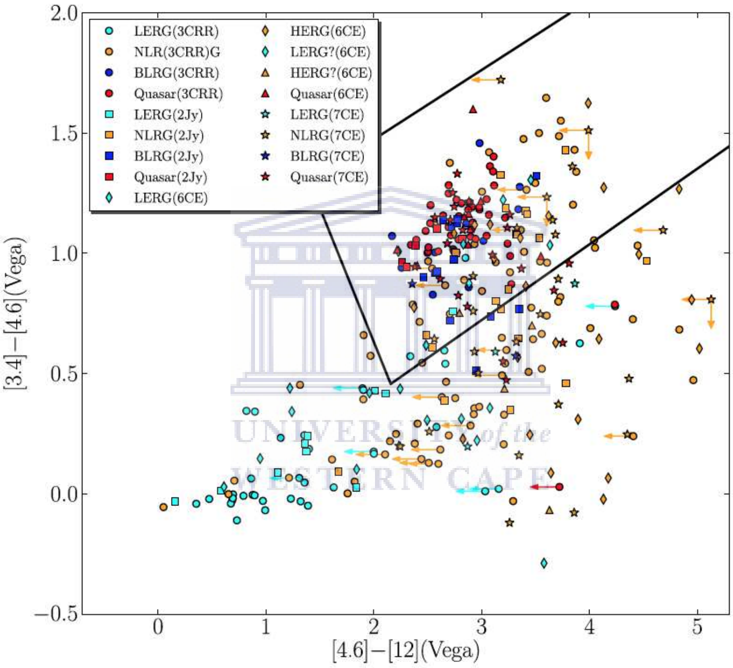

FIGURE 1.12: W12 as a function of W23. The three-band AGN Wedge (Mateos et al., 2012) selects mid-IR AGN (Fig. 3 of Gürkan et al., 2014).

1.8 Summary

We have outlined the main goal of this work. This is to investigate the influence of environment density on accretion-mode classification. A brief summary of discoveries that have led to the current AGN picture has been given. We have described the composition and speculated powering mechanisms behind AGN and shown the general AGN structure based on the Unified AGN Model. We broke down accretion-mode dichotomy and discussed the main features of each type of radio galaxy under its umbrella i.e. HERG and LERG. We selected literature relevant to this study and discussed the possible implications of their results. We then closed the chapter with a caveat on WISE classification diagnostics in sources where thermal dust re-emission of stellar light occurs.

Chapter 2

Methodology

In this chapter, we summarise the technical design features of observing tools used to obtain our datasets. In addition to this, we describe the cross-matching of JVLA (Jansky Very Large Array) radio data (Heywood et al., 2016) with SDSS optical, WISE mid-IR and UKIDSS near-IR surveys as a means of creating a multiwavelength dataset. This is done with the purpose of probing different attributes of our radio sources. The SDSS optical data provides photometric redshifts (photo-z's). In WISE mid-IR, we detect the thermal dust re-emission. The UKIDSS near-IR survey gives us petrosian K_s magnitudes we use as a proxy for M_*. We also describe the method for calculating the environment densities of the JVLA-selected radio sourced. We discuss why we refer to our JVLA-SDSS catalogue as radio-loud AGN. We also explain how the AGN and control samples are constructed.

2.1 Overview

In order to examine the link between radiative accretion efficiency and local galaxy density, we use a sample of radio sources detected by the JVLA in the $1 - 2$ GHz range. Then invoking an algorithm that identifies neighbouring galaxies within projected apertures centred on each JVLA radio source cross-matched with SDSS. For each of these sources, we determine the $\mathrm{N^{th}}$ nearest neighbour distances ($\mathrm{d_N}$). Applying a specific redshift constraint on on the line-of-sight separation between AGN and their neighbours, we obtain the surface-density (Σ_N). The gives us a 2D projected density for all JVLA radio sources.

We assume that the majority of these are AGN based on evidence given by local ($0.003 < \mathrm{z} < 0.3$) NVSS (radio) luminosity functions from Mauch and Sadler (2007b). These have indicated that a greater proportion of AGN occur when $\mathrm{L_{1.4GHz}} \gtrsim 10^{23}$ W/Hz. Below this threshold, the majority of the radio sources are star-forming.

We compile a sample of control galaxies matched individually to each radio AGN in terms of stellar-mass ($\mathrm{M_*}$) and redshift (z). Redshifts are obtained from SDSS data (York et al., 2000) and United Kingdom Infrared-Telescope Deep Sky Survey (UKIDSS) data (Lawrence et al., 2007). In addition to being $\mathrm{M_*}$ and z-matched, these SDSS control sources are also selected at angular distances $> 60''.0$ from each radio AGN. This is done to ensure that field sources exist well outside local environments of the radio AGN.

When calculated from the AGN sample, surface-density represents local galaxy density for the AGN. Surface-density measured on control galaxies associated with specific AGN and averaged over, provide the control (or field) density. Comparing radio AGN and field densities yields the relative density which indicates density of the AGN's environment relative to the field. Accretion-mode can be traced using radio-luminosity with HERGs having characteristically higher radio-luminosities than LERGs (Best and Heckman, 2012). Using JVLA radio flux density (in mJy) and distance obtained from SDSS photometric redshifts, we obtain 1.4 GHz radio-luminosities. With this, we are able investigate the trend between accretion-mode and density by examining how relative density changes as a function of 1.4 GHz radio-luminosity.

2.2 The Data

This section describes the process of cross-matching catalogues. Cross-matching involves taking a list containing the positional sky co-ordinates (ra, dec) of a group of sources (catalogue 1) and matching them to sources in a similar type of list (catalogue 2). A match is achieved by finding a source in catalogue 2 that is closest (separated by least angular distance) to a source in catalogue 1. This matching process is done for every source in catalogue 1. The results in a cross-matched catalogue that is described as symmetric or one-to-one.

In this work, we compile multiwavelength datasets by first cross-matching the JVLA radio data with the *SDSS Co-add: Galaxy Photometric Redshift Catalog* (Reis et al., 2012). From this, we obtain redshifts and sky co-ordinates (ra, dec) for neighbouring galaxies to the JVLA-detected sources. The co-ordinates are used to calculate projected angular distances (in arcseconds) which are then converted to projected distances (in kpc). This yields distances to N^{th} nearest neighbours which gives us the surface-density parameters. With this, we obtain galaxy density measures.

We cross-match JVLA-SDSS with *UKIRT Infrared Deep Sky Survey DR10 Plus* (UKIDSS) which contains petrosian K_s-band magnitudes. With these, we can approximate M_* (Gavazzi, 1993). From a cross-matched catalogue containing combining SDSS DR7 galaxy and UKIDSS data, we select a set of control galaxies. These are matched to the radio sources in terms of M_* and redshift to the AGN they are associated with.

We obtain mid-IR data by cross-matching the combined JVLA-SDSS catalogue with the *AllWISE Source Catalog*. The WISE data may be useful for determining accretion-mode (Gürkan et al., 2014) and classification or morphological type (Wright et al., 2010) for sources with nuclei encircled by a dust medium.

2.2.1 JVLA Radio Data

The JVLA is a radio interferometer array that comprises 27 antennae with 25 m diameter each. One of its main uses has been performing radio continuum surveys. The first of these to be completed was Faint Images of the Twenty Centimetre Sky (FIRST) survey (Becker et al., 1994) and the NRAO VLA Sky Survey (NVSS) (Condon et al., 1998).

More recently, the VLA was upgraded to enhance its surveying capabilities and was renamed, the Janksy VLA (JVLA). One part of these new amendments was an improvement in performance by 1 to 4 orders of magnitude, translating to an increase of 1σ point-source continuum sensitivity, in 12 hr observing durations, from 10 to 1 μJy. Bandwidths as broad as 8 GHz were added to the increase in sensitivity. The upgraded array covers 8 frequency bands spanning, $1-50$ GHz for Cassegrain focus receivers. There is also an additional $50-450$ MHz band associated with the ninth prime-focus receiver (Perley, 2013).

This work makes use of data from a recent snapshot survey captured by the JVLA in a hybrid CnB configuration[1]. The survey scanned a section of the SDSS Stripe 82 field with beam frequencies in the $1-2$ GHz range. The surveyed field is 100 deg^2 in area providing a radio source catalogue that forms the basis of our dataset.

To complete the survey, the JVLA correlator delivered $1-2$ GHz of bandwidth over 16 spectral windows each with 64 x 1 MHz channels in standard, wide L-band mode. Observation times for the 16 scheduling blocks were 4.5 hours each in duration. A total of 1368 pointings were made for integration intervals with durations of 2.5 minutes each. This total consists of 608 and 760 pointings completed in the east and west portions of SDSS Stripe 82. Surveyed region and pointings are shown in Fig. 2.1.

The resulting survey of Stripe 82 consists of separate east and west portions. The discontinuity in the eastern part is a consequence of the array transitioning out of the CnB configuration after scanning only 12 of the 16 scheduling blocks planned. As a result of this, the total number of actual pointings made were 522 in the east and 504 in the west. For each scheduling block, the radio source, 3C 48, was used to calibrate flux. A strong calibrator (source ID J2225-0457 in this catalogue) was chosen for bandpass correction. After each hour of observing, a new and more suitable calibrator was selected to correct phase (Heywood et al., 2016).

---

[1] This is an arrangement for the receivers that has JVLA's east and west arms positioned in the C-configuration. While the north arm is placed in the extended B-configuration.

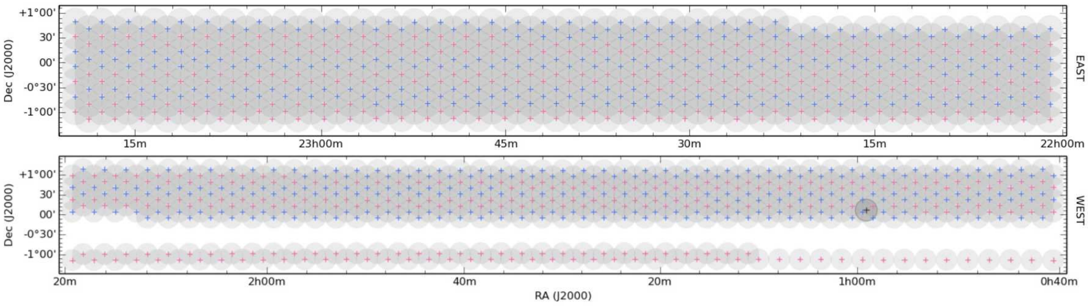

FIGURE 2.1: The upper and lower panels are the east and west portions of Stripe 82, respectively. Blue and pink crosses represent the centroids of each separate pointing. Grey circles represent individual pointing coverage (Heywood et al., 2016).

The main survey products are a set of radio mosaic images and a radio source catalogue. Mosaics of the east and west contain a third of a billion pixels. Hence, only the brightest radio sources are visible in the final images. The source finder algorithm, PyBDSM (Mohan and Rafferty, 2015) is used to compile the radio catalogue. In this catalogue, each radio source is labelled according to island, Gaussian and source identifiers (IDs). In total, 8948 unique radio sources are obtained (details given in Table. 2.1) (Heywood et al., 2016).

The island ID is assigned when the signal of a source exceeds 5σ, where σ if the effective local rms noise which is 88 μJy/beam in this survey. In these cases, an island is drawn out as a 3σ contour around the source. An island ID is then assigned. Gaussian fits to each of these islands forms list of components with individual Gaussian IDs. In the case that no such fit is possible, the source is considered point-like. The algorithm also makes an attempt at identifying discrete sources, each assigned a source ID (Heywood et al., 2016).

A total of 8946 sources in the catalogue have a unique source ID. This means that there are approximately 8946 discrete sources in the catalogue. There is a possibility that some of these are not discrete radio sources. Below the 5σ threshold, there may be a strong likelihood of obtaining spurious noise detections (Hogg, 2001; Condon, 1974). These lead to artefacts showing up in the immediate vicinity of strong radio sources. These noise detections may be mistaken for astronomical objects when they are not manually excised from the catalogue through a one-by-one inspection process (Heywood et al., 2016).

Region	Gaussian	Island	Source
East	5674	4602	4354
West	6094	4869	4594
Total	11768	9471	8948

Table 2.1: Number of sources detected by the JVLA in east and west portions of the survey (Heywood et al., 2016) for each identifier (ID) type.

Comparing radio images of this JVLA survey to those of similar surveys, we see a marked improvement in the resolution of diffuse structures in the radio sources. These new images have 16 x 10″ resolutions, beneficial for identifying extended radio sources i.e. low surface-brightness radio sources and extended diffuse emission (Heywood et al., 2016). Hence, this survey strikes a better balance between sensitivity and angular resolution than FIRST (Becker et al., 1994) and NVSS (Condon et al., 1998).

2.2.2 SDSS Optical Data

The designated telescope for the Sloan Digital Sky Survey (SDSS) creates optical images in its five characteristic bands, u,g,r,i,z. These are highlighted in Table 2.2 (York et al., 2000). SDSS uses a 2.5 m alt-azimuth telescope at the Apache Point Observatory. It operates on drift-scan mode using an f/5 modified Ritchey-Chrétien design with wide-field imaging capability. A mosaic CCD camera at the telescope's Cassegrain focus is used for image creation. A spectrograph replaces the CCD to obtain spectra.

The CCD has been designed with six columns (also called *camcols*) and five rows for each SDSS filter. The drift-scan runs perpendicular to this column arrangement, meaning that each run consists of six scanlines (one for every CCD column). The drift occurs along great circles and forms a *strip* of scanlines in the direction that the *camcols* are arranged. When a second strip is added to an observation, the result is a wide-field image referred to as a *stripe* (York et al., 2000). The surveyed field we extract data from is one such stripe and thus called *Stripe 82*.

Stripe 82 covers a portion of the Celestial Equator on the Southern Galactic Cap, shown as red portions in Fig. 2.3. We make extensive use of the *SDSS Co-add: Galaxy Photometric Redshift Catalog*. This is a co-added data product of SDSS Data Release 7 (DR7). Our

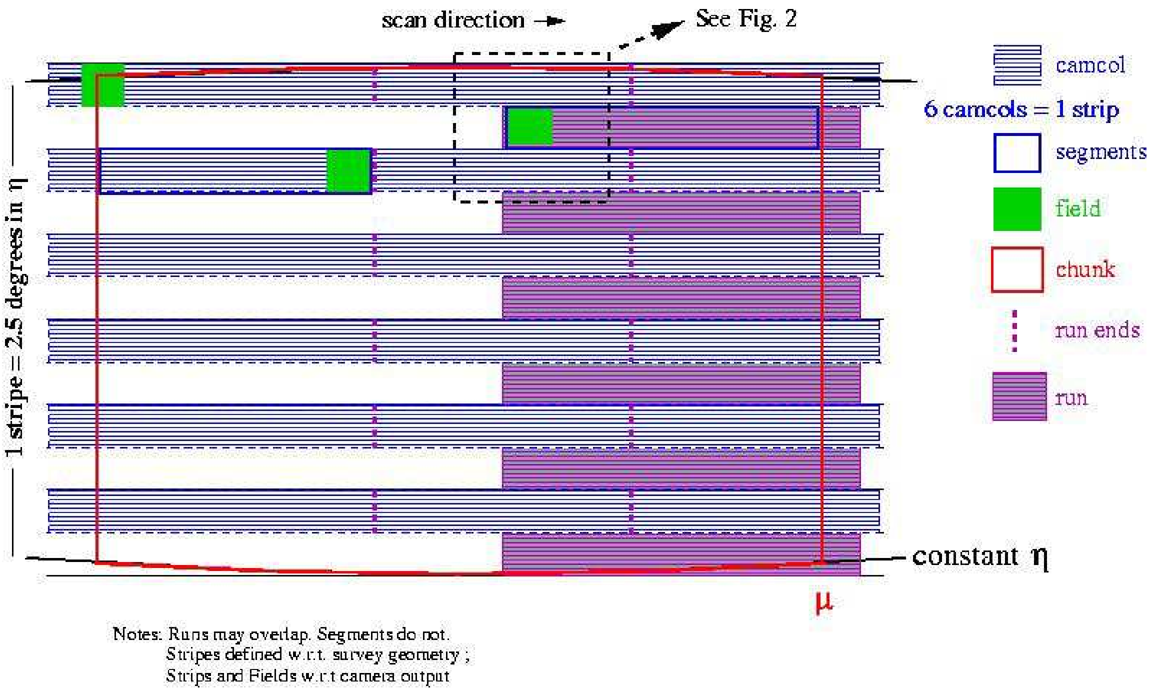

FIGURE 2.2: Scanning procedure of SDSS telescope. A 'stripe' is a combination of runs comprising 12 *camcols* (SDSS, 2007a).

choice to use this catalogue is motivated by its depth in redshift, number of detected sources and sky coverage which all exceed those of legacy SDSS spectroscopic redshift catalogues. One of these being PRIMUS which contains $\sim 120,000$ sources detected over an area 9.1 deg^2. SDSS DR7 detected 13,688,828 sources over a 7500 deg^2 large area. This outweighs PRIMUS in both area and percentage of sources detected.

SDSS Stripe 82 covers 275 deg^2, over declinations, $-50° < \alpha < 59°$ and right-ascensions, $-1.25° < \delta < 1.25°$. The catalogue includes all five SDSS bands and contains galaxies detected up to magnitude limit of r = 24.5 (Reis et al., 2012). The limiting magnitudes summarized in Table 2.2 are for 50% completeness of the SDSS DR7 galaxy survey. These limits represent the medians and rms values of co-add magnitudes for sources in 50 randomly selected fields in SDSS DR7.

Photometric redshifts are determined with greater accuracy for sources with $r < 22$ i.e. bright galaxies. It follows that the uncertainty of photo-z's increases above this limit i.e. $r \geq 22$. In fact, algorithms that determine photo-z are found to be less efficient at the faint source end (Reis et al., 2012).

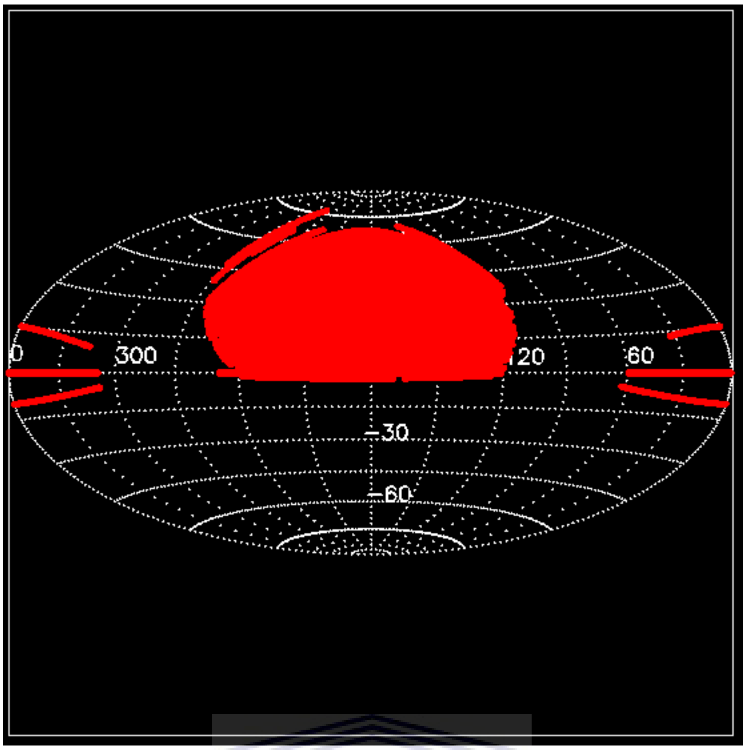

FIGURE 2.3: The red represents sky areas surveyed by SDSS DR7 (SDSS, 2007b).

Band	λ (Å)	μ_{G}	$\sigma(\mu_{\mathrm{G}})$
u	3551	23.25	0.23
g	4686	23.51	0.18
r	6166	23.26	0.14
i	7480	22.69	0.17
z	8932	21.27	0.23

TABLE 2.2: Central wavelength, AB limiting magnitude and rms magnitude are denoted by λ, μ_{G} and $\sigma(\mu_{\mathrm{G}})$, respectively for *SDSS Co-add: Galaxy Photometric Redshift Catalog* data. The subscript G denotes galaxy (Reis et al., 2012).

Algorithms used to compute photometric redshift operate on two principles: template-fitting and training-sets. To form the co-add photo-z catalogue used in this work, the training-set approach was taken. This involved taking the relation between the spectroscopic redshifts and photometry of a set of galaxies and using it to obtain an empirical relation between the photometric properties of a source[2] and redshift. Through this method, redshift can be deduced for each SDSS galaxy.

This particular approach is embedded in the artificial neural networks (ANN) method which provided estimates of galaxy photo-z's. In addition to this, a nearest neighbour

---

[2] Such properties are the concentration indices as morphology indicators, colours and magnitudes in each bandpass.

Band	λ (μm)	FWHM ($''$)	f_{lim} (mJy)
W1	3.4	6.1	0.08
W2	4.6	6.4	0.11
W3	12	6.5	1.0
W4	22	12.0	6.0

TABLE 2.3: Central wavelengths (λ), resolving power (FWHM) and flux limits ($f_{\rm lim}$) of WISE bands.

estimator (NNE) determines error in photo-z. The algorithm calculates photo-z errors by associating them with errors on sources in a validation set that have similar magnitudes (Reis et al., 2012).

2.2.3 WISE Mid-Infrared Data

During the course of its mission, WISE (Wide Field Infrared Survey Explorer) mapped the sky in thermal infrared wavelengths. Given the fortunate circumstance that mid-IR background emission in space is relatively low, enhanced the sensitivity of its surveys. WISE was cryogenically cooled in order to better detect infrared emission in its four characteristic bands: W1, W2, W3 and W4. The flux limits for this survey are shown in Table Table 2.3 and apply to the unconfused regions located along the ecliptic (Wright et al., 2010).

WISE had a 40 cm diameter and Si:As (silicon, arsenic) CCD arrays, orbiting at 526.5 km altitude. Its cooling system kept its CCD arrays at temperatures < 7.5K which helped reduce thermal noise but also telescope sensitivity. Shortening integration times also helped cut down the thermal background in the W3 and W4 bands where this type of noise was most pronounced. By the end of its life-span, WISE had mapped 99% (as shown in Fig. 2.4) of the sky, up to a minimum depth of eight frames (Wright et al., 2010).

The *AllWISE Source Catalog* is a product of the WISE mission. It is better than its predecessor, the *All-Sky Release Catalog*, in 3.4 μm (W1) and 4.6 μm (W2) sensitivity. The *AllWISE Source Catalog* contains almost 750 million discrete sources. Because mid-IR wavelengths are effective at selecting dust-obscured objects well, WISE photometry can be used to provide data for discerning between sub-groups and/or classes of AGN. This is especially useful for objects with reduced emission in the UV-optical continuum due to dust absorption (Mason, 2014).

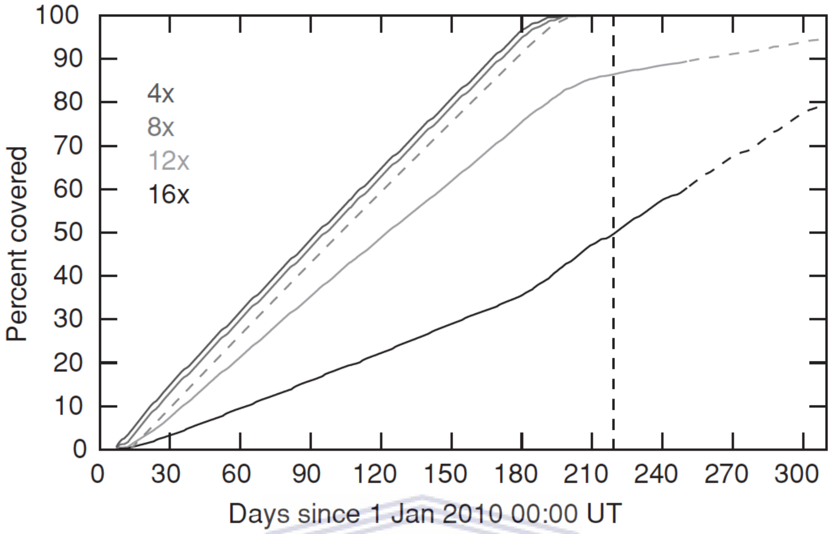

FIGURE 2.4: Percentage of the whole sky surveyed with time (in days) relative to the starting date and time. Each grey line represents a coverage depth of either 4, 8, 12, or 16 frames (Fig. 5 of (Wright et al., 2010)).

2.2.4 UKIDSS Near-Infrared Data

UKIDSS DR10 Plus is a near-IR survey (Lawrence et al., 2007). It has been widely considered, the infrared counterpart to SDSS. Despite it's coverage being limited to very specific regions (shown in Fig. 2.5), the survey detects objects much fainter than those in the *Two Micron All-Sky Survey* (2MASS), making it a better near-IR option for faint sources. UKIRT also covers a substantial portion of the equatorial region that overlaps well with SDSS Stripe 82.

The survey uses the Wide Field Camera (WFCAM) on the United Kingdom Infrared Telescope (UKIRT). The camera consists of a 0.21 deg^2 field of view and has a 4m aperture. The instrument has 5 filters: Z,Y,J,H, and K$_s$ that span a wavelength range of $0.83 - 2.37$ μm. Their details are summarised in table 2.4. Our region of interest is SDSS Stripe 82. Hence, we select the Large Area Survey (LAS) as a data source (shown in Fig.

Band	λ	Range	Width
Z	0.8817	0.836-0.929	0.093
Y	1.0305	0.979-1.081	0.102
J	1.2483	1.169-1.328	0.159
H	1.6313	1.492-1.784	0.292
K_s	2.2010	2.029-2.380	0.351

TABLE 2.4: Central wavelengths, wavelength range and bandpass width in μm for UKIDSS bands.

2.5). LAS provides Y,J,H and K_s bands with objects detected up to a magnitude limit of K_s = 18.2. In total, the LAS region spans an area of 4028 $\deg^2$.

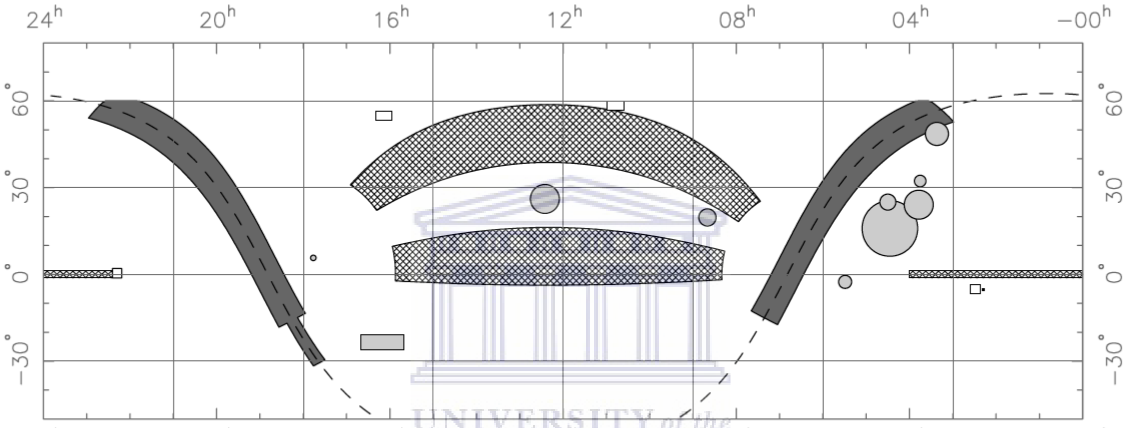

FIGURE 2.5: Stripe 82 coincides with the cross-hatched portion of this UKIDSS coverage map (Fig. 6 of Lawrence et al., 2007).

2.3 Multiwavelength Cross-match

Here, we describe the parameters and steps involved in forming the multiwavelength dataset. We describe how cross-match JVLA radio data with the SDSS optical, WISE mid-IR and UKIDSS far-IR catalogues in sections 2.2.1, 2.2.2 and 2.2.3, respectively. We first obtain a combined JVLA-SDSS catalogue which we then match with both WISE and UKIDSS. In each step, only a fraction of the initial 8946 radio sources are recovered. We, therefore, summarise all cross-match statistics in Table 2.5, quoting the number of counterparts detected as a percentage of the total number of sources in the JVLA catalogue.

Survey	Wavelength/Frequency	Cross-match Count (%)
JVLA	1 - 2 GHz	8946 (100)
SDSS DR7	3551 - 8932 Å	4130 (46.2)
WISE	3.4 - 22 μm	3414 (38.2)
UKIDSS	1.235 - 2.159 μm	2716 (30.4)

TABLE 2.5: The wavelength or frequency range covered by each survey are shown. JVLA constitutes the primary source catalogue. It is cross-matched with SDSS, WISE and UKIDSS catalogues. The number of sources obtained after cross-matching JVLA and each one of these catalogues is given as the cross-match count. The percentage of initial JVLA sources recovered in the cross-match is also shown (in brackets).

2.3.1 JVLA and SDSS Cross-match

In the JVLA-SDSS catalogue, we have the redshifts necessary for calculating cosmological distance. Redshifts allow us to convert projected separations on the sky into realistic distance separations measured in standard cosmological distance units e.g. kpc, Mpc via the procedure outlines in Appendix A.1.

When cross-matching JVLA-SDSS with WISE and UKIDSS catalogues, we have the choice of selecting either radio or optical sky co-ordinates from JVLA-SDSS in the cross-match. We find that optical sources have a greater degree of precision in defining the positions of the radio sources. We, therefore, cross-match SDSS co-ordinates with WISE and then UKIDSS.

Before performing a cross-match between two catalogues, an ideal cross-matching radius, ε, (or cross-match radius) is defined. This paremeter represents the largest possible angular separation allowed between two matched sources. For separations below this limit, the most ideal multiwavelength counterpart to a source has been identified. Above the limit, cross-match identifications are more likely to be random.

To find epsilon, we cross-match the catalogues up to a sufficiently large search radius we call, $\varepsilon_{\mathrm{max}}$. The size of this is set to $20''.0$. We find that this will give us a distribution of cross-match separations that is large enough to help us determine the ideal cross-match radius. So, for each source in catalogue 1, we find every source from catalogue 2 located at angular separations $< \varepsilon_{\mathrm{max}}$. This is referred to as an 'all matches' type of cross-match.

A mock catalogue of sources is created by picking a number of random positions within the surveyed field of catalogue 1. This new catalogue contains the same number of sources as catalogue 1 and is cross-matched with catalogue 2 using the same 'all matches' method as before.

When two sources are cross-matched, their angular separation is added to the combined catalogue. A distribution of these angular separations is drawn out. For the cross-match between real catalogue 1 and catalogue 2, we obtain what we call the 'real' distribution of angular separations. Between mock catalogue 1 and catalogue 2, we obtain the 'mock' distribution.

Generally, the real distribution will peak at some angular separation and then drop off. This will be followed by a monotonic increase. The mock distribution will simply increase monotonically with angular distance. The real distribution peaks when the majority of actual counterparts to sources in catalogue 1 are identified in catalogue 2. Fewer and fewer of these true matches are made for increasing separations, hence the drop-off.

The real distribution increases again as the separation increases. This is because the cross-match algorithm begins to select sources nearby rather than true matches to sources in catalogue 1. As the search-radius increases, the search area also widens leading to more sources from catalogue 2 being identified as matches. This also explains the monotonic increase in both distributions. Where the real and random distributions intersect is the approximate point at which true counterparts to sources in catalogue 1 are no longer identified in catalogue 2. The angular separation at this point is, therefore, the ideal maximum separation for one-to-one matches between catalogues 1 and 2. Our interest is in obtaining multiwavelength counterparts rather than selecting nearby sources.

This process is carried out to combine the JVLA and SDSS catalogues. Their real and mock distributions are drawn out in Fig. 2.6. We find that the JVLA-SDSS and mock-SDSS catalogues are vertically offset. This probably implies that there are sources in JVLA with additional radio detections around them, in such close proximity that they cannot be neighbouring galaxies. They could, instead, be radio noise detections that have been spuriously identified as unique radio sources in the JVLA catalogue. The result of such an occurrence is that an increased number of sources are identified per search radius. This leads to an offset between both distributions because the randomly-selected source positions, in the mock catalogue, are more uniformly distributed in the JVLA-SDSS survey region.

Based on Fig. 2.6, the best cross-matching radius for between JVLA and SDSS i.e. $\varepsilon_{\rm opt}$ in which the subscript *opt* stands for *optical*. Through inspection, this parameter is found to be $2''.87$. We use the best-match method to find SDSS counterparts to JVLA sources. The result is a catalogue containing 4130 sources. These make up 46.2% of the initial JVLA source detections.

The combined catalogue contains SDSS photometric redshifts (photo-z's) for the sources recovered after the cross-match. We show a distribution of these in Fig. 2.7. At $z > 1.2$, the distribution drops down considerably. This in addition to the fact that the efficiency of photometric redshift estimation declines for $z \geq 0.75$ (Reis et al., 2012) encourages us to apply a redshift cut at ~ 1.2. More motivation to do this is given in Fig. 2.8 where a very sparse quantity of sources are found at $z = 1.5$ and $z = 2.0$. We suggest that sources being assigned these photo-z's is a result of the method not working well for perhaps faint sources with $z > 0.75$.

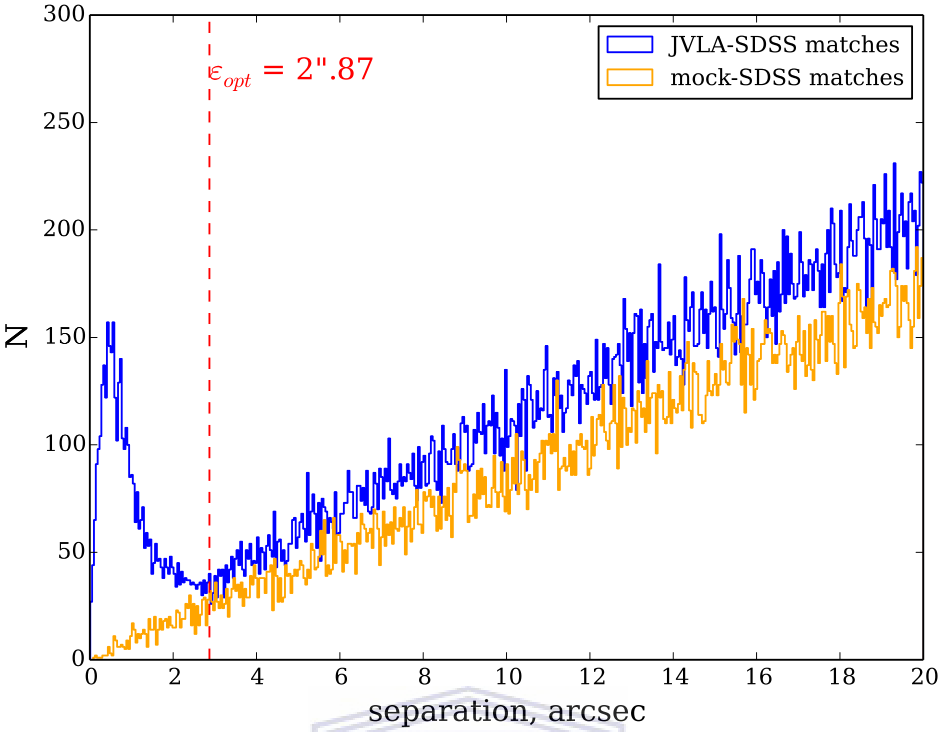

FIGURE 2.6: Distribution of angular separations between JVLA sources and nearest SDSS galaxies (blue). A similar distribution for mock-JVLA sources and SDSS galaxies is also shown (orange).

2.3.2 WISE Cross-match

In a method similar to the one applied between JVLA and SDSS (from Section 2.3.1), we cross-match the JVLA-SDSS catalogue with the *AllWISE Source Catalog* (Wright et al., 2010). To do this, we use a cross-match radius i.e. $\varepsilon_{\rm mir} = 3''.52$ where the subscript *mir* refers to *mid-IR* (inferred from Fig. 2.9).

For many of the JVLA-SDSS sources, WISE data is unavailable. This may be due to survey sensitivity or flux limit. Of the 4130 sources in JVLA-SDSS, we obtain 3414 WISE detections. This represents 38.2% of the JVLA radio catalogue.

2.3.3 UKIDSS Cross-match

We implement a cross-match between the JVLA-SDSS catalogue and *UKIDSS DR10 Plus* (Lawrence et al., 2007). Comparing real and mock distributions as Section 2.3.1

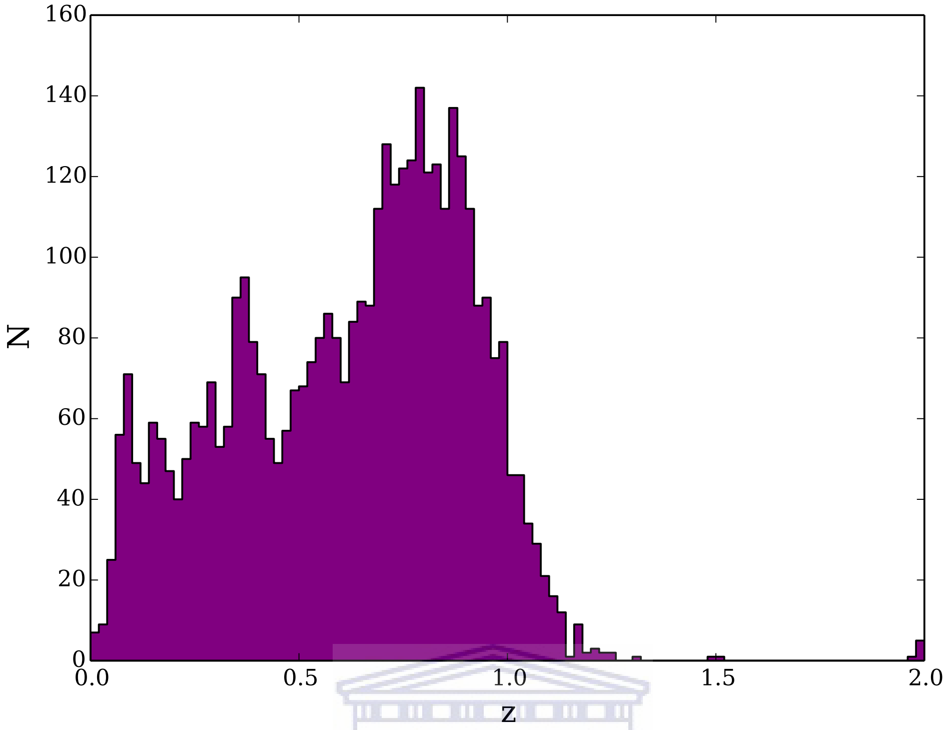

FIGURE 2.7: Photometric redshift (z) distribution of unique JVLA-SDSS radio sources.

prescribes, we determine an ideal cross-match radius of $\varepsilon_{\mathrm{nir}} = 1''.16$. where the subscript *nir* stands for near-IR. The JVLA-SDSS catalogue is matched with UKIDSS, yielding 2716 detections. This translates to 30.4% of all initial JVLA radio detections.

Fig. 2.11 depicts the Ks-magnitudes for sources in this catalogue with photo-z. This confirms that the JVLA-SDSS-UKIDSS catalogue contains a sizeable distribution of sources within the $0.1 < z < 1.2$ redshift interval we examine in this work.

Petrosian $\mathrm{K_s}$ magnitudes of matched UKIDSS sources are used as a proxy for M_*. To obtain these, we cross-match the entire SDSS galaxy photometric redshift catalogue with UKIDSS. From this catalogue, we select M_*-matched control galaxies. We use $\varepsilon_{\mathrm{nir}} = 1''.16$ to create a combined SDSS-UKIDSS catalogue that contains every galaxy in SDSS DR7 detected by UKIDSS.

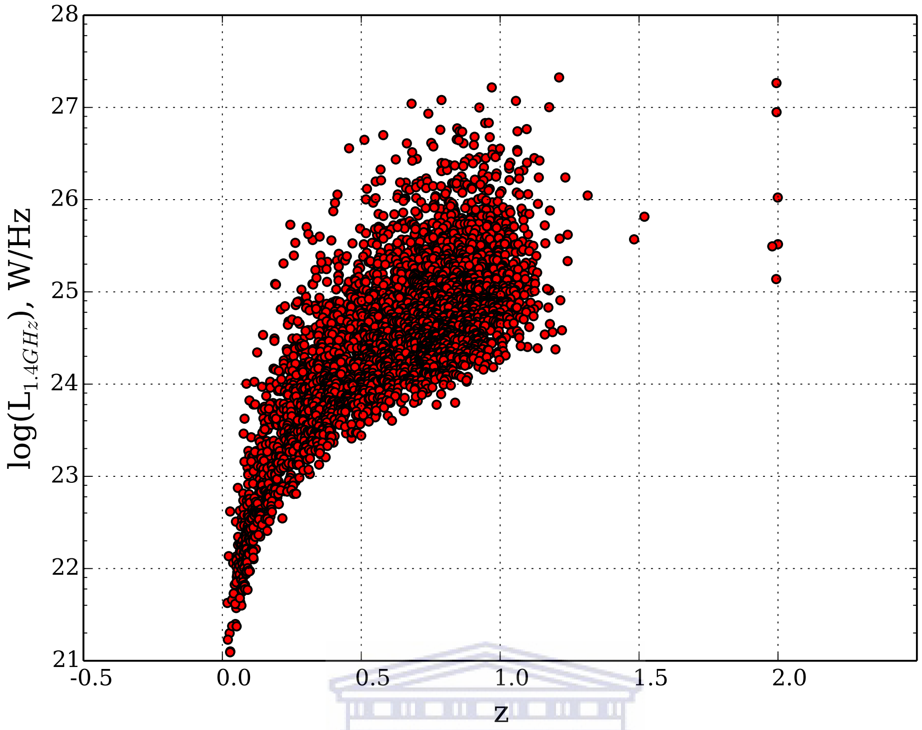

FIGURE 2.8: L$_{1.4\mathrm{GHz}}$ as function of photometric redshift (z) for JVLA-SDSS sources.

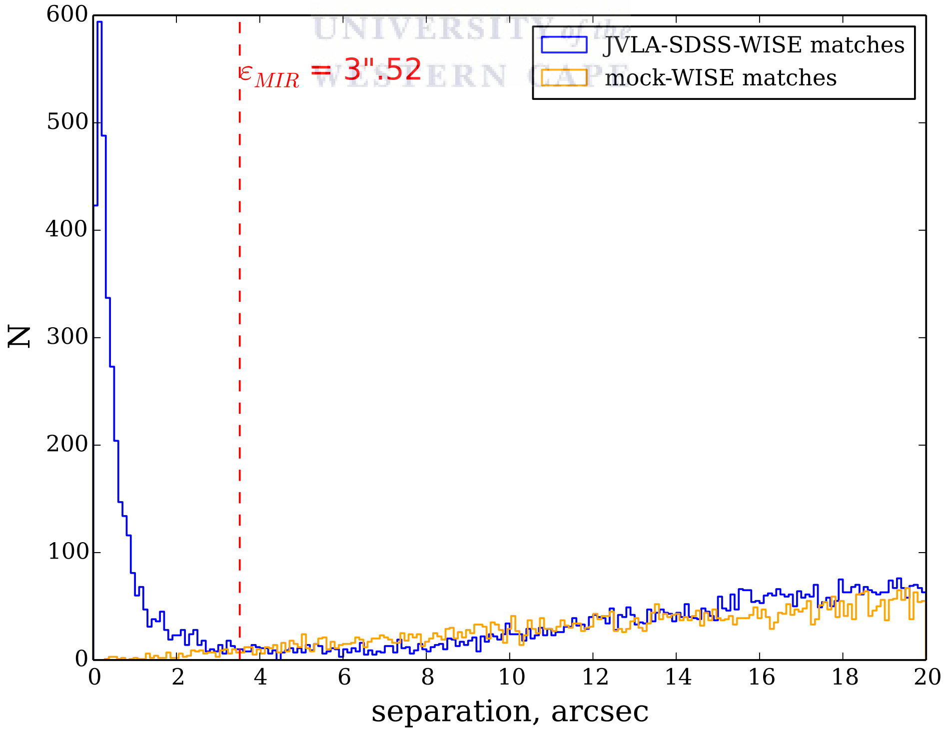

FIGURE 2.9: Distribution of angular separations between JVLA-SDSS sources and nearest WISE detections (blue). A similar distribution for mock-JVLA-SDSS sources and WISE detections is also shown (orange).

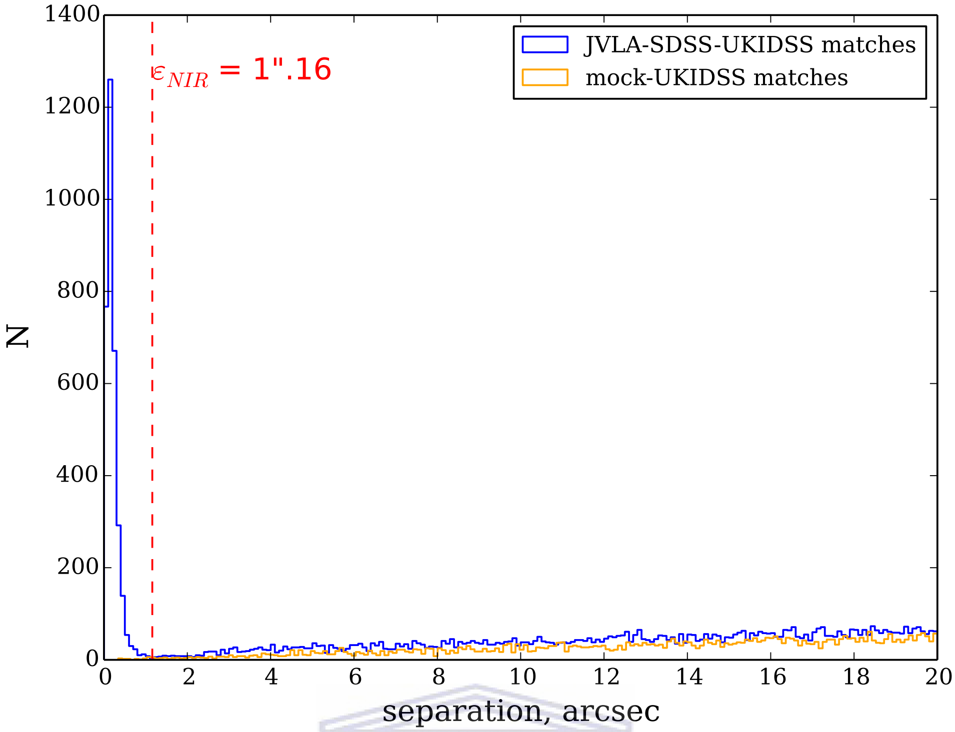

FIGURE 2.10: Distribution of angular separations between JVLA-SDSS sources and nearest UKIDSS detections (blue). A similar distribution for mock-JVLA-SDSS sources and UKIDSS detections is also shown (orange).

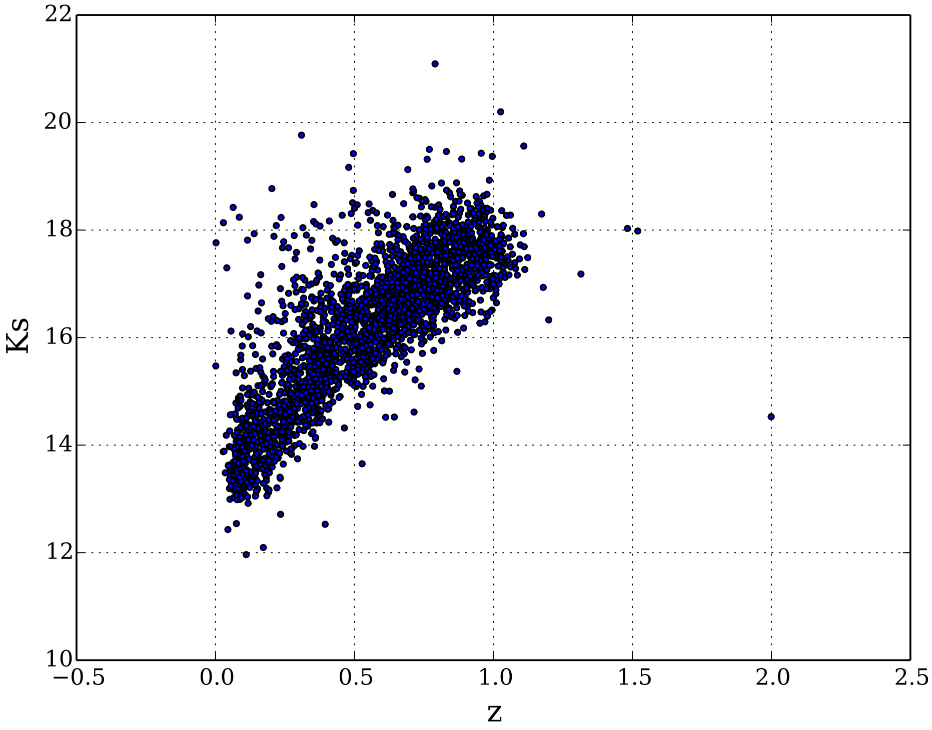

FIGURE 2.11: K_s magnitudes as a function of photometric redshift (z).

2.4 Environment Quantifier

We use the the projected surface-density parameter to measure galaxy density. This parameter is defined, once again, in equation 2.1. Surface-density parameter takes on two variables: distance to the $\mathrm{N^{th}}$ nearest neighbour ($\mathrm{d_N}$) and the closest N companion (or neighbouring) galaxies considered when measuring density around a target source (Dressler, 1980). In this work, $\mathrm{d_N}$ is measured as a distance (in kpc) on the projected plane and the surface-density, in $\mathrm{kpc^{-2}}$. We make use of this quantifier because it provides a continuous density measure over a broad range of distance scales (Cooper et al., 2005).

$$\Sigma_{\mathrm{N}} = \mathrm{N}/\pi \mathrm{d}_{\mathrm{N}}^{2} \tag{2.1}$$

A redshift constraint is applied to the surface-density parameter in each case. In the general form, this constraint is expressed as equation 2.2 where i is the target and j is the $\mathrm{N^{th}}$ nearest neighbour. An error, ε, in equation 2.2 is chosen specifically for redshift constraints on AGN and control density measures.

$$\Delta \mathrm{z} = \mathrm{z_i} - \mathrm{z_j} \leq \varepsilon(1 + \mathrm{z_i}) \tag{2.2}$$

We choose N in accordance with the mean sizes of galaxy group and clusters ($\overline{\mathrm{N_{glx}}}$). The condition for this is that $\overline{\mathrm{N_{glx}}} \leq \mathrm{N}$. This condition maintains that only galaxies in group or cluster associations are considered when calculating surface-densities. When N exceeds this average, $\mathrm{d_N}$ might be biased to higher values than expected if the $\mathrm{N^{th}}$ nearest neighbour is outside of local group or cluster region. This reasoning is built on the premise that distances between separate groups or clusters exceed the distances between individual group or cluster members (Cooper et al., 2005).

The fact that surveys are limited in size also means that catalogue sources on the outskirts of a survey are susceptible to “edge effects”. The result being that edge sources have densities biased to lower values when some of the neighbouring sources, that actually exist, are not counted because they reside outside the surveyed field. These occur when the nearest neighbour search area intersects with the edge of the surveyed field (Cooper et al., 2005).

The survey edge problem can be solved by applying edge-cuts to the JVLA-SDSS catalogue. This is done on sections where the JVLA and SDSS field edges coincide. Such an overlap occurs at three survey edges in total: the northern and southern edges of the west JVLA survey and in the southern edge of the east JVLA survey (as seen in Fig. 2.12). In the rest of the field, SDSS survey edges extends farther out than the JVLA survey, enough for optical neighbours to be obtained at all the search radii used in our analysis. Any source located at a projected separation from the edge less than the size of the search radius is flagged as a potential source of edge-effects bias.

For Stripe 82 galaxies, the most extensive catalogue of redshifts currently available consists of photometric redshifts (photo-z's). But photometric redshifts are less precise than spectroscopic redshifts leading to increased uncertainty in line-of-sight positions (Cooper et al., 2005). Despite this, we are motivated to use them because the photo-z catalogue contains a greater proportion of sources and the fact that spec-z's are limited to $\mathrm{r} < 17.7$ in comparison to $\mathrm{r} \sim 24$ for the photo-z's.

Local density measured on mock galaxy catalogues in Cooper et al. (2005) indicate that the use of photo-z's reduce precision of density measure. This effect is pronounced for photo-z's with redshift errors (σ_{z}) as low as 0.02. The loss of precision is seen in all but the lowest densities (Cooper et al., 2005). Our own use of photo-z's could easily contribute to less precise density estimation. It is also a known fact that redshifts are even less accurate for sources close to the flux limit of SDSS i.e. $\mathrm{r} \sim 22$ (Reis et al., 2012). This may affect the density measured for the faintest sources.

Many of the issues associated with photo-z may be overcome by comparing AGN density to control galaxy density. The control galaxies are matched to the AGN in terms of mass (M_*) and redshift (photo-z) and located an angular separation $> 60''.0$ from the associated AGN. This means that to obtain local galaxy density relative to the field, we compare AGN with control galaxies that have are similar in M_* and photo-z. As a result, the effects of M_* and photo-z are removed from the density-relation being tested. Hence, the lack of precision associated with using photo-z does not bias the relative density measure much.

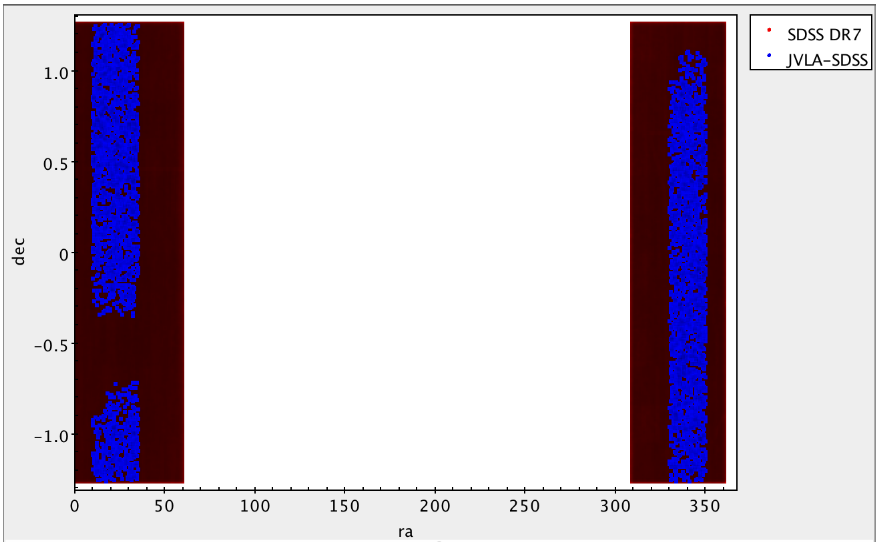

Figure 2.12: Coverage of SDSS DR7 is shown in dark red. JVLA-SDSS coverage is shown in blue.

2.5 AGN Sample

The AGN sample consists of sources in the JVLA-SDSS catalogue. We assume that the majority of the sources in this catalogue are AGN. We do this based on a finding that suggests that at $\sim 10^{23}$ W/Hz, SF galaxies become less prevalent in local ($0.003 < z < 0.3$) 1.4 GHz radio source groups (Mauch and Sadler, 2007b). Above this limit, AGN comprise the majority. This is a rather simplistic approximation, considering the fact that our sample extends to $z \sim 1.2$. Since the focus of our study is the role of environment on accretion-mode, calling our radio sources AGN does not affect our results in a major way.

To measure AGN density, we search for the N$^{\text{th}}$ nearest neighbours to each AGN. Using the separation distances to each, we compute the local galaxy density. The search radii used in the algorithm span from $20''.0 - 120''.0$ in intervals of $10''.0$[3].

The probability of an AGN having a companion galaxy increases with search radius. The larger this radius, the larger the search area and hence, the stronger the likelihood of having a neighbouring galaxy. For radii between $20''.0 - 120''.0$, all the radio AGN have at least one companion galaxy in SDSS. The number of AGN per search-cone radius (SCR) is, however, reduced by edge-effect cuts that are dependent on search radius. Table 2.6 summarises the fraction of JVLA-SDSS sources that remain after an edge-cut.

SCR ($''$)	Neighbouring Source(s) (%)	Post Edge-cut (%)
20	2716 (100)	2714 (99.9)
30	2716 (100)	2711 (99.8)
40	2716 (100)	2707 (99.7)
50	2716 (100)	2703 (99.5)
60	2716 (100)	2699 (99.4)
70	2716 (100)	2696 (99.3)
80	2716 (100)	2694 (99.2)
90	2716 (100)	2689 (99.0)
100	2716 (100)	2684 (98.8)
120	2716 (100)	2679 (98.6)

TABLE 2.6: The quantity of AGN with neighbours remains constant with increasing SCR (search-cone radius). We show the number of AGN remaining after the edge-cut is applied. This is also given as a percentage of the total number of AGN in the JVLA-SDSS-UKIDSS catalogue.

---

[3] The upper limit is capped at $120''.0$ by limits on computing power.

A redshift constraint between the AGN and their N$^{\mathrm{th}}$ neighbours (denoted by the subscript, ‘neigh’) is applied to achieve the AGN density measure. This particular constraint follows the format of equation 2.2 defined as,

$$\mathrm{z}_{\mathrm{agn}} - \mathrm{z}_{\mathrm{neigh}} = 0.1(1 + \mathrm{z}_{\mathrm{agn}}).$$

The redshift constraint is minimised to 0.1 for AGN with z $\approx$ 0 because it is the mean photo-z error of the AGN sample. We choose to build the sample based on SCR = $120''.0$. In general, it is best to maximise on this parameter to increase the probability of matching companion sources. This also increases the quantity of companion sources matched. The loss in AGN due to the edge-cut is 98.6% on the SCR = $120''.0$ search. This cut will not impact the AGN sample drastically since it is only 1.3% less than the number of sources left after the surveys edges are cut when SCR = $20''.0$.

2.6 Control Sample

The control sample consists of sources from the combined SDSS-UKIDSS catalogue matched to each AGN in terms of stellar-mass (M_* represented by K_s magnitude Gavazzi, 1993) and redshift (z). This condition places limits on the number of control galaxies an AGN matches with. For the sake of uniformity, we cap the number of control galaxies per AGN at 10. We consider a minimum of 2 control galaxies because statistical measures such as the median, mean and standard deviation (which cannot be calculated on samples of 1) are calculated on each set of control galaxies assigned per AGN. A a result, our analysis includes AGN with between $2 - 10$ control galaxies each.

As stated before, the control galaxies are also selected at projected separations of $> 60''.0$ from their associated AGN. The projected distance limit is applied to distinguish between local density (AGN) and field density (control). The field density exists to provide a standard of comparison for local density that is independent of M_* and redshift.

We approximate M_* via the petrosian K_s magnitude in UKIDSS which we know to be K_s as a proxy for M_*. This has been deduced by Gavazzi (1993), who used the 21cm Tully-Fisher (TF) relation for a nearby galaxy sample. For these, H and B-band magnitudes in the sample are graphed as functions of 21cm line velocities. Linear fits to both H and B slopes are found to be, 3.21 ± 0.12 and 2.05 ± 0.12 respectively. A TF slope of ~ 4 indicates a constant mass-to-light (M/L) ratio (Aaronson et al., 1979). In Gavazzi (1993), the M/L ratio for the H magnitude is constant. Leading to the conclusion that the near-IR magnitudes such as H and K_s are more reliable for tracing M_* than optical bands such as U,B,V. A fair majority of the radio sources in this work have extended light-profiles. We, thus, incorporate petrosian magnitudes to account for varying surface-brightness distribution.

M_*-matching between AGN and control galaxies prevents false correlations between environment and AGN properties being found since galaxy mass is known to correlate strongly with environment (Park and Choi, 2009). For instance, the most massive, early-type, elliptical galaxies are generally observed in cluster regions that are dense. It follows that, without a proper M_*-constraint, correlations between environment and mass bias results (Sabater et al., 2013).

Both K_s from UKIDSS and photo-z from SDSS are constrained by carefully selected parameters. The AGN and control galaxies M_* should match as closely as possible hence we limit differences between their petrosian Ks magnitudes using a parameter we call ε_{K_s}. This is shown in equation 2.3. Redshift is constrained in a similar way except a factor of (1+z) is included in the equation. This is because observed Δz in equation 2.4 increases with redshift. Hence, (1+z) accounts for the fact that redshift estimation becomes less uncertain with increasing redshift.

$$\Delta K_s = K_{s,agn} - K_{s,cont} \leq \varepsilon_{K_s} \tag{2.3}$$

$$\Delta z = z_{agn} - z_{cont} \leq \varepsilon_z (1 + z_{agn}) \tag{2.4}$$

We run the algorithm to search for control galaxies using ε_{K_s} and ε_z combinations with values from the subsets, $\varepsilon_{K_s} = \{0.05, 0.1\}$ and $\varepsilon_z = \{0.05, 0.1\}$. The purpose is to determine which combination will provide matches that yield the most control galaxies. The algorithm runs four different control searches. In each of these, the number of control galaxies matched differs. The statistics related to each search are shown in Table 2.7.

There is a total of 2716 AGN in the JVLA-SDSS-UKIDSS catalogue. The control count is a cumulative total of all control galaxies found for every AGN in the JVLA-SDSS-UKIDSS combined catalogue. The control maximum is the total number of control galaxies that would occur if every AGN in the catalogue matched to 10 control galaxies. A percentage of the control maximum, each control count represents is given in brackets.

The redshift constraint between a control galaxy (cont) and neighbouring (neigh) sources is given by equation 2.2 such that, $\Delta z = z_{cont} - z_{neigh} = 0.05(1+z_{cont})$. In Table 2.7, control galaxy statistics from the four combinations of parameters, ε_{K_s}, ε_z is shown. The purpose of this selection is to find the combination that maximises control count while also reducing bias in the control density measure. We look the distributions for the

AGN (%)	control (%)	control maximum	ε_{z}	$\varepsilon_{\mathrm{K_s}}$
2714 (99.93)	27121 (99.92)	27140	0.05	0.05
2715 (99.96)	27131 (99.93)	27150	0.05	0.1
2715 (99.96)	27142 (99.97)	27150	0.1	0.05
2715 (99.96)	27148 (99.99)	27150	0.1	0.1

TABLE 2.7: Each iteration carries a unique combination of ε_{z} and $\varepsilon_{\mathrm{K_s}}$. For each of these, total AGN (with ≥ 2 control galaxies assigned) and total control galaxy counts are shown. The AGN count is also given as a percentage of the total number of JVLA-SDSS-UKIDSS sources (2716). The total control galaxy count is expressed as a percentage of the control maximum in each case as well.

differences between $\mathrm{K_s}$ and z for AGN and control galaxies. The distributions that are most symmetric indicate the best suited combination of values.

For $\varepsilon_{\mathrm{K_s}}$, the distributions to examine are shown in Fig.'s 2.13 and 2.13. A greater level of symmetry is visible in Fig. 2.13 which is a distribution for the parameter $\varepsilon_{\mathrm{K_s}} = 0.05$. To select ε_{z}, we consider distributions shown in Fig.'s 2.15 - 2.16. Both are anti-symmetric, peaking in the $\mathrm{z_{cont}} < \mathrm{z_{agn}}$ region. Hence, the value of ε_{z} may be 0.01 or 0.05.

There are 27142 control galaxies for the $\varepsilon_{\mathrm{K_s}}, \varepsilon_{\mathrm{z}} = \{0.05, 0.1\}$ combination. In comparison, there are 27121 control galaxies when $\varepsilon_{\mathrm{K_s}}, \varepsilon_{\mathrm{z}} = \{0.05, 0.05\}$. Given the conclusions drawn from the distributions and our interest in maximising the control count, we select the combination, $\varepsilon_{\mathrm{K_s}}, \varepsilon_{\mathrm{z}} = \{0.05, 0.1\}$. Hence, to construct the control galaxy sample, we use the constraints $\varepsilon_{\mathrm{K_s}} = 0.05$ and $\varepsilon_{\mathrm{z}} = 0.1$ in equations 2.3 and 2.4.

For each control galaxy, we implement neighbour search in SDSS. The statistics for this are summarized in table 2.8. We find that for search radii $> 60''.0$, all control galaxies have neighbouring sources. To measure the field density for each AGN, we average over surface-densities of the control galaxies associated to that AGN. Hence the field surface-density ($\Sigma_{\mathrm{field,i}}$) of the i^{th} AGN is the average Σ_{N} over m control galaxies and can be expressed as,

$$\Sigma_{\mathrm{field,i}} = \sum_{\mathrm{k=1}}^{\mathrm{m}} \frac{\Sigma_{\mathrm{N,k}}}{\mathrm{m}}.$$

The fact that the field density is an average makes biasing from edge-effects contribute minimally. Hence, we do not flag control galaxies at the edge of the survey.

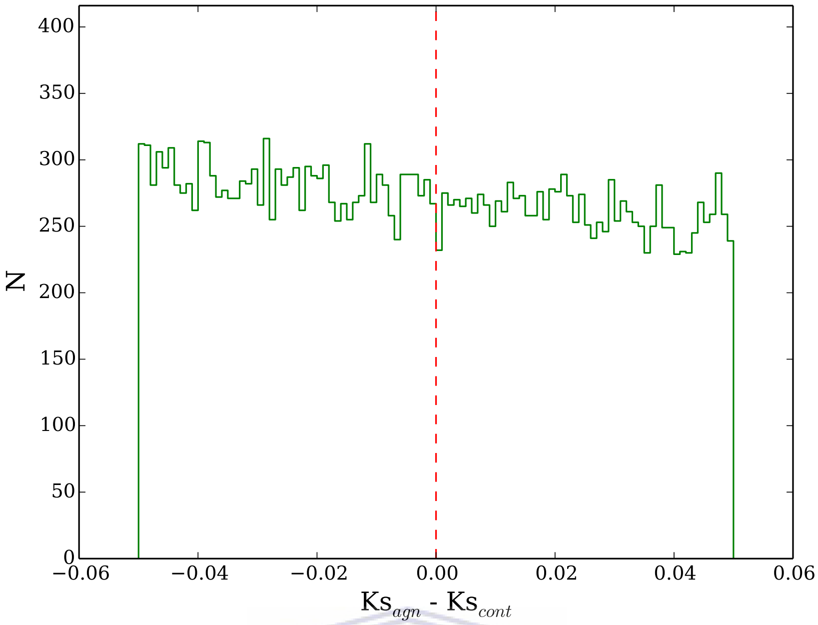

FIGURE 2.13: $K_{s,agn} = K_{s,cont}$ along the central axis (dotted red line).

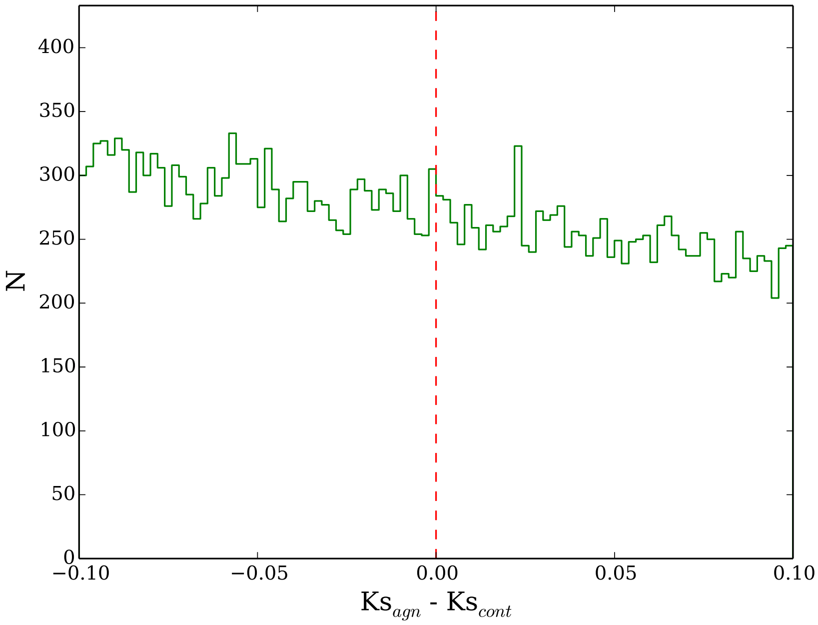

FIGURE 2.14: $K_{s,agn} = K_{s,cont}$ along the central axis (dotted red line).

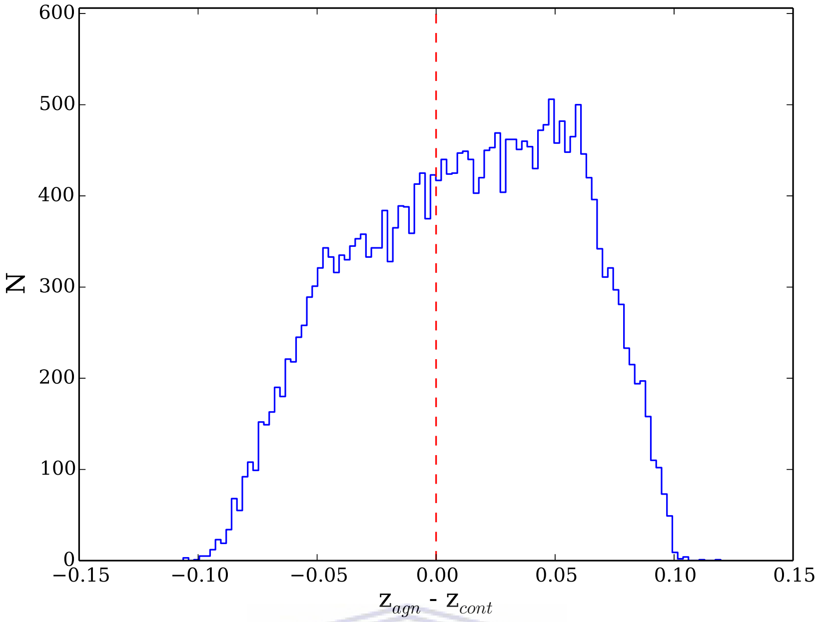

FIGURE 2.15: $z_{agn} = z_{cont}$ along the central axis (dotted red line).

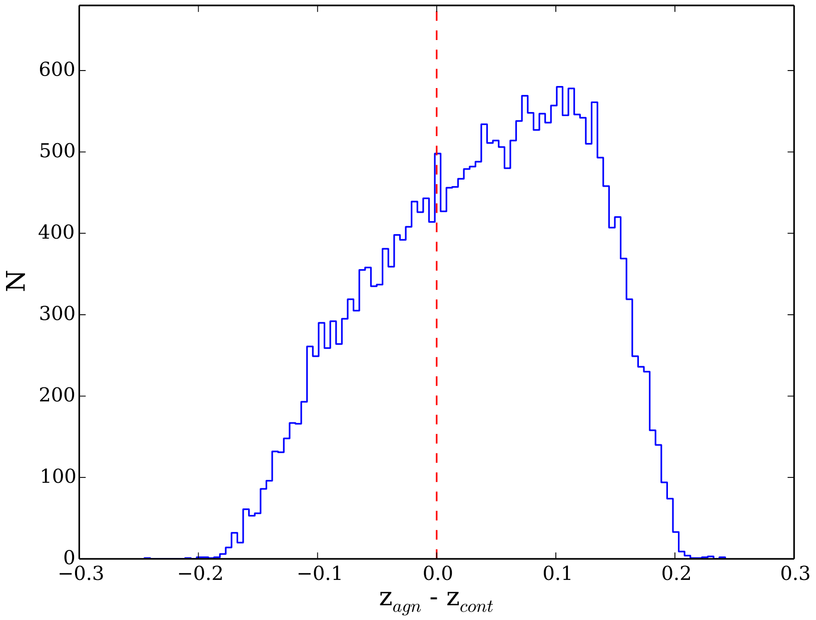

FIGURE 2.16: $z_{agn} = z_{cont}$ along the central axis (dotted red line).

SCR	Control Galaxies without Neighbours (%)
20	343 (1.26)
30	34 (0.125)
40	8 (2.95×10^{-2})
50	1 (3.68×10^{-3})
60	0 (0)
70	0 (0)
80	0 (0)
90	0 (0)
100	0 (0)
120	0 (0)

TABLE 2.8: Control galaxies with neighbours for increasing SCR when $\varepsilon_{\mathrm{z}} = 0.1$ and $\varepsilon_{\mathrm{K_s}} = 0.05$. In total there are 27142 control galaxies. The percentage of sources without neighbours out of this total is shown in brackets.

2.7 Summary

We have described in full, the method used to measure the surface-density parameters of AGN and control galaxies. We have also cited the surveys from which our datasets have been extracted. The technical aspects of instruments used to carry out the surveys were described. We have explained how sources in the JVLA radio catalogue are cross-matched with SDSS optical, WISE mid-IR and UKIDSS near-IR data in order to create a multiwavelength dataset. We have also discussed the method for measuring environment density as well as the algorithm used to obtain lists of nearest neighbouring galaxies to our AGN and control galaxies. The criteria used to compile AGN and control samples has been outlined in detail and the reasoning behind our choices has also been given.

Chapter 3

WISE Results

In the mid-IR continuum, certain features and attributes of the radio AGN in our sample are revealed. WISE photometry[1] specifically is used to deduce AGN classification and morphology. We consider the 22 μm (W4) luminosity ($L_{22\mu\mathrm{m}}$) to be a reasonable diagnostic for dichotomising radio source samples into the jet-mode (LERG) and radiative-mode (HERG) galaxies (Gürkan et al., 2014). The reliability of this threshold is tested by comparing it to the classification method used on Best and Heckman (2012) low-redshift SDSS radio sources. Where optical ionisation and emission line diagnostics are used to determine accretion-mode.

---

[1] Vega calibration is used on the WISE bands.

3.1 WISE Photometry of a radio-loud AGN Sample

To check the viability of the Gürkan et al. (2014) method for classifying radio sources into LERGs and HERGs. We do this using the SDSS radio AGN sample presented in Best and Heckman (2012). This sample is taken from a catalogue constructed by cross-matching SDSS DR7 data with NVSS and FIRST. Obtaining WISE counterparts to the radio AGN by cross-matching this SDSS radio catalogue with WISE, we plot WISE two-colour diagrams with axes identical to those in Gürkan et al. (2014). In one instance, the SDSS radio sources are classified into accretion-modes using optical ionisation and emission line ratios (shown in Fig.'s 3.1 and 3.3) (Best and Heckman, 2012). In the other, they are classified via the 22 μm luminosity such that radio sources above the $L_{22\mu m} = 5 \times 10^{43}$ erg/s threshold are likely to be HERGs and those below it, LERGs (as seen in Fig.'s 3.2 and 3.4) (Gürkan et al., 2014).

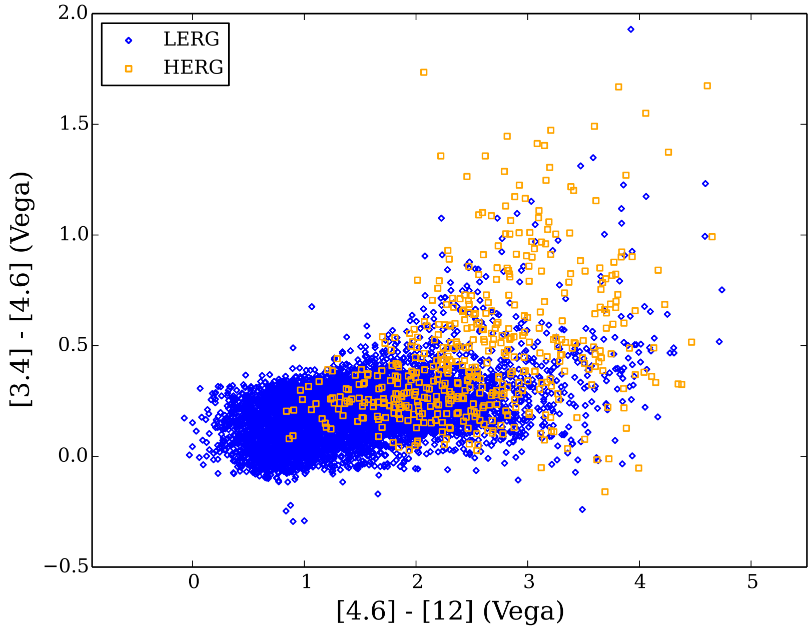

FIGURE 3.1: WISE two-colour diagram of Best and Heckman (2012) sample. Ionisation and emission line diagnostics from literature determine accretion-mode.

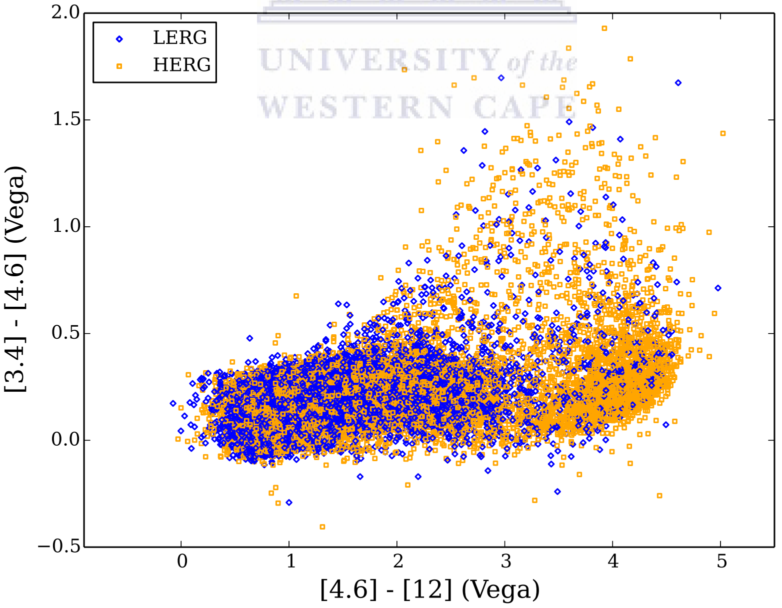

FIGURE 3.2: WISE two-colour diagrams of Best and Heckman (2012) sample. W4-luminosity threshold from Gürkan et al. (2014) classifies Best and Heckman (2012) sources into accretion-modes. Overlap is greater in comparison to Fig. 3.1.

Comparing Fig.'s 3.1 with 3.2 and Fig.'s 3.3 with 3.4, we conclude that the Gürkan et al. (2014) method for determining accretion-mode does not work well on the Best and Heckman

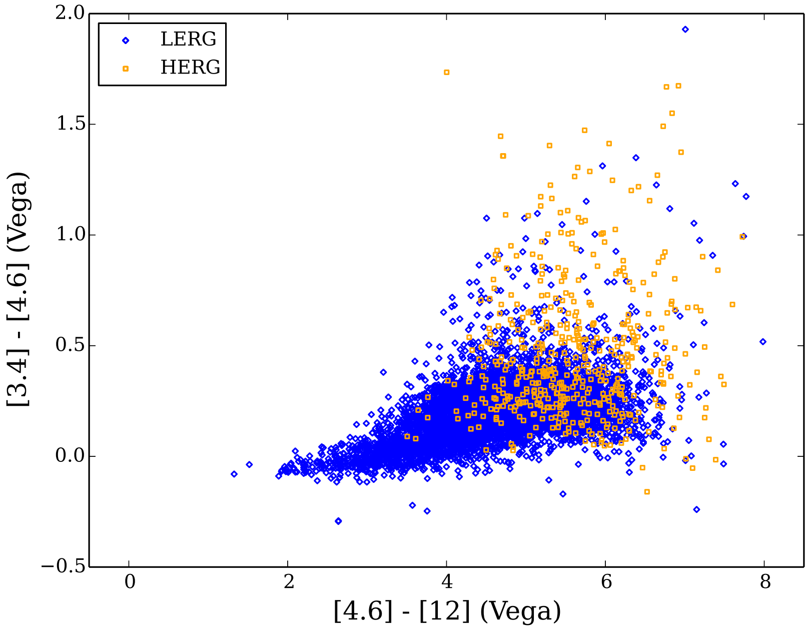

Figure 3.3: WISE two-colour diagram of Best and Heckman (2012) sample. Ionisation and emission line diagnostics from literature determine accretion-mode.

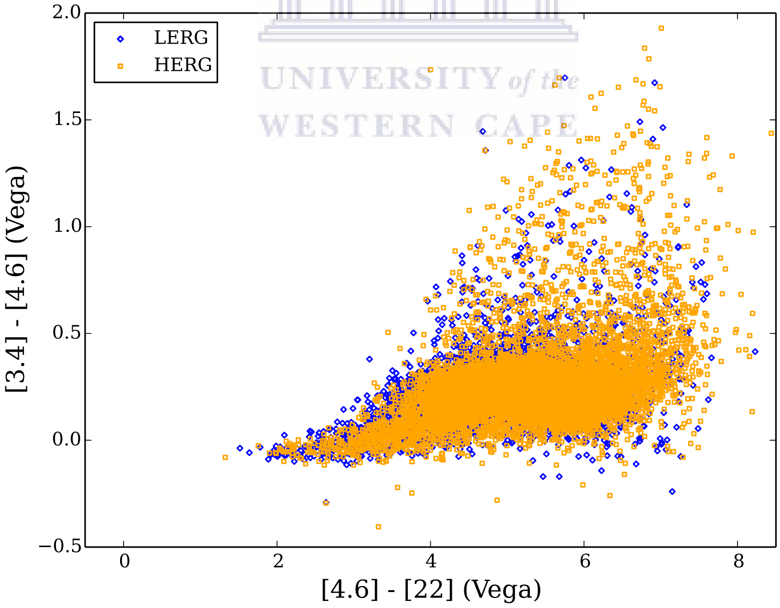

Figure 3.4: WISE two-colour diagrams of Best and Heckman (2012) sample. W4-luminosity threshold from Gürkan et al. (2014) classifies Best and Heckman (2012) sources into accretion-modes. Overlap is greater in comparison to Fig. 3.3.

(2012) SDSS radio source sample. Based on this finding, we argue that the method may also be inadequate for classifying the JVLA radio sources in our sample and we do not apply it to our mid-IR analysis.

3.2 WISE Mid-IR Two-colour Diagrams

Mid-IR wavelength detections are a good tracer for dust. This is because UV-optical from stars in a radio galaxy can be absorbed and re-emitted by dust grains in the circumnuclear torus. From WISE two-colour diagrams, we may be able to extract morphological details about dusty AGN based on their position on the diagram. In Fig.'s 3.5 and 3.6, we classify radio sources using the luminosity threshold, $L_{1.4\text{GHz}} = 10^{26}$ W/Hz, above which AGN are classified as HERGs and below it, as LERGs.

This threshold has been derived from local NVSS radio-luminosity functions. In this we see that both HERGs and LERGs exist across the full $L_{1.4\text{GHz}}$-range probed in Best and Heckman (2012) i.e. $10^{22}-10^{27}$ W/Hz. The luminosity functions, however, also suggest that HERGs comprise the majority of the radio source population $> 10^{26}$ W/Hz (shown in Fig. 1.5) (Best and Heckman, 2012).

We use this finding to define 10^{26} W/Hz as the point at which accretion-mode is likely to switch from being LERG to HERG in our own radio source sample. There is, of course, a possibility that LERGs exist above this threshold. Hence, a rigorous classification involving ionisation and emission lines would be needed to obtain the most ideal accretion-mode distribution. The radio-luminosity method is merely an approximate classifier we conclude to be sufficient in this context.

Using this method to classify the radio AGN into accretion-modes, LERGs are found to outnumber HERGs by a tremendous margin. This is highlighted in Table 3.1 where a brief statistical breakdown of the WISE-detected radio sources is given.

Accretion-mode	Count (%)
HERG	47 (1.38)
LERG	3367 (98.6)

Table 3.1: Bimodal accretion-mode counts. WISE detects 3414 in all four WISE bands. Each count is shown as a percentage of the initial 4130 JVLA-SDSS radio sources.

When we overlap the morphological designations of Fig. 12 in Wright et al. (2010) onto Fig. 3.5, HERGs are found to coincide with spiral and obscured AGN portions of the diagram while LERGs appear to be scattered throughout it, emerging under all three morphological designations shown. A similar proportion of HERGs are incident in the obscured AGN and spiral areas of the two-colour diagram as indicated by Table 3.2.

We know that thermal re-emission by dust provides an approximate link between this mid-IR emission and star-formation (SF) (Buat et al., 2002; Dominguez et al., 2013). Hence, the fact that HERGs are incident in the *dust-obscured* and *spirals* (where SF is more likely) sectors of the diagram may be an indicator of dust abundance rather than galaxy morphology. This is a more reasonable explanation for what we observe, given the fact that HERGs have been found to reside in massive ellipticals with only residual SF occurring (Hardcastle et al., 2013; Herbert et al., 2010).

Similarly, Fig. 3.6 reinforces the notion that HERGs are likely to have dust-obscured nuclei since the majority of them (51%) are found in portions on the diagram that indicate this. We find that 49% of WISE-detected HERGs occupy the spiral sector in Fig. 3.5. LERGs, on the other hand, do not follow any similar pattern but comprise 100% of the elliptical population in fig. 3.5.

The diagram does not yield sufficient information about LERGs and this may be because of how we determine accretion-mode i.e. using only the radio-luminosity. Optical spectra would properly distinguish what classes of AGN exist with $L_{1.4\mathrm{GHz}} < 10^{23}$ W/Hz. There is a possibility that within this population, what we currently call LERGs are, in fact, a variety of different AGN classes.

In Fig.'s 3.7 - 3.10, we show WISE 3.4, 4.6, 12 and 22 μm luminosities as a function of redshift. In all of these, LERGs exist across the full mid-IR luminosity range while HERGs tend to only be found at the upper end of the WISE luminosity range. On the 22 μm luminosity-redshift plane (Fig. 3.10), all HERGs are found $> 5 \times 10^{43}$ erg/s. However, a significant number of LERGs also exceed this threshold. This diagnostic, therefore, only appears to work for sources at the upper end of the radio luminosity range. Since high-power sources such as these are predicted to have a greater dust abundance than those in the low-luminosity range, it is possible that a selection bias makes only those sources with sufficient dust classifiable via WISE data.

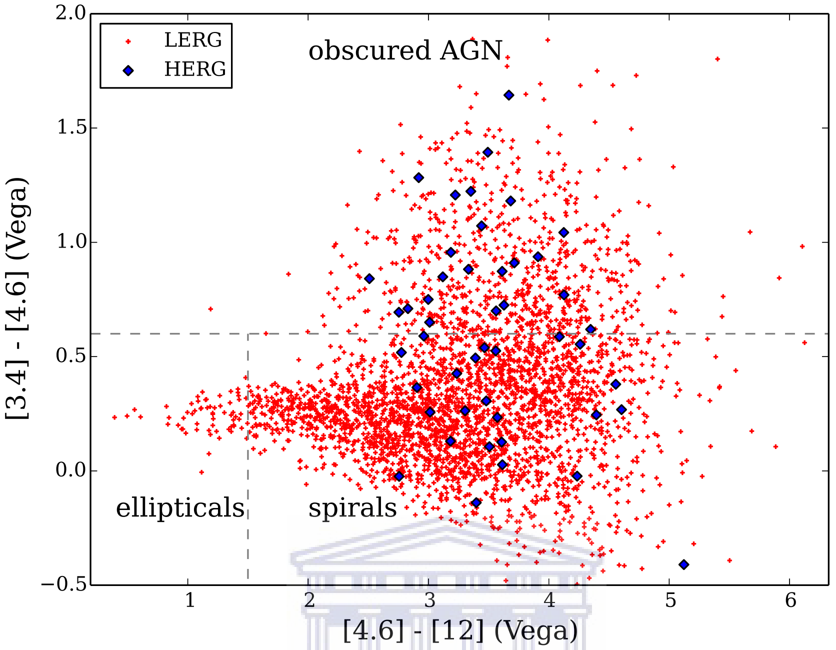

FIGURE 3.5: WISE two-colour diagram, W12 vs W23 for JVLA-SDSS-WISE sample. The bounds of the WISE two-colour plot (fig. 12 of (Wright et al., 2010)) are applied. [3.4]-[4.6] $>$ 0.6 represents sources with obscured AGN, [3.4]-[4.6] $<$ 0.6 and [4.6]-[12] $<$ 1.5 denotes sources with elliptical morphologies, [3.4]-[4.6] $<$ 0.6 and [4.6]-[12] $>$ 1.5 have spiral morphologies. HERGs (blue diamonds) are thus likely to be spiral and dust-obscured while LERGs (red markers) fall under all three morphologies on the plot due to insufficient dust for thermal re-emission.

Accretion-mode	Obscured	Spirals	Ellipticals	Total
HERG	24 (0.510)	23 (0.489)	0 (0)	47
LERG	732 (0.217)	2572 (0.764)	63 (0.0187)	3367

TABLE 3.2: JVLA-SDSS-WISE radio source counts under each type/morphology designation in Fig. 10 of Wright et al. (2010). Each count is shown as a percentage of the total for HERGs and LERGs given in Table 3.1. Full classification is shown in Fig. 3.5.

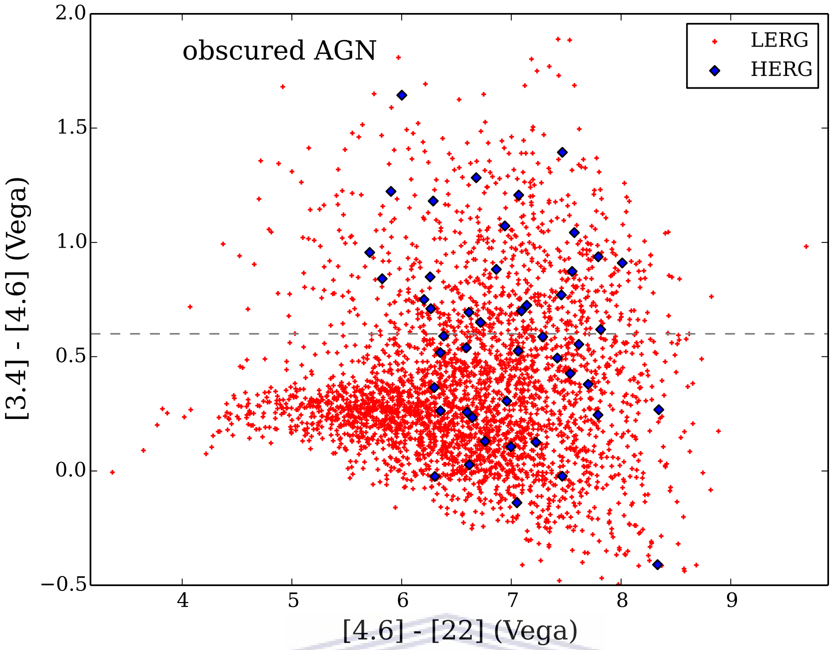

FIGURE 3.6: WISE two-colour diagram, W12 vs W24 for JVLA-SDSS-WISE. [3.4]-[4.6] > 0.6 denotes sources with obscured AGN. The [4.6]-[22] axis has no significance to WISE classification in this case. Neither HERG (blue diamonds) nor LERG (red markers) complies to any specific section of the diagram.

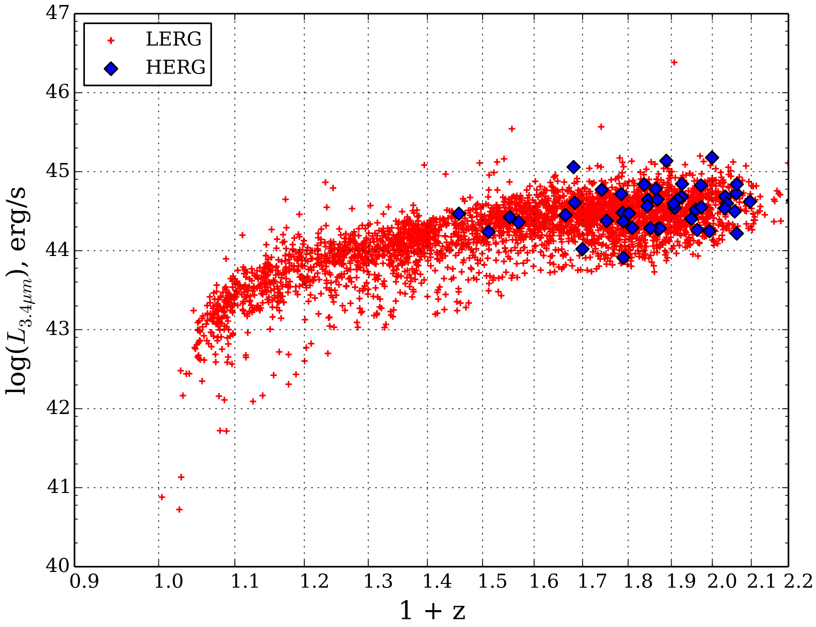

FIGURE 3.7: W1 (3.4 μm) luminosity as a function of 1+z (offset redshift).

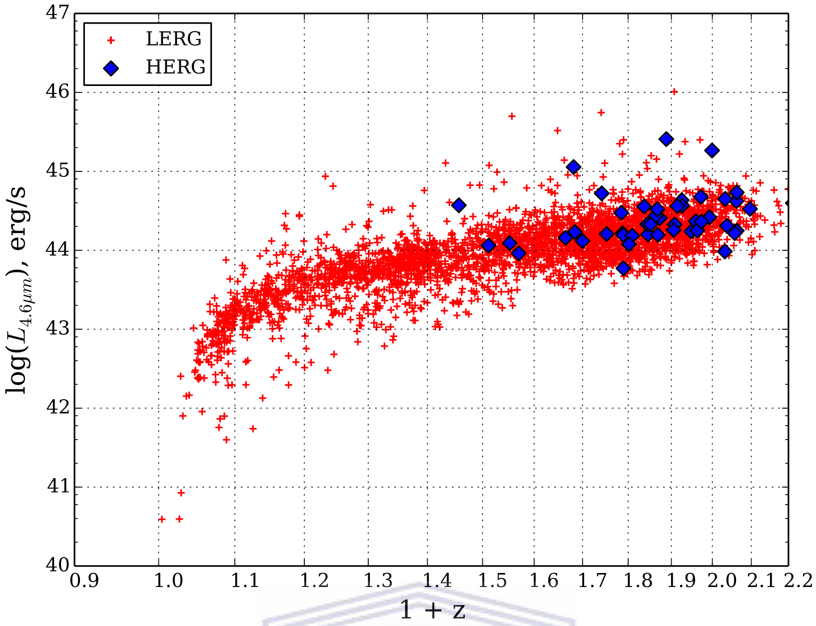

FIGURE 3.8: W2 (4.6 μm) luminosity as a function of 1+z (offset redshift).

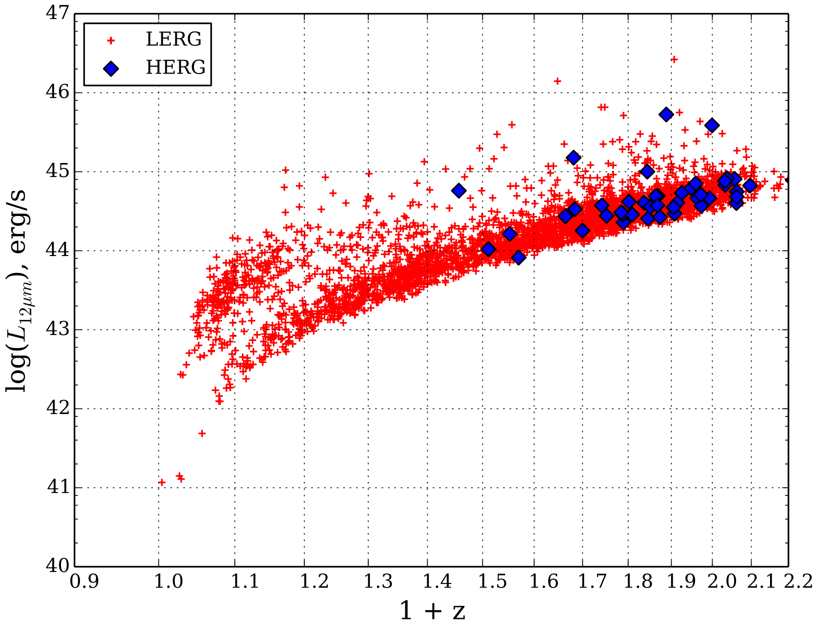

FIGURE 3.9: W3 (12 μm) luminosity as a function of 1+z (offset redshift).

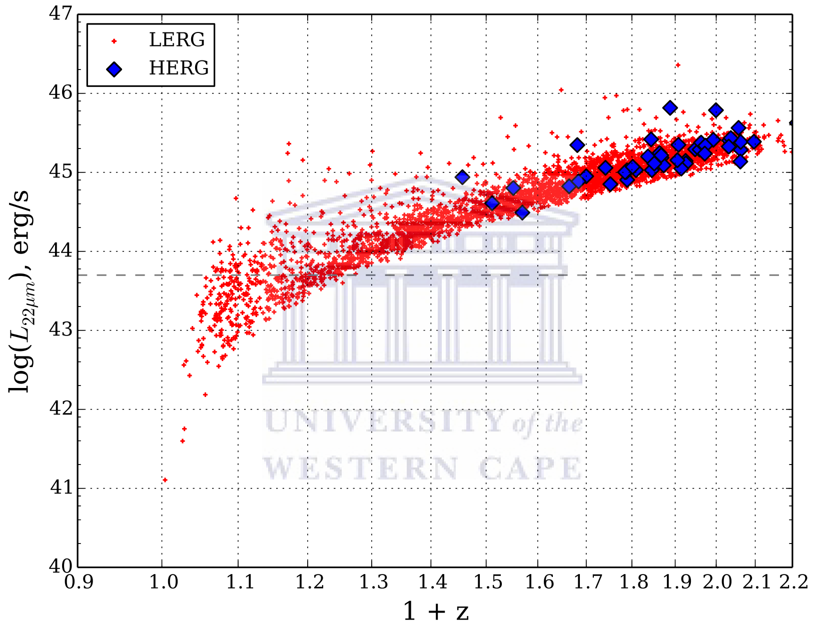

FIGURE 3.10: W4 (22 μm) luminosity as a function of 1+z (offset redshift). The dashed grey line represents the WISE accretion-mode diagnostic for RL AGN i.e. $L_{22\mu\text{m}} = 5 \times 10^{43}$ erg/s (Gürkan et al., 2014). All HERGs are consistent with this threshold. LERG contamination is seen above the line as well.

Chapter 4

Environment Results

In this chapter, we investigate the role of environment on altering the rate of accretion in radio AGN. The outline on accretion-mode given in Section 1.4 describes the way that accretion rate differs for jet-mode (LERG) and radiative-mode (HERG) sources. Accretion rates are faster in HERGs than they are in LERGs. Because accretion rate and radiative accretion efficiency are proportional to each other, we can use radio power to roughly approximate accretion-mode.

We do this using a 1.4 GHz radio luminosity ($L_{1.4\text{ GHz}}$) threshold which states that radio sources with $L_{1.4\text{ GHz}} > 10^{26}$ W/Hz are most likely HERGs and those below it, LERGs. It follows that those below the threshold are LERGs. To quantify environment, we calculate projected surface-density, Σ_N, given by equation 2.1 (constrained in redshift) for all AGN and control galaxies. Averaging the surface-density over mass and redshift-matched control galaxies for each AGN gives us field density. Comparing AGN and field densities provides a relative measure of the galaxy density around each AGN. Using this, we examine AGN galaxy density as a function of $L_{1.4\text{ GHz}}$.

Our analysis is comparative in that we are mostly interested in examining our findings in light of previous works that are similar. We divide our JVLA radio sample into two redshift intervals. We call these the low ($0.1 < z < 0.2$) and intermediate ($0.2 < z < 1.2$) redshift intervals. The low redshift interval has been created with the purpose of comparing our results to those in other low-redshift AGN studies using radio survey data spanning redshift ranges of $0.03 < z < 0.1$ (Sabater et al., 2013; Sabater et al., 2015) and $0.01 < z < 0.3$ (Best and Heckman, 2012). We place an upper limit of $z = 0.2$ on the low redshift sub-sample because it strikes a good balance between upper redshift limits in studies we compare our work to. The lower limit, $z \sim 0.1$, and upper limit, $z \sim 1.2$ are imposed on the radio sample due to minimal source contributions at $z < 0.1$ and $z > 1.2$. This is made clear in the JVLA-SDSS redshift distribution (Fig. 2.7) where significant drops in the quantities of detected sources occur.

The low and intermediate intervals span 0.1 and 1.0 deep in redshift-space, respectively. Although the intervals are not equal in depth, they are each broad enough to provide the statistical information we need for this analysis. This is because the sample sizes in each case are large enough to alleviate the detrimental effects brought about by large photometric redshift errors.

The intermediate redshift interval is larger and not divided into smaller increments because there are no comparable results from previous works available for comparison. This is because the relation between galaxy density and $L_{1.4\,\mathrm{GHz}}$ has yet to be analysed on radio sources with redshifts of up to $z \sim 1.2$. The significance of our results are quantified using Spearman's rank correlation parameters.

4.1 1.4 GHz Radio Luminosity and Surface-Density Measure

We investigate the link between local galaxy densities of the radio AGN and their accretion-mode classification (HERG or LERG) as approximated $L_{1.4\mathrm{GHz}}$. The choice for this rough classification method is motivated by Fig. 1.5. In this diagram, NVSS low-redshift radio luminosity functions indicate that for 1.4 GHz luminosities $> 10^{26}$ W/Hz, HERGs are more prevalent than LERGs. This allows us to assume that in our own radio sample, HERGs also comprise the majority $> 10^{26}$ W/Hz in the local universe.

To estimate the local density of each radio AGN, we use Σ_N (equation 2.1) the surface-density parameter, a function of the nearest neighbour distance, $\mathrm{d_N}$. Surface-density is calculated for distances to the 2nd and 5th companion sources i.e. $\mathrm{N} = \{2, 5\}$. This yields density measures in groups containing 3 and 6 galaxies (including the AGN host galaxies), respectively. The surface-densities we measure are Σ_2 and Σ_5. We calculate them for AGN and control sample (discussed in Sections 2.5 and 2.6). The calculated densities are denoted by $\Sigma_\mathrm{N,AGN}$ and $\Sigma_\mathrm{N,field}$, for each AGN we quantify galaxy density for.

By comparing $\Sigma_\mathrm{N,AGN}$ and $\Sigma_\mathrm{N,field}$, we determine the level of clustering in the local environment of an AGN. As explained in Section 2.6, the AGN and control galaxies are matched in terms of M_* and redshift in order to excise effects linked to the mass-density relation (Park and Choi, 2009) as well as cosmic evolution (Best and Heckman, 2012) biases.

We call this comparison the relative density and quantify it using ratios and differences. The ratios (R) are denoted by $\Sigma_\mathrm{N,R} = \Sigma_\mathrm{N,AGN}/\Sigma_\mathrm{N,field}$ and differences (D) by $\Sigma_\mathrm{N,D} = \Sigma_\mathrm{N,AGN} - \Sigma_\mathrm{N,field}$. The interpretation states that for $\Sigma_\mathrm{N,R} > 1$ and $\Sigma_\mathrm{N,D} > 0$, AGN environments are denser than the field or 'over-dense'. In the opposite case, AGN environments are less dense than the field or 'under-dense'.

In order to carry out a statistical analysis of the trend between $L_{1.4\mathrm{GHz}}$ and galaxy density, we create $L_{1.4\mathrm{GHz}}$-bins with increasing powers of base 10 (dex units). In each bin, we calculate mean (μ) and median relative density of the binned sample. The mean takes into account every density measure including the outliers. Whereas, the median, provides a statistical middle, that is not biased by outliers. Therefore, in cases where outlying or unusual density values are present, the median provides a better estimation of the average density.

We quantify the significance of binned means using the relation, $\mathrm{N}\sigma = \mu$ in which σ is the standard error on the binned mean (Section A.2). When $|\mathrm{N}| > 3$, i.e. the binned mean has 3σ significance and is considered a reliable measure of the mean relative density in that bin.

To test the correlation between $\mathrm{L}_{1.4\mathrm{GHz}}$ and relative density, a Spearman's rank test is carried out. The parameters, ρ and p quantify significance (or strength) of a correlation. The parameter, ρ ranges from -1 to +1 with positive and negative correlations indicated by their proximity to +1 and -1, respectively. While p indicates whether the null hypothesis should be accepted or not. In cases where $\mathrm{p} < 0.05$, the null hypothesis is rejected. In this context, the null hypothesis states that there is an anti-correlation between the relative density and 1.4 GHz radio luminosity. Hence, when $\mathrm{p} < 0.05$, this correlation is validated.

4.1.1 Low Redshift Interval

We examine the relation between relative density and $L_{1.4GHz}$ for radio AGN in the interval, $0.1 < z < 0.2$. For these AGN, binned medians and means (including their errors) and their statistical significance are summarised in Tables 4.1, 4.2, 4.3 and 4.4. Spearman's rank parameters are also drawn out in Table 4.5. The diagrams for density as a function of $L_{1.4GHz}$ are given in Fig.'s 4.1 - 4.8 for this interval.

$\log_{10} L_{1.4GHz}$-bin	$\mu(\Sigma_{2,R})$ $(\sigma_{\mu(\Sigma_{2,R})})$	median	μ-significance
22 – 23	3.547 (0.0453)	1.302	78.160
23 – 24	8.551 (0.554)	1.479	15.427
24 – 25	2.839 (0.469)	1.795	6.057
25 – 26	1.700 (9.58×10^{-3})	1.700	2.380

Table 4.1: For $\Sigma_{2,R}$ in each $L_{1.4GHz}$-bin, the mean (μ) and its uncertainty (σ_μ), in brackets, are shown as well as the median. These are in kpc^{-2}. Significance of the binned mean (μ-significance) is also given.

$\log_{10} L_{1.4GHz}$-bin	$\mu(\Sigma_{2,D})$ $(\sigma_{\mu(\Sigma_{2,D})})$	median	μ-significance
22 – 23	6.606×10^{-5} (4.497×10^{-6})	1.235×10^{-5}	14.690
23 – 24	1.723×10^{-4} (1.318×10^{-5})	3.165×10^{-5}	13.079
24 – 25	1.615×10^{-4} (4.392×10^{-5})	2.598×10^{-5}	3.678
25 – 26	-2.248×10^{-6} (2.402×10^{-5})	-2.248×10^{-6}	-0.094

Table 4.2: For $\Sigma_{2,D}$ in each $L_{1.4GHz}$-bin, the mean (μ) and its uncertainty (σ_μ), in brackets, are shown as well as the median. These are in kpc^{-2}. Significance of the binned mean (μ-significance) is also given.

$\log_{10}$ L$_{1.4\text{GHz}}$-bin	$\mu(\Sigma_{5,\text{R}})$ $(\sigma_{\mu(\Sigma_{5,\text{R}})})$	median	μ-significance
22 − 23	2.255 (0.0284)	1.309	79.386
23 − 24	2.554 (0.0406)	1.584	62.961
24 − 25	1.689 (0.146)	2.120	11.558
25 − 26	1.477 (0.460)	1.477	3.214

TABLE 4.3: For $\Sigma_{5,\text{R}}$ in each L$_{1.4\text{GHz}}$-bin, the mean (μ) and its uncertainty (σ_μ), in brackets, are shown as well as the median. These are in kpc^{-2}. Significance of the binned mean (μ-significance) is also given.

$\log_{10}$ L$_{1.4\text{GHz}}$-bin	$\mu(\Sigma_{5,\text{D}})$ $(\sigma_{\mu(\Sigma_{5,\text{D}})})$	median	μ-significance
22 − 23	3.738×10^{-5} (1.371×10^{-6})	1.262×10^{-5}	27.263
23 − 24	5.367×10^{-5} (2.101×10^{-6})	2.239×10^{-5}	25.544
24 − 25	4.104×10^{-5} (1.042×10^{-5})	2.993×10^{-5}	3.937
25 − 26	-6.139×10^{-7} (1.368×10^{-5})	-6.139×10^{-7}	-0.045

TABLE 4.4: For $\Sigma_{5,\text{D}}$ in each L$_{1.4\text{GHz}}$-bin, the mean (μ) and its uncertainty (σ_μ), in brackets, are shown as well as the median. These are in kpc^{-2}. Significance of the binned mean (μ-significance) is also given.

surface-density type	ρ	p
$\Sigma_{2,\text{R}}$	0.0981	0.147
$\Sigma_{2,\text{D}}$	0.101	0.136
$\Sigma_{5,\text{R}}$	0.156	0.0294
$\Sigma_{5,\text{D}}$	0.131	0.0669

TABLE 4.5: Spearman's rank correlation coefficients for mean Σ_N when $\text{N} = \{2, 5\}$ per L$_{1.4\text{GHz}}$-bin in the low redshift interval spanning the range $0.1 < \text{z} < 0.2$.

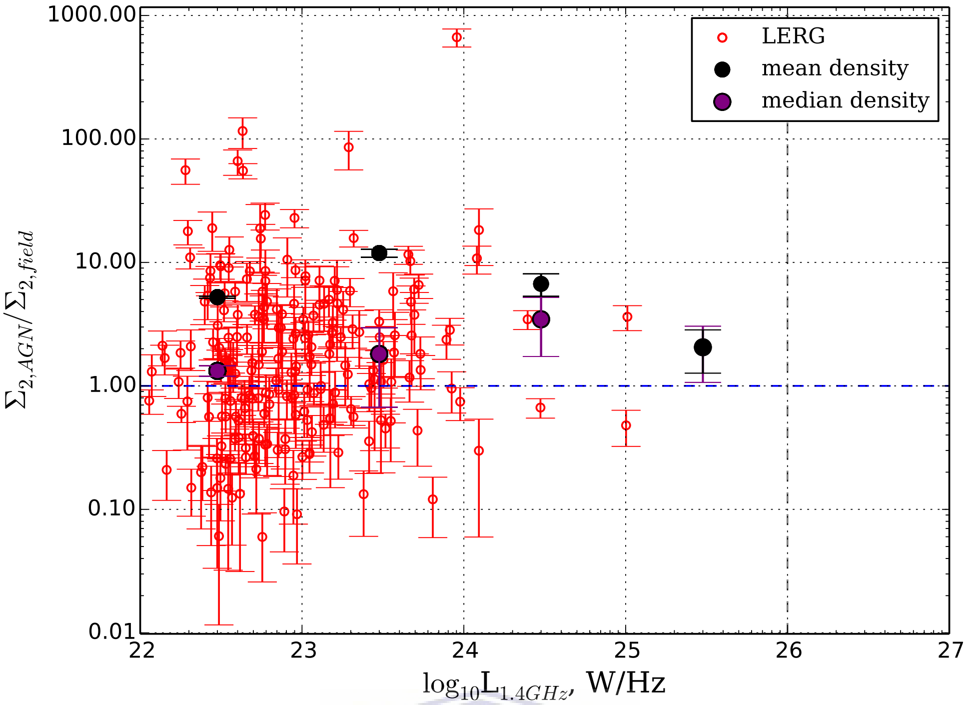

FIGURE 4.1: $\Sigma_{2,\mathrm{R}}$ as a function of $L_{1.4\mathrm{GHz}}$.

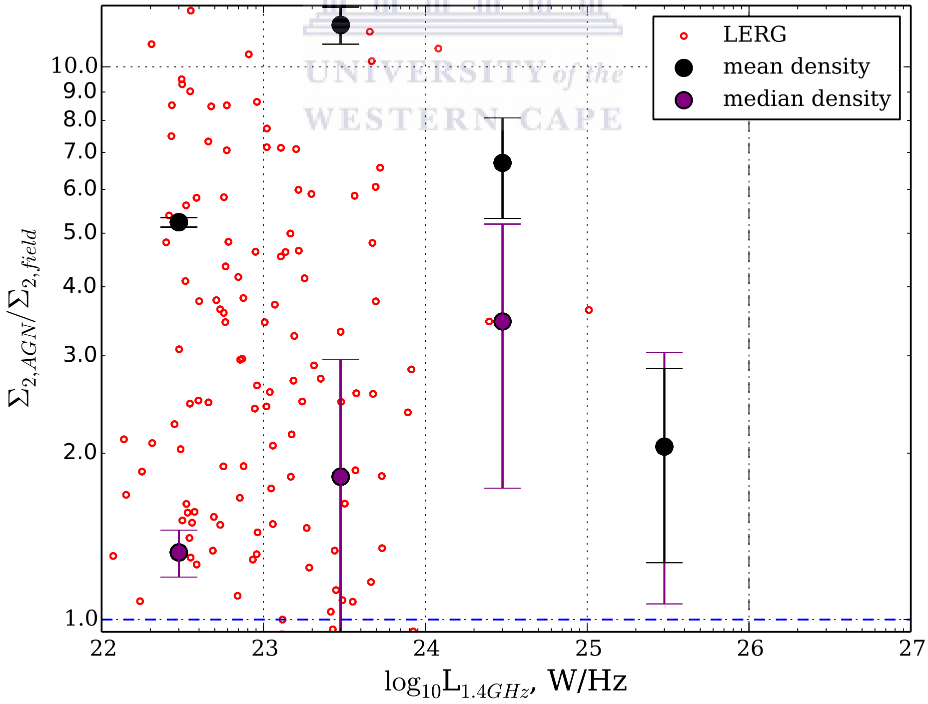

FIGURE 4.2: A magnified rendition of Fig. 4.1.

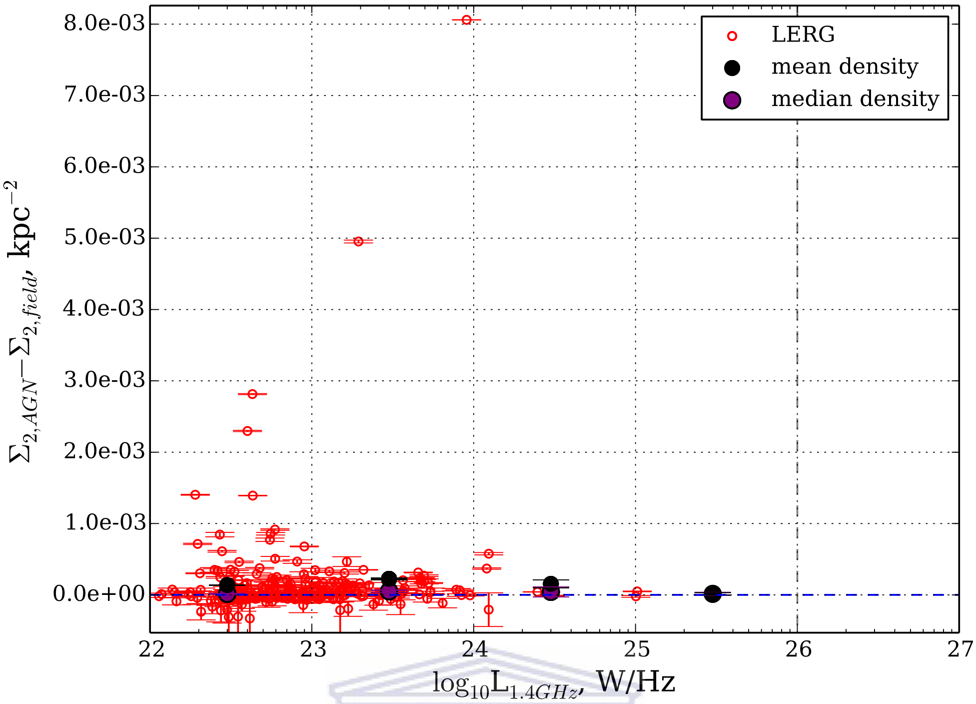

FIGURE 4.3: $\Sigma_{2,D}$ as a function of $L_{1.4GHz}$.

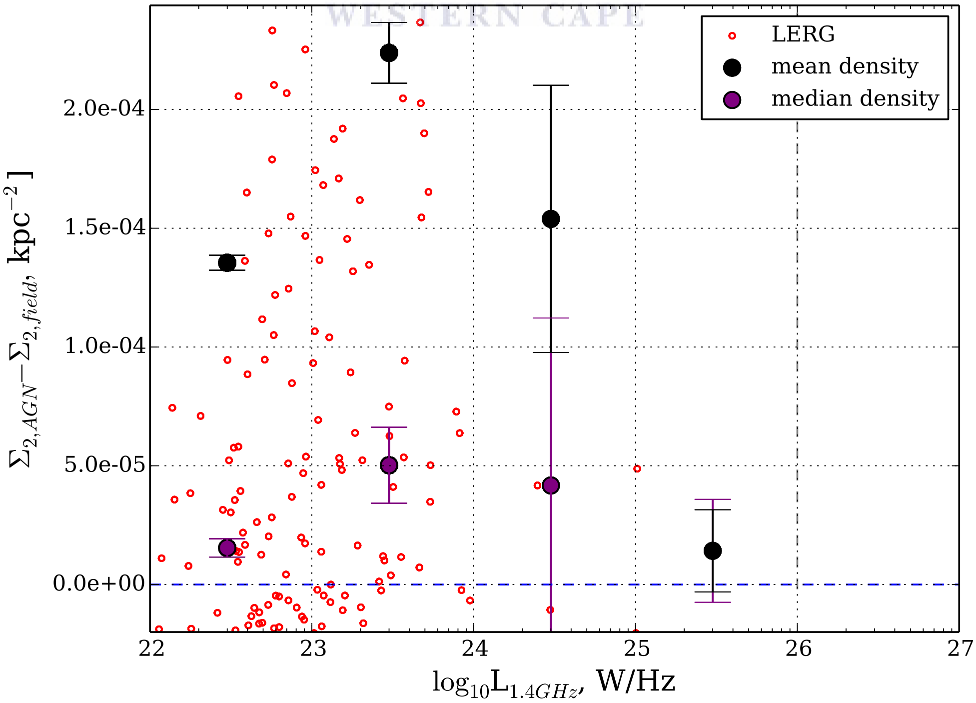

FIGURE 4.4: A magnified version of Fig. 4.3.

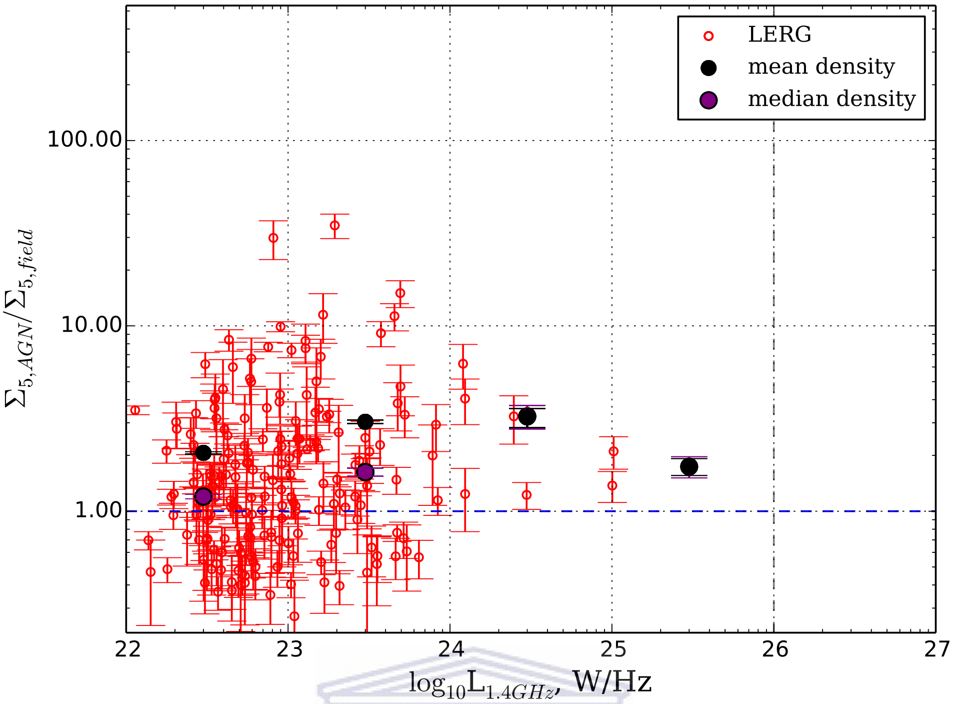

FIGURE 4.5: $\Sigma_{5,\mathrm{R}}$ as a function of $L_{1.4\mathrm{GHz}}$.

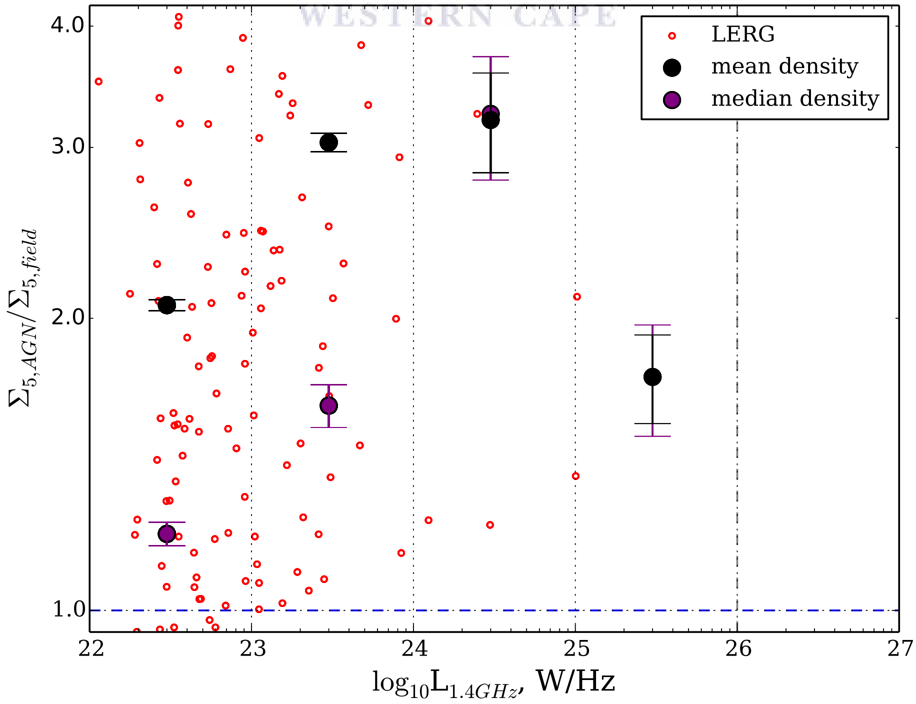

FIGURE 4.6: A magnified version of Fig. 4.5.

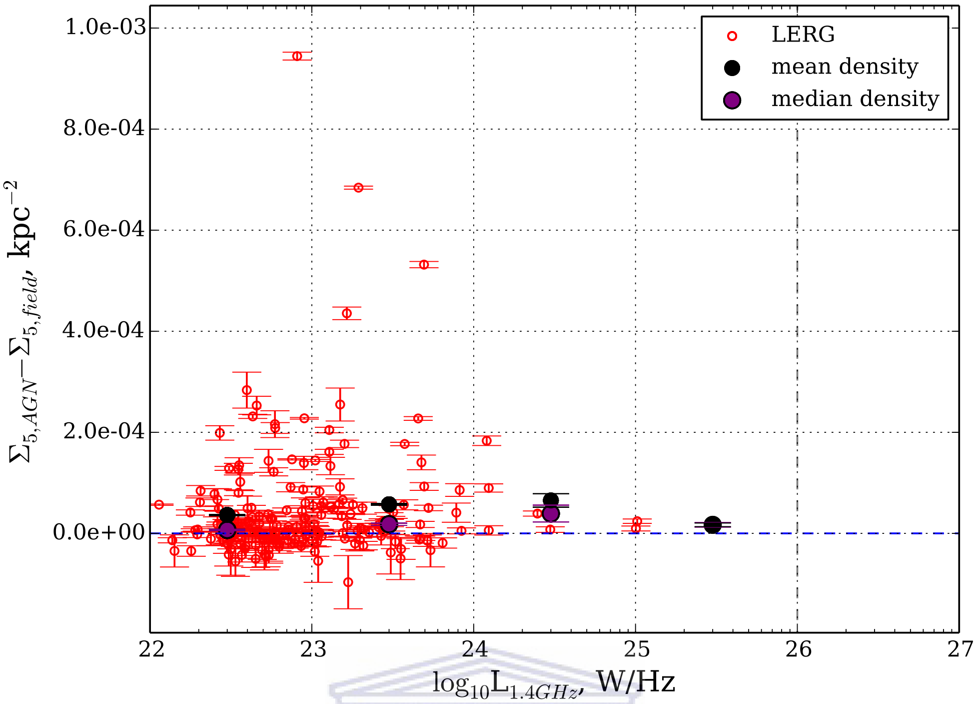

FIGURE 4.7: $\Sigma_{2,\mathrm{R}}$ as a function of $L_{1.4\mathrm{GHz}}$ on a log-scale.

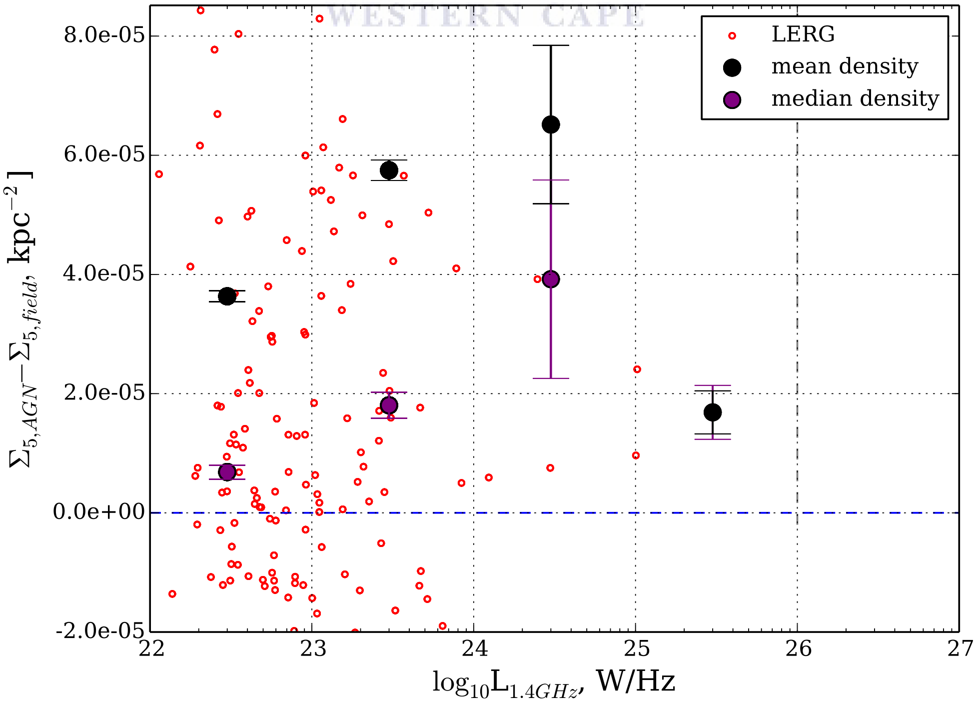

FIGURE 4.8: A magnified version of Fig. 4.7.

4.1.2 Intermediate Redshift Interval

We observe relative density as a function of $L_{1.4GHz}$ over the interval, $0.1 < z < 1.2$. The binned medians, means (including their errors) and their statistical significance are highlighted in Tables 4.6, 4.7, 4.8 and 4.8. Correlation strength is quantified in Table 4.10. In Fig.'s 4.9 - 4.16, relative density as a function of $L_{1.4GHz}$ is depicted.

$\log_{10} L_{1.4\mathrm{GHz}}$-bin	$\mu(\Sigma_{2,\mathrm{R}})$ $(\sigma_{\mu(\Sigma_{2,\mathrm{R}})})$	median	μ-significance
22 – 23	2.674 (0.110)	1.408	24.346
23 – 24	2.832 (7.42×10^{-3})	1.391	381.909
24 – 25	2.737 (2.87×10^{-3})	1.543	954.579
25 – 26	2.463 (9.58×10^{-3})	1.431	257.093
26 – 27	2.608 (0.169)	1.176	15.410

TABLE 4.6: For $\Sigma_{2,\mathrm{R}}$ in each $L_{1.4GHz}$-bin, the mean (μ) and its uncertainty (σ_μ), in brackets, are shown as well as the median. These are in kpc^{-2}. Significance of the binned mean (μ-significance) is also given.

$\log_{10} \mathrm{L}_{1.4\mathrm{GHz}}$-bin (W/Hz)	$\mu(\Sigma_{2,\mathrm{D}})$ $(\sigma_{\mu(\Sigma_{2,\mathrm{D}})})$	median	μ-significance
22 – 23	4.016×10^{-5} (3.980×10^{-6})	2.294×10^{-5}	10.090
23 – 24	5.161×10^{-5} (2.090×10^{-7})	1.301×10^{-5}	246.941
24 – 25	6.011×10^{-5} (1.034×10^{-7})	1.034×10^{-7}	581.302
25 – 26	5.275×10^{-5} (3.691×10^{-7})	3.691×10^{-7}	142.895
26 – 27	3.709×10^{-5} (3.570×10^{-6})	3.570×10^{-6}	10.390

TABLE 4.7: For $\Sigma_{2,\mathrm{D}}$ in each $L_{1.4GHz}$-bin, the mean (μ) and its uncertainty (σ_μ), in brackets, are shown as well as the median. These are in kpc^{-2}. Significance of the binned mean (μ-significance) is also given.

$\log_{10} \mathrm{L}_{1.4\mathrm{GHz}}$-bin (W/Hz)	$\mu(\Sigma_{5,\mathrm{R}})$ $(\sigma_{\mu(\Sigma_{5,\mathrm{R}})})$	median	μ-significance
$22 - 23$	2.377 (0.105)	1.604	22.601
$23 - 24$	$2.312\ (3.44 \times 10^{-3})$	1.656	672.161
$24 - 25$	$2.574\ (2.01 \times 10^{-3})$	1.880	1279.682
$25 - 26$	$2.285\ (6.24 \times 10^{-3})$	1.717	366.001
$26 - 27$	$1.719\ (3.46 \times 10^{-2})$	1.826	49.640

TABLE 4.8: For $\Sigma_{5,\mathrm{R}}$ in each $\mathrm{L}_{1.4\mathrm{GHz}}$-bin, the mean ($\mu$) and its uncertainty ($\sigma_{\mu}$), in brackets, are shown as well as the median. These are in kpc^{-2}. Significance of the binned mean (μ-significance) is also given.

$\log_{10} \mathrm{L}_{1.4\mathrm{GHz}}$-bin (W/Hz)	$\mu(\Sigma_{5,\mathrm{D}})$ $(\sigma_{\mu(\Sigma_{2,\mathrm{D}})})$	median	μ-significance
$22 - 23$	$3.059 \times 10^{-5}\ (2.447 \times 10^{-6})$	1.656×10^{-5}	12.500
$23 - 24$	$2.879 \times 10^{-5}\ (7.391 \times 10^{-8})$	1.498×10^{-5}	389.518
$24 - 25$	$3.814 \times 10^{-5}\ (4.626 \times 10^{-8})$	2.298×10^{-5}	824.510
$25 - 26$	$3.415 \times 10^{-5}\ (1.724 \times 10^{-7})$	1.682×10^{-5}	198.066
$26 - 27$	$1.789 \times 10^{-5}\ (9.808 \times 10^{-7})$	1.662×10^{-5}	18.244

TABLE 4.9: For $\Sigma_{5,\mathrm{D}}$ in each $\mathrm{L}_{1.4\mathrm{GHz}}$-bin, the mean ($\mu$) and its uncertainty ($\sigma_{\mu}$), in brackets, are shown as well as the median. These are in kpc^{-2}. Significance of the binned mean (μ-significance) is also given.

surface-density type	ρ	p
$\Sigma_{2,\mathrm{R}}$	0.0177	0.394
$\Sigma_{2,\mathrm{D}}$	0.0216	0.297
$\Sigma_{5,\mathrm{R}}$	0.0208	0.316
$\Sigma_{5,\mathrm{D}}$	0.0452	0.0293

TABLE 4.10: Spearman's rank correlation coefficients for mean Σ_{N} when $\mathrm{N} = \{2, 5\}$ per $\mathrm{L}_{1.4\mathrm{GHz}}$-bin in the low redshift interval spanning the range $0.1 < \mathrm{z} < 0.2$.

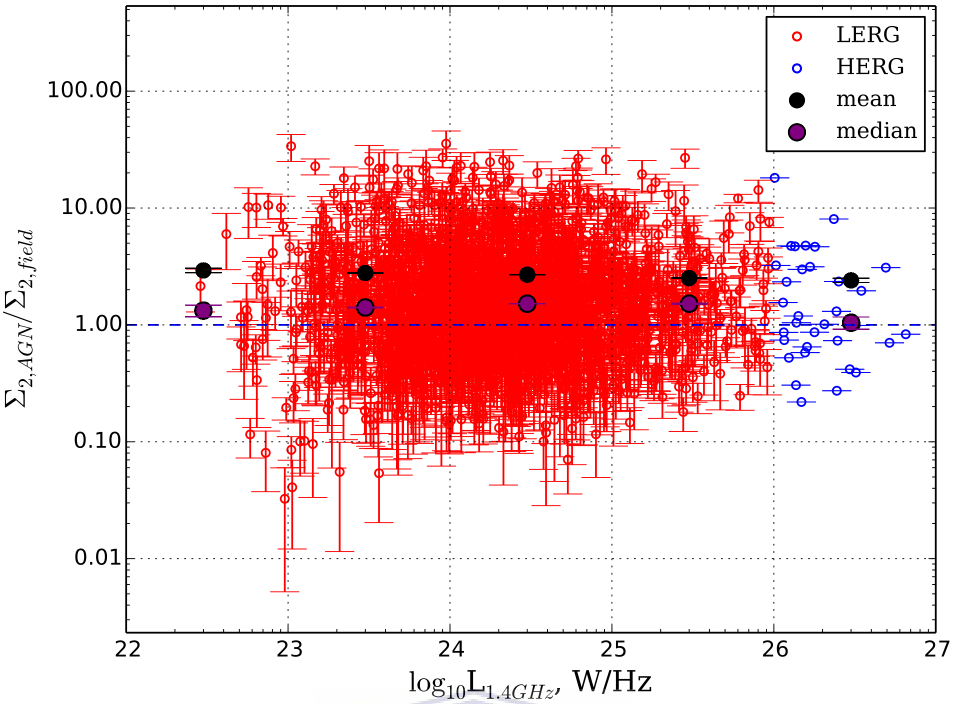

FIGURE 4.9: $\Sigma_{2,R}$ as a function of $L_{1.4GHz}$.

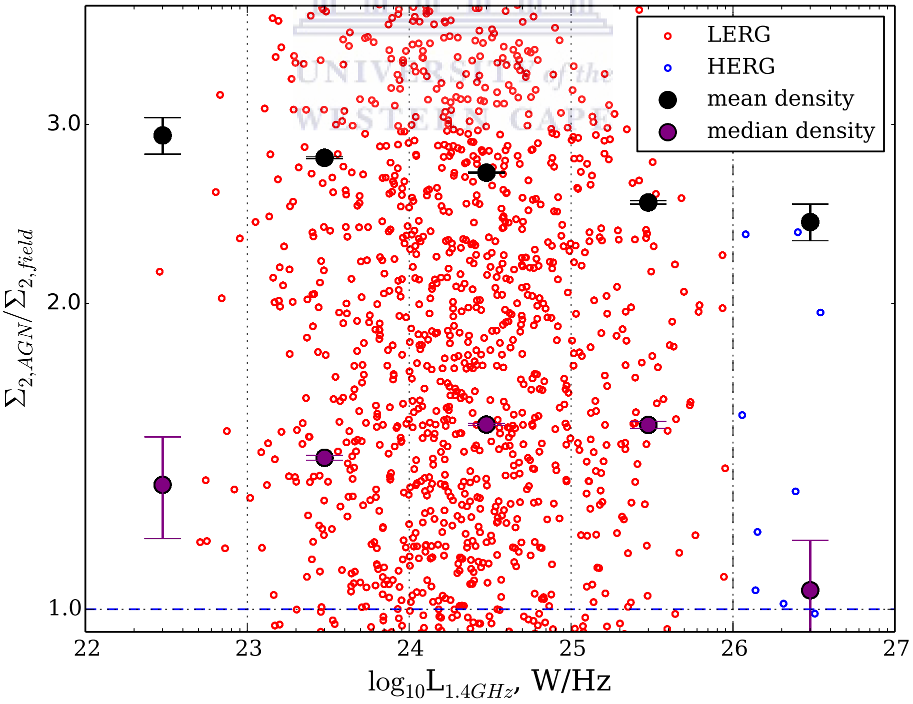

FIGURE 4.10: A magnified rendition of Fig. 4.9.

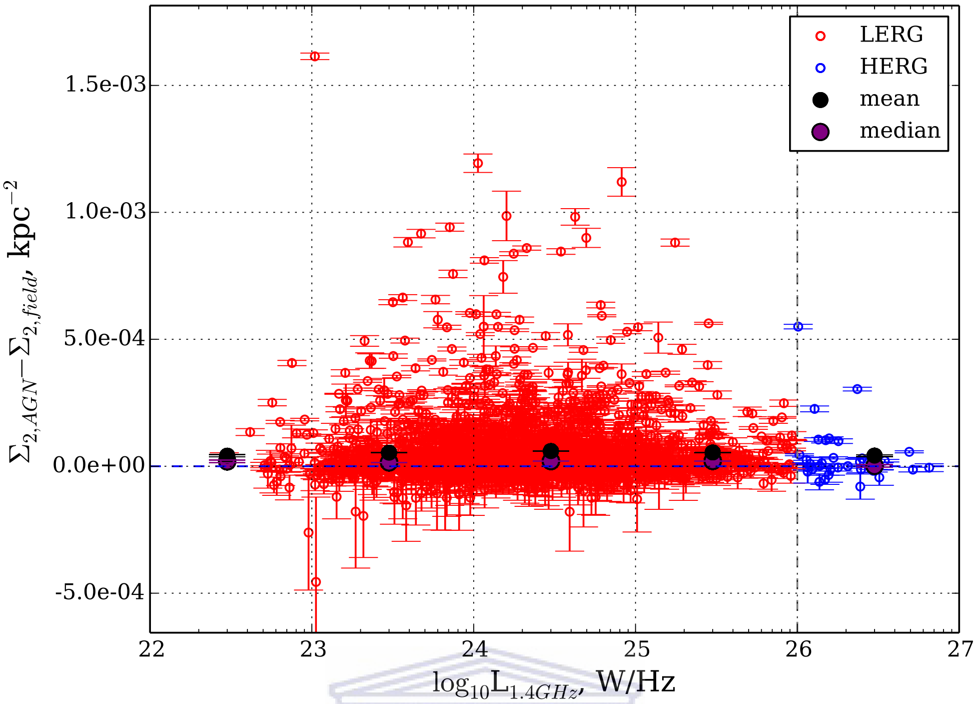

FIGURE 4.11: $\Sigma_{2,\mathrm{D}}$ as a function of $\mathrm{L}_{1.4\mathrm{GHz}}$.

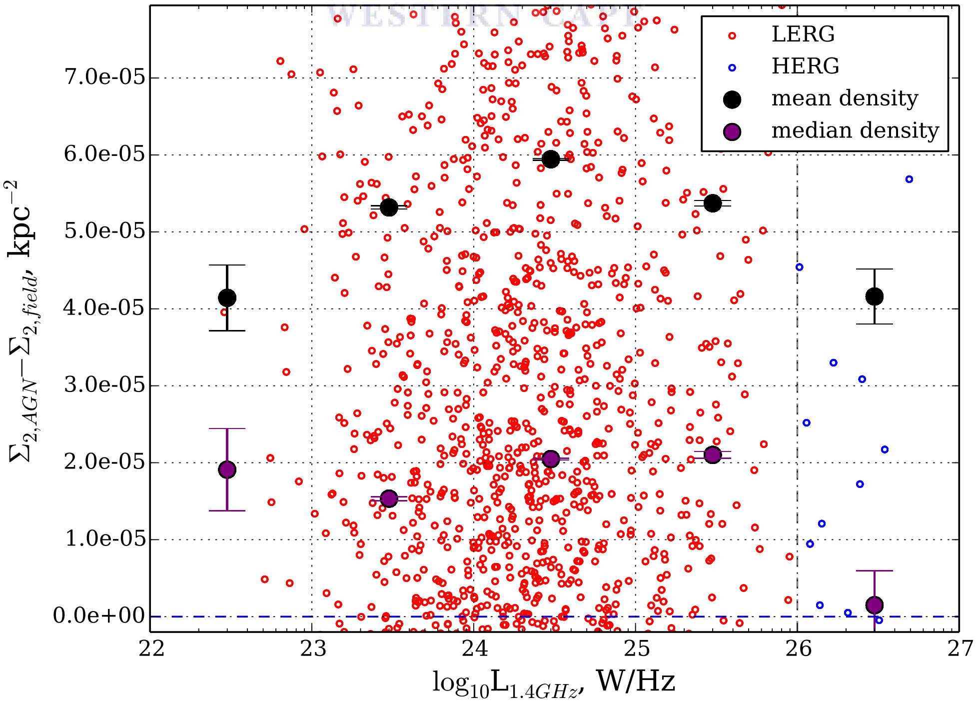

FIGURE 4.12: A magnified version of Fig. 4.11.

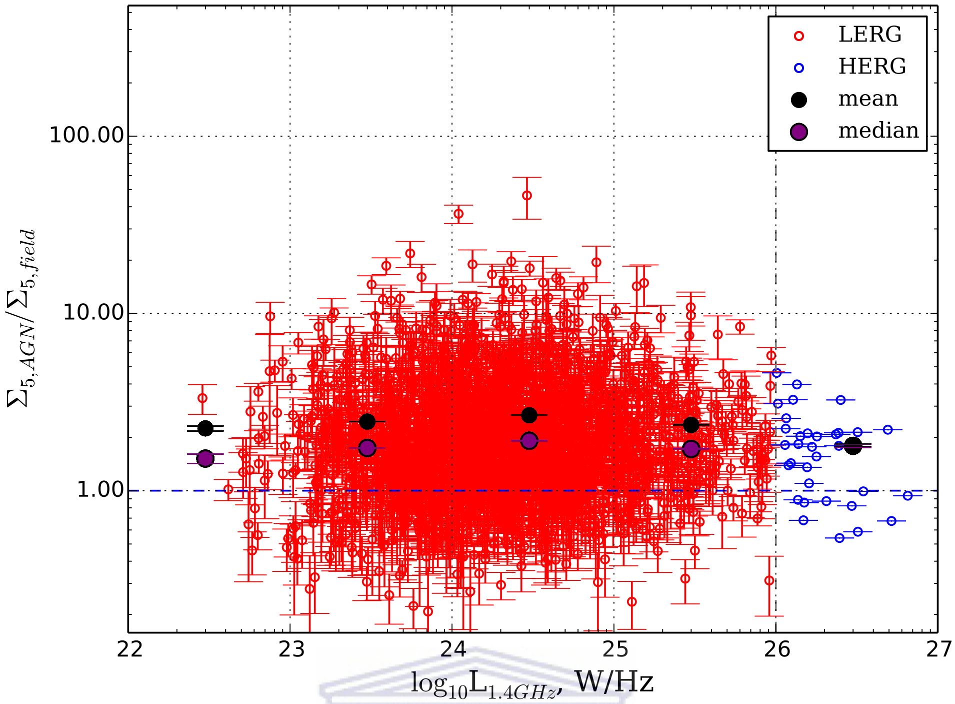

FIGURE 4.13: $\Sigma_{5,\mathrm{R}}$ as a function of $\mathrm{L}_{1.4\mathrm{GHz}}$.

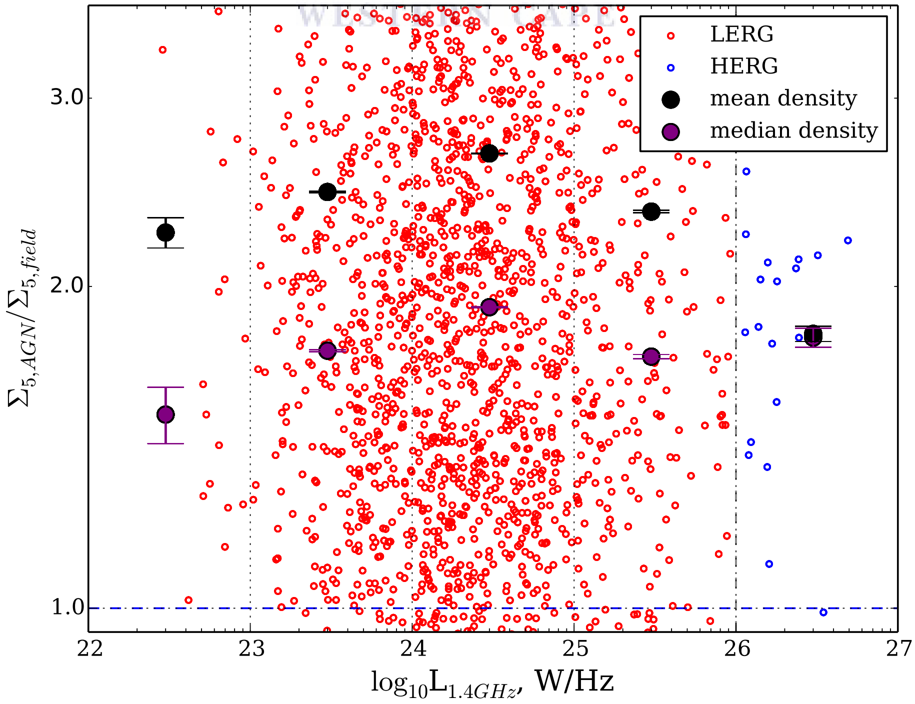

FIGURE 4.14: A magnified version of Fig. 4.13.

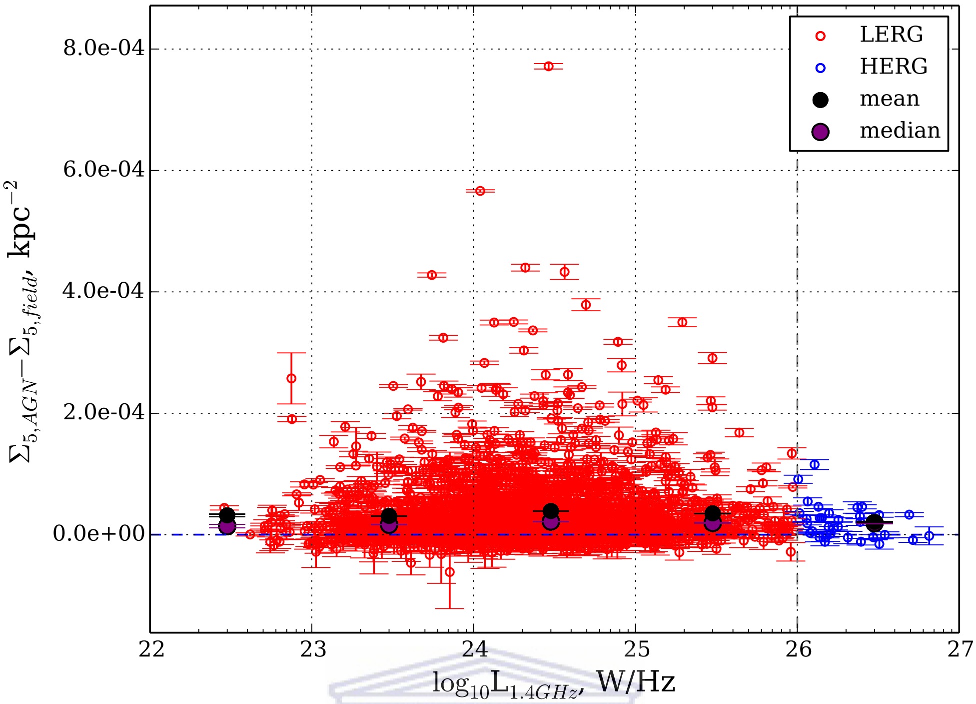

FIGURE 4.15: $\Sigma_{5,\mathrm{D}}$ as a function of $\mathrm{L}_{1.4\mathrm{GHz}}$.

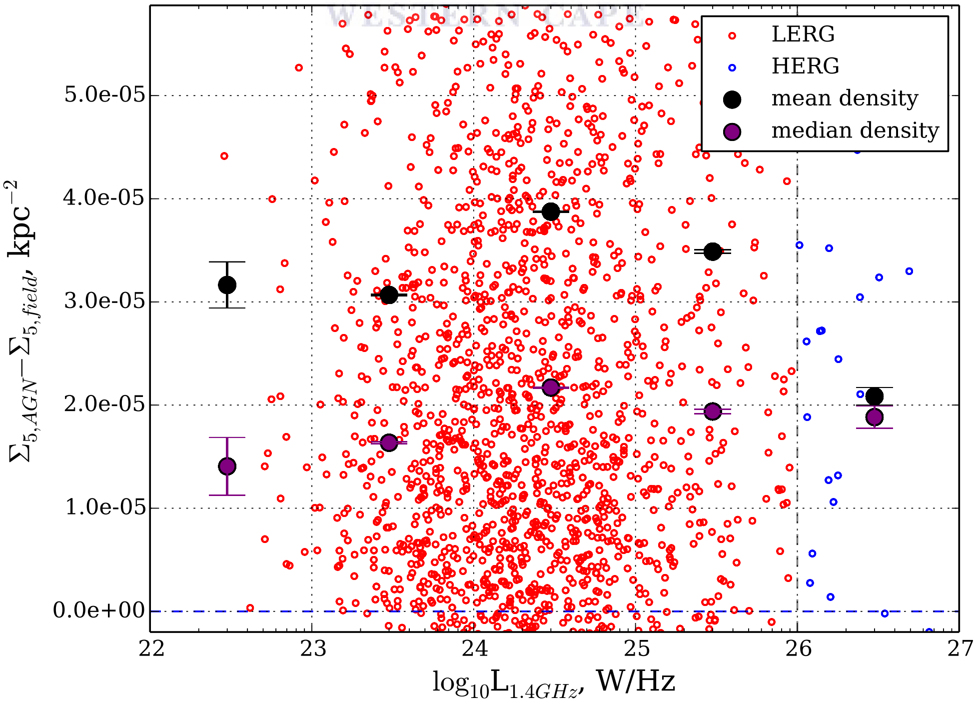

FIGURE 4.16: A magnified version of Fig. 4.15.

4.2 Discussion

Previous studies examining the role of environment on AGN have shown that the quantity of radio AGN (HERG and LERG) fractions increase with galaxy density among low-redshift radio source populations. The opposite is seen to be true for optical AGN (LINER, Seyfert and TO) (Sabater et al., 2013).

Although also considered radio AGN, HERGs are known to share characteristics with optical AGN. One of these is that they are detectable in both radio and optical wavelengths. Following the results of Sabater et al. (2013), we should thus expect the HERG fraction to increase with decreasing density. On the other hand, LERGs are only detectable in the radio continuum due to weak spectral features (Heckman and Best, 2014). LERGs, like radio AGN, have been found to favour regions where galaxy density is high (Sabater et al., 2013). If this pattern is reflected by our radio sample, we should observe a significant quantity of LERGs in environments denser than those of HERGs.

We find that our results agree with those of Sabater et al. (2013) in the low redshift interval. Based on the binned mean and median relative densities, we find that sources classified as LERGs occupy environments denser than the field in all bins except for where $L_{1.4GHz} \epsilon [10^{25}, 10^{26}]$ W/Hz. We have no results for HERGs in this interval because JVLA radio sources with $L_{1.4GHz} > 10^{26}$ W/Hz (HERGs) do not feature at all. This may be a result of HERGs simply being rare at these redshifts.

We also find, within this range, that relative mean density is not significant for $\Sigma_{2,R}$ and $\Sigma_{2,D}$ (as seen in Tables 4.1 and 4.2). Moreover, it is only marginally significant for $\Sigma_{5,R}$ but not $\Sigma_{5,D}$ (shown in Tables 4.3 and 4.4). Given that in three of the four mean density measures for $L_{1.4GHz} \epsilon [10^{25}, 10^{26}]$ W/Hz have statistics that are not significant, we can safely disregard the mean density measure in this bin.

The Spearman's rank correlation coefficients, ρ and p, are displayed in Table 4.5. The value of ρ in each case indicates a relation between density and radio-luminosity that is weak and positive. We find that $p < 0.05$ applies for $\Sigma_{5,D}$ alone, implying a valid correlation. For three of the four density measures, however, the test indicates no correlation.

These results are consistent with the idea that LERGs or low-power AGN at low redshifts occupy the densest regions. Since, all our LERG environments are denser than the field. This is consistent with Sabater et al. (2013) in which radio AGN (akin to LERGs) fractions are found to increase with density implying that radio AGN favour dense environments.

Both HERGs and LERGs exist in the intermediate redshift interval of our sample. In this interval, the binned mean and median relative densities indicate that AGN occupy regions denser than the field for $L_{1.4\mathrm{GHz}}$ ϵ $[10^{22}, 10^{27}]$ W/Hz. All relative mean densities are significant for Σ_2 and Σ_5 (as seen in Tables 4.6, 4.7, 4.8 and 4.9).

The Spearman's rank correlation test coefficients, ρ, indicate weak and positive correlations in each case (Table 4.5). The p-values suggest that the only valid correlation is for $\Sigma_{5,\mathrm{D}}$ measures. Once more, in three out of four cases, no correlation is observed.

These results are informative in a number of ways. They indicate that LERGs and HERGs, on average, reside in over-dense regions. LERGs in this interval occupy environments denser than the field consistent with low-redshift results from Sabater et al. (2013). This new finding indicates that for $z > 0.2$, HERG environments are denser than the field which contradicts the prediction that HERGs are likely to favour under-dense environments. The explanation behind this could be that HERG fractions increase with redshift which has been shown by V/V_{max} cosmic evolution tests (Best and Heckman, 2012). There is a possibility that through some quenching mechanism, HERGs evolve into LERGs. It is likely that, in the intermediate redshift interval, the HERGs we find in over-dense regions have evolved over cosmic time into LERGs that occupy the same over-dense regions at low redshifts.

The discrepancies between previous findings and our own may stem from differences in classification methods, density measures and redshift-intervals used. By classifying the sample using $L_{1.4\mathrm{GHz}} \sim 10^{26}$ W/Hz (Best and Heckman, 2012), we make a rather basic approximation of accretion-mode that should only to apply to low-redshift sources. We find that the best way to classify radio sources reliably is using equivalent widths of optical emission and ionisation lines. In this work, it appears that we have only really tested the relation between density and 1.4 GHz luminosity rather than density and the accretion-mode or the HERG-LERG dichotomy.

The spectral-line classification method is largely based on BPT diagrams (Baldwin et al., 1981). These are used to determine the AGN classes of the low-redshift radio source sample of Sabater et al. (2013) into star-forming nuclei (SFN), Seyfert galaxies, transition objects (TO – where star-forming and AGN properties are both observed), low-ionization emission regions (LINER) and passive galaxies (where star-formation has been quenched). We make the simplifying assumption that optical AGN are similar to HERGs. This is, however, insufficient without proper validation from spectral lines.

In addition to this, the radio AGN from Sabater et al. (2013) are identified up to a flux-limit of 5mJy (at z=0.1) for $L_{1.4GHz} \gtrsim 10^{23}$ W/Hz (Best et al., 2005) and classified into HERGs and LERGs. Given this flux-limit, it is likely that these sources have higher radio luminosities than those in our JVLA sample which has a flux-limit of $\sim$ 0.4mJy for $L_{1.4GHz} \gtrsim 10^{22}$. Hence, much fainter radio sources are contained in our sample. These differences in depth and flux-limit may also explain why results differ.

Differences in density measure can also contribute to discrepancies in results obtained. We have calculated surface-density up to the 2nd and 5th nearest neighbours per radio source i.e. Σ_2 and Σ_5. In Sabater et al. (2013), surface-densities, Σ_5 and Σ_{11} are obtained. It is possible for galaxy density measures in the same region to differ when measured on different scales e.g. under-dense on the kpc-scale and over-dense on the Mpc-scale. Hence, findings between studies where density has been measured different expanses may differ greatly.

In general, groups or clusters are approximately $1 - 2$ Mpc in diameter and separated at distances of $15 - 30$ h^{-1}Mpc (West, 1989). Hence, distances between galaxy groups are, on average, a factor of 10 larger than the distances between individual groups or clusters. We have shown that the parameter, N, determines the extent to which density is measured. We call the number of galaxies in a group or cluster, n. Such that when N $\geq$ n, the N^{th} nearest neighbour is likely to exist in a neighbouring galaxy meaning that the local density is not measured. Σ_N represents the galaxy density within virialised dark matter halo structures when $N \leq n$. Hence, density measured using Σ_{11} may bias densities to lower values if the average number of individual galaxies in a group are < 12. This could possibly explain some differences between our findings and those of Sabater et al. (2013).

Our measurement of density also lacks precision and would benefit from additional quantifiers. These include aperture counts, tidal-force estimation and the Voronoi volume method. Aperture counts quantifies the number of SDSS galaxies in a projected circular region on the sky. A tidal-force estimator (Verley et al., 2007) measures the magnitude of tidal forces relative to the internal binding forces for a galaxy. The Voronoi Volume counts the number of neighbouring galaxies in a sphere of finite radius centred on the target source (Cooper et al., 2005).

We do not observe a correlation between galaxy density and 1.4 GHz radio luminosity. This may be because density is perhaps being influenced by another factor within an AGN's environment. Secular processes have been suggested as a primary influencer of AGN activity in this regard Sabater et al. (2015). This may also be true for our sample, the radio AGN population residing in environments denser than the field. Since high-density regions are known to foster an abundance of diffuse, hot intra-cluster gas which may constitute the fuel supply for AGN in denser regions (Hardcastle et al., 2007). The orientation and strength of magnetic fields may also influence the measured nuclear activity (O'Sullivan et al., 2015).

Chapter 5

Conclusions

5.1 Summary and Conclusions

We used WISE photometry to examine the mid-IR properties (in the $3.4 - 22\mu$m range) of 8946 sources detected by the JVLA in the $1 - 2$ GHz range which form the radio-loud AGN sample. On WISE two-colour diagrams, HERGs are found to occupy regions that suggest the presence of dust. LERGs do not follow any discernible patterns on the two-colour plots. These results are in agreement with the prediction that HERGs have circumnuclear dust structures which WISE is able to detect.

We examined the effects of environment on a radio-loud AGN sample in SDSS Stripe 82. We did so by measuring local environments of radio AGN relative to the field by computing surface-densities (Σ_{N}) for AGN and mass and redshift matched control galaxies. This provided us with AGN and field densities that when compared (via ratios and differences) gave the relative density for each AGN. We then investigated the correlation between relative density and accretion-mode (as approximated by 1.4 GHz radio luminosity).

Environment density results indicate that at low redshift ($0.1 < z < 0.2$), low-power sources, in the $10^{22} - 10^{25}$ W/Hz range, occupy environments denser than the field sources, on average. However, we find, overall, that no correlation exists between relative density and 1.4 GHz radio luminosity.

At intermediate redshift ($0.2 < z < 1.2$), environments of the radio AGN across the full radio luminosity range probed, $10^{22} - 10^{27}$ W/Hz range are, on average, denser than the field. This is true for both HERGs and LERGs. Once more, no correlation is observed between relative density and 1.4 GHz radio luminosity.

We attribute the absence of correlations at both low and intermediate redshift intervals to the notion that local galaxy density plays only a secondary role in influencing AGN properties such as 1.4 GHz luminosity. Secular processes involving the collapse of hot intra-cluster medium gas or cold gas of origins local to the AGN play are likely to play a more significant role. Galactic-scale magnetic fields may also be more influential on nuclear activity than galaxy density.

5.2 Future Work

This study represents a starting point for what is a growing body of work that aims to chronicle the role of environment on accretion-mode classification with cosmic time. The best way to build on what has been done is to invoke optical ionisation and emission lines to classify the AGN properly. The diagnostics drawn from BPT diagrams will thus be taken into consideration in future.

We may also need an improved algorithm for identifying unique sources in the radio catalogue. The present use of PyBDSM may be insufficient for this purpose. Spurious radio noise detections in the JVLA catalogue may have been falsely identified as unique astronomical sources resulting in unwanted biases on surface-density measures.

In this work, we only make use of the surface-density parameter to estimate galaxy density. To get a more precise measure of density, we require additional methods. The more methods that are used, the better the constraint on density measurement.

Finding solutions for these issues may help improve the overall precision of our measurements. Such that when we are able to better classify and identify individual radio sources, and make use of additional density quantifiers, we will be able to study the relation between nuclear activity and environment more accurately and in greater detail.

Appendix A

Measured Quantities

A.1 Cosmological Distance

To convert angular separations on the celestial sphere to physical distances, we take cosmological expansion into account. In this work, we have made use of the WMAP 9 cosmology constants: $\mathrm{H_0} = 69.3$ km/s/Mpc, $\Omega_\mathrm{m} = 0.287$, $\Omega_\mathrm{k} = 0$ (flat universe consideration) and $\Omega_\Lambda = 0.713$ (Hinshaw et al., 2013).

A direct relation between angular separation (Θ) and physical separation (D), shown in equation A.8 (Peebles, 1993), is derived through a series of steps. This begins with equation A.1. The line-of-sight co-moving distance, $\mathrm{d_C}$, is the distance between two objects. It remains constant within a specific epoch, provided that it is small enough and both objects move with the Hubble flow (or cosmological expansion). This distance measure is obtained by integrating equation A.1 in redshift-space and multiplying the integral by the Hubble distance $\mathrm{d_H}$ defined by equation A.2. The transverse co-moving distance, $\mathrm{d_M}$, is equivalent to $\mathrm{d_C}$ for Ω_k.

To obtain the angular diameter distance, $\mathrm{d_A}$, we integrate equation A.4 (Carroll and Press, 1992). To do this, we substitute the $\mathrm{H_0 d_M}$ with $\mathrm{d_A}$ in this expression. The luminosity distance, $\mathrm{d_L}$, is defined by equation A.5 containing luminosity (L) and flux (S). With this, we obtain the angular diameter distance via equation A.7.

$$\mathrm{E(z)} \equiv \sqrt{\Omega_{\mathrm{m}}(1+\mathrm{z})^3 + \Omega_{\mathrm{k}}(1+\mathrm{z})^2 + \Omega_\Lambda} \tag{A.1}$$

$$\mathrm{d_H} = \frac{\mathrm{c}}{\mathrm{H_0}} = 3000\mathrm{h^{-1}Mpc} \tag{A.2}$$

$$\mathrm{d_c} = \mathrm{d_H} \int_0^{\mathrm{z}} \frac{dz'}{\mathrm{E(z')}} \tag{A.3}$$

$$\mathrm{H_0 d_M} = \int_0^{\mathrm{z}} [(1+\mathrm{z}')^2(1+\Omega_{\mathrm{m}}\mathrm{z}') - \mathrm{z}'(2+\mathrm{z}')\Omega_\Lambda]^{-1/2}\mathrm{dz}' \tag{A.4}$$

$$\mathrm{d_L} = \sqrt{\frac{\mathrm{L}}{4\pi \mathrm{S}}} \tag{A.5}$$

$$\mathrm{d_A} = \frac{\mathrm{H_0}}{c}\mathrm{d_m} \tag{A.6}$$

$$\mathrm{d_L} = \mathrm{d_A}(1+\mathrm{z})^2 \tag{A.7}$$

In this work, all distances are represented by $\mathrm{d_L}$. In Euclidean space, the physical separation (D) is related to angular separation by equation A.8. Combining equations A.7 and A.8 yields equation A.9. This provides a direct way of converting angular separations to physical distances which takes cosmological expansion into account.

$$\mathrm{D} = \mathrm{d_A}\Theta \tag{A.8}$$

$$\mathrm{D} = \frac{\mathrm{d_L}}{(1+\mathrm{z})^2}\Theta \tag{A.9}$$

The frequency-dependent luminosity, L_ν, is affected by redshift via bandwidth-smearing. This refers to the broadening of wavelength bands with increasing redshift. The result of this is a decrease in total luminosity per frequency bin. Flux is measured in the observational frame of reference and L_ν is intrinsic to a source and emitted in the source frame. The difference between emitted and observation frames makes it necessary to apply a k-correction along the line-of-sight. This is accomplished by introducing a factor of (1+z) to the relation between luminosity and flux. Doing this leads to the k-corrected luminosity in equation A.10 where observed and emitted frequencies are denoted by ν_e and ν_o, respectively (Hogg, 2000).

$$\mathrm{L}_\nu(\nu_\mathrm{e}) = \frac{4\pi \mathrm{d}_\mathrm{L}^2}{(1+\mathrm{z})}\mathrm{S}_\nu(\nu_\mathrm{o}) \tag{A.10}$$

A.2 Error Analysis

We quantify the error on the mean or standard error (SE) via equation A.12). This is defined as the standard deviation (equation A.11) in a sample, weighted by $\sqrt{\mathrm{N}}$ with N being the number of data points within the sample. The symbols, <>, denotes an average of the enclosed parameter.

$$\sigma = \sqrt{<\mathrm{x}^2> - <\mathrm{x}>^2} \tag{A.11}$$

$$\mathrm{SE} = \frac{\sigma}{\sqrt{\mathrm{N}}} \tag{A.12}$$

We propagate errors using equations A.14 and A.13 for sums i.e. $X = a + b + ... + n$ and products i.e. $X = a^\alpha b^\beta ... n^\gamma$, respectively.

$$\sigma_\mathrm{X}^2 = \sigma_\mathrm{a}^2 + \sigma_\mathrm{b}^2 + ... + \sigma_\mathrm{n}^2 \tag{A.13}$$

$$\left(\frac{\sigma_{\mathrm{X}}}{\mathrm{X}}\right)^2 = \alpha^2\left(\frac{\sigma_{\mathrm{a}}}{\mathrm{a}}\right)^2 + \beta^2\left(\frac{\sigma_{\mathrm{b}}}{\mathrm{b}}\right)^2 + ... + \gamma^2\left(\frac{\sigma_{\mathrm{n}}}{\mathrm{n}}\right)^2 \quad \text{(A.14)}$$

Appendix B

Neighbour Search and Cross-match Tools

We make frequent use of Starlinks Table Infrastructure Library Tool Set (Stilts) Taylor (2015a) in this work. Stilts is a Java library containing a set of command-line tools designed to perform specific functions on data tables or catalogue. One of these is functions the cross-matching of catalogues.

An example of a Stilts command which is used to determine nearest-neighbour match-groups for radio sources in the JVLA-SDSS sample is as follows:

```
java -jar -Xmx16384m ../topcat_\&_stilts/stilts.jar tskymatch2
ifmt1=’ascii’ ifmt2=’fits’
omode=out
out=’../stripe82_SDSS/agn/stilts_search_ukidss/20as_agn_search_results.txt’
ofmt=’ascii’ ra1=’ra’ dec1=’dec’ ra2=’ra’ dec2=’dec’
error=20 tuning=16 join=1and2 find=all
in1=’../stripe82_UKIDSS/s82_vla_sdss_ukidss.txt’
in2=’../SDSS_photoz/sdss_coadd_glxs_v12.04_all.fit.txt’
```

In general, a command like this invokes the use of `java` because Stilts based on a java library. The flag `jar` is set to specify that the programme’s source is a JAR file. We also flag `-Xmx16384m` to increase the heap memory used by the programme. In this example, we allocate 2^{14} MB or 16.384 GB heap memory. What follows is the file-path of the Stilts JAR file.

The tool we use here is `tskymatch2` and requires input formats e.g. ASCII, VOTable, FITS etc (`ifmt`) for the two tables being cross-matched. The parameter `omode` writes a new table containing the results of a cross-match. These results are written into a file specified under the name, `out`. The format of the output table is given under `ofmt`.

Co-ordinate, right-ascension (ra) and declination (dec) in tables 1 and 2 are assigned under `ra1`, `dec1` and `ra2`, `dec2`, respectively. Pixel-size for binning rows during the matching process is determined under `tuning`. The higher this value, the more detailed the cross-match method and also, the greater the memory and power of computational resourced used to complete the cross-match.

The `error`, in arcseconds ($''$), is the search-cone radius (SCR). The parameter, `join` defines which tables should be matched. The matching method is defined by `find`. In this example, we combine tables 1 and 2. We want the programme to search for `all` possible matches to each source in table 1 within circular areas centred on each source in table 1 that have radii equivalent to the angular size or `error`.

Input tables are denoted by `in1` for table 1 and `in2` for table 2. This numbering is kept consistent throughout the command i.e. `in1` is associated with the parameters, `ra1` and `dec1` as is `in2` with `ra2` and `dec2`

We can display catalogued data using a programme called Topcat (Taylor, 2015b). It is Java plugin that interpolates table data into diagrams among other functions. Some of these include performing calculations on tabulated data, plotting and cross-matching catalogues. Topcat differs in that it runs via a graphical user interface (GUI) rather than via a command-line.

Appendix C

Computing the Surface-density Parameter

We compute the surface-density parameter, $\Sigma_{\rm N}$, using a sequence of steps. This involves the use of Python, Topcat and Stilts. A brief outline of our method is as follows:

- The JVLA-SDDS-UKIDSS combined catalogue form the AGN sample. The control sample consists of all SDSS-UKIDSS galaxies matched in M_* and z to the AGN. We implement this control galaxy search in Python. These two steps yield the AGN and control samples.

- We run a neighbour-search in SDSS for each source in the AGN and control catalogues. The output is a table containing groups of neighbouring SDSS sources for all AGN and control galaxies.

- A Python script groups the tabulated results by AGN for the AGN sample. Because an AGN may have between $2-10$ control galaxies, results are grouped first by AGN and then by control galaxy on the control sample.

- For each group of neighbouring sources, the $\rm N^{th}$ nearest source is identified. This is given as an angular distance in arcseconds ($''$) and then converted to a physical distance in kpc. This $\rm N^{th}$ nearest distance ($\rm d_N$) is then expressed as $\Sigma_{\rm N}$. Surface-density for each

AGN gives the AGN density $\Sigma_{\mathrm{N,agn}}$. The average Σ_{N} over each set of controls associated with an AGN yields the field density for that AGN i.e. $\Sigma_{\mathrm{N,field}}$.

- Using a Python script, we write these surface-densities into two separate text files (one each for the AGN and control samples) with the 19-digit unique SDSS identifier for each AGN. This helps match the surface-densities so that the ratios and differences of $\Sigma_{\mathrm{N,agn}}$ and $\Sigma_{\mathrm{N,field}}$ can be calculated to obtain the relative galaxy density we consider as the galaxy density measure for the AGN.

Bibliography

M. Aaronson, J. Huchra, and J. Mould. The Infrared Luminosity/HI Velocity-width Relation and its Application to the Distance Scale. *The Astrophysical Journal*, 229: 1–13, 1979.

M.A. Abramowicz. Foundations of Black Hole Accretion Disk Theory. *Living Reviews in Relativity*, 16:1–89, 2013.

R. Antonucci. Unified Models for Active Galactic Nuclei and Quasars. *Annual Review of Astronomy and Astrophysics*, 31:473–521, 1993.

R.R.J. Antonucci and J.S. Miller. Spectropolarimetry and the Nature of NGC 1086. *The Astrophysical Journal*, 297:621–632, 1985.

B.D. Asabere, C. Horellou, H. Winkler, T. Jarrett, and L. Leeuw. Dust in the radio galaxy and merger remnant NGC 1316 (Fornax A). *arXiv*, 2014.

W. Baade and R. Minkowski. Identification of radio sources in Cassiopeia, Cygnus A, and Puppis A. *The Astrophysical Journal*, 119:206–227, 1954.

J.A. Baldwin, M.M. Phillips, and R. Terlevich. Classification parameters of the emission line spectra of extragalactic objects. *Publications of the Astronomical Society of the Pacific*, 93:5–19, 1981.

P. Barai, M. Viel, G. Murante, M. Gaspari, and S. Borgani. Kinetic or thermal AGN feedback in simulations of isolated and merging disc galaxies calibrated by the M-σ relation. *Monthly Notices for the Royal Astronomical Society*, 437:1456–1475, 2014.

J.E. Barnes and L.E. Hernquist. Fueling Startburst Galaxies with Gas-rich Mergers. *The Astrophysical Journal*, 370:L65–L68, 1991.

R.H. Becker, R.L. White, and D.J. Helfand. The VLA's FIRST Survey. In *ASP Conference Series Astronomical Data Analysis Software and Systems III*, volume 61, page 165, 1994.

P.N. Best. The environmental dependence of radio-loud AGN activity and star formation in the 2dFGRS. *Monthly Notices for the Royal Astronomical Society*, 351:70–82, 2004.

P.N. Best and T.M. Heckman. On the fundamental dichotomy in the local radio-AGN population: accretion, evolution and host galaxy properties. *Monthly Notices for the Royal Astronomical Society*, 421:1569–1582, 2012.

P.N. Best, G. Kauffmann, T.M. Heckman, J. Brinchmann, S. Charlot, et al. The host galaxies of radio-loud active galactic nulcei: mass dependences, gas cooling and active galactic nuclei feedback. *Monthly Notices for the Royal Astronomical Society*, 362: 25–40, 2005.

R.D. Blandford and M.J. Rees. A 'twin-exhaust' model for double radio sources. *Monthly Notices for the Royal Astronomical Society*, 169:395–415, 1974.

V. Buat, A. Boseli, G. Gavazzi, and C. Bonfanti. Star formation and dust extinction in nearby star-forming and starburst galaxies. *Astronomy & Astrophysics*, 383:801–812, 2002.

G.R. Burbidge. *Paris Symposium on Radio Astronomy*. Stanford University Press, 1959.

S. Buttiglione and Alessandro Capetti. Optical Spectrscopy of 3CR Sources: Accretion and Jet launching in Radio Galaxies. *ASP Conferences Series, Accretion and Ejection in AGNs: A Global View*, 427, 2010.

S. Buttiglione, A. Capetti, A. Celotti, D. J. Axon, M. Chiaberge, F. D. Macchetto, and W. B. Sparks. An optical spectroscopic survey of the 3CR sample of radio galaxies with z $<$ 0.3: II. Spectroscopic classes and accretion modes in radio-loud AGN. *Astronomy & Astrophysics*, 509:A6, 2010.

S.M. Carroll and W.H. Press. The cosmological constant. *Annual Review of Astronomy and Astrophysics*, 30:499–542, 1992.

M. Cisternas, K. Jahnke, K.J. Inskip, J. Kartaltepe, A.M. Koekemoer, et al. The Bulk of the Black Hole Growth Since z $\sim$ 1 Occurs in a Secular Universe: No Major Merger-AGN connection. *The Astrophysical Journal*, 726:57–71, 2011.

J.J. Condon. Confusion and Flux-Density Error Distributions. *The Astrophysical Journal*, 188:270–286, 1974.

J.J. Condon, W.D. Cotton, E.W. Gresisen, Q.F. Yin, R.A. Perley, G.B. Taylor, and J.J. Broderick. The NRAO VLA Sky Survey. *The Astronomical Journal*, 115:1693–1716, 1998.

M.C. Cooper, J.A. Newman, D.S. Madgwick, B.F. Gerke, R. Yan, and M. Davis. Measuring Galaxy Environments with Deep Redshift Surveys. *The Astrophysical Journal*, 634:833–848, 2005.

R. Coziol and I. Plauchu-Frayn. Evidence for Tidal Interactions and Mergers as the Origin of Galaxy Morphology Evolution in Compact Groups. *The Astronomical Journal*, 133: 2630–2642, 2007.

B. Czerny, R. Goosmann, V. Karas, and G. Ponti. Radio Quiet AGN. *arXiv*, 2005.

E.A. Dibai. Mass of the central bodies of active galactic nuclei. *Soviet Astronomy Letters*, 3:1–3, 1977.

A. Dominguez, B. Siana, A.L. Henry, C. Scarlata, A.G. Bedregal, M. Malkan, et al. Dust excitation from Balmer decrements of star-formation galaxies at $0.75 \leq z \leq 1.5$ with Hubble Space Telescope/Wide-Field-Camera 3 spectroscopy from the WFC3 infrared spectrsoscopic parallel survey. *The Astrophysical Journal*, 763:145–155, 2013.

A. Dressler. Galaxy Morphology in Rich Clusters; Implications for the Formation and Evolution of Galaxies. *The Astrophysical Journal*, 236:351–365, 1980.

A. Einstein. Does the inertia of a body depend upon its energy content? *The Astronomical Journal*, 18 (13):639–641, 1905.

Sara L. Ellison, David R. Patton, J. Trevor Mendel, and Jillian M. Scudder. Galaxy pairs in the Sloan Digital Sky Survey – IV. interactions trigger active galactic nuclei. *Monthly Notices for the Royal Astronomical Society*, 418:2043–2053, 2011.

S.L. Ellison, D.R. Patton, and R.C. Hickox. Galaxy pairs in the Sloan Digital Sky Survey - XII: The fuelling mechanism of low excitation radio-loud AGN. *Monthly Notices for the Royal Astronomical Society*, 451:L35–L39, 2015.

R. Farouki and S.L. Shapiro. Computer Simulations of Environmental Influences on Galaxy Evolution in Dense Clusters. II. Rapid Tidal Encounters. *The Astrophysical Journal*, 243:32–41, 1981.

C.M. Gaskell and E.S. Klimek. Variability of Active Galactic Nuclei from the Optical to X-ray Regions. *Astronomical and Astrophysical Transactions*, 22:4–5, 2003.

G. Gavazzi. Colours, Luminosities and Masses of Disk Galaxies. *The Astrophysical Journal*, 419:469–478, 1993.

Gabriele Ghisellini. Radiative Processes in High Energy Astrophysics. *arXiv*, 2012.

G. Gürkan, M.J. Hardcastle, and M.J. Jarvis. The Wide-field Infrared Survey Explorer properties of complete samples of radio-loud active galactic nucleus. *Monthly Notices for the Royal Astronomical Society*, 438:1149–1161, 2014.

M. J. Hardcastle, D. A. Evans, and J. H. Croston. Hot and cold gas accretion and feedback in radio-loud active galaxies. *Monthly Notices for the Royal Astronomical Society*, 376: 1849–1856, 2007.

M. J. Hardcastle, J. H. Y. Ching, J. S. Virdee, M. J. Jarvis, S. M. Croom, et al. Herschel-ATLAS/GAMA: a difference between star formation rates in strong-line and weak-line radio galaxies. *Monthly Notices for the Royal Astronomical Society*, 429:2407–2424, 2013.

T.M. Heckman and P.N. Best. The Coevolution of Galaxies and Supermassive Black holes: Insights from Surveys of the Contemporary Universe. *arXiv*, 2014.

P. D. Herbert, M. J. Jarvis, C. J. Willott, R. J. McLure, E. Mitchell, et al. Evidence of different star formation histories for high- and low-luminosity radio galaxies. *Monthly Notices for the Royal Astronomical Society*, 406:1841–1847, 2010.

I. Heywood, M.J. Jarvis, A.J. Baker, K.W. Bannister, C.S. Carvalho, M. Hardcastle, et al. A deep/wide 1–2 GHz snapshot survey of SDSS Stripe 82 using the Karl G. Jansky Very Large Array in a compact hybrid configuration. *arXiv*, 2016.

G. Hinshaw, D. Larson, E. Komatsu, D. N. Spergel, C. L. Bennett, et al. Nine-year Wilkinson Microwave Anisotropy Probe (WMAP) Observation: cosmological parameter results. *The Astrophysical Journal Supplement Series,*, 208:19–3 p, 2013.

David W. Hogg. Distance Measures in Cosmology. *arXiv*, 2000.

D.W. Hogg. Confusion Errors in Astrometry and Counterpart Association. *The Astronomical Journal*, 120:1207–1213, 2001.

H.S. Hwang, C. Park, D. Elbaz, and Y.Y. Choi. Activity in galactic nuclei of cluster and field galaxies in the local universe. *Astronomy & Astrophysics*, 538:A15, 2012.

W. Ishibashi and T.J.-L. Courvoisier. Synchrotron radio emission in radio-quiet AGNs. *Astronomy & Astrophysics*, 525:A118, 2011.

N. Jackson and S. Rawlings. [OIII] 500.7 spectroscopy of 3C galaxies and quasars at redshift z > 1. *Monthly Notices for the Royal Astronomical Society*, 286:241–256, 1997.

W. Jaffe, K. Meisenheimer, H.J.A. Röttgering, Ch. Leinert, A. Richichi, O. Chesneau, et al. The central dusty torus in the active nucleus of NGC 1068. *Letters to Nature*, 429:47–49, 2004.

R.M.J. Janssen, H.J.A.Röttgering, P. N. Best, and J. Brinchmann. The triggering probability of radio-loud AGN: A comparison of high and low excitation radio galaxies in hosts of different colors. *Astronomy & Astrophysics*, 541:A62:1–7, 2012.

M. Karouzos, M. J. Jarvis, and D. Bonfield. Mergers as triggers for nuclear activity: a near-IR study of the close environment of AGN in the VISTA-VIDEO survey. *Monthly Notices for the Royal Astronomical Society*, 439:861–877, 2014.

K.I. Kellerman, R. Sramek, M. Schmidt, D.B. Shaffer, and R. Green. VLA Observations of Objects in the Palomar Bright Quasar Survey. *The Astronomical Journal*, 98:119–132, 1989.

G. A. Khorunzhev, S. Yu. Sazonov, R. A. Burenin, and A. Yu. Tkachenko. Masses and accretion rates of supermassive black holes in active galactic nuclei from the integral survey. *arXiv*, 2012.

D.D. Kocevski, S.M. Faber, M. Mozena, A.M. Koekemoer, Kirpal Nandra, Cyprian Rangel, et al. Candels: Constraining the AGN–Merger Connection with Host Morphologies at z∼2. *The Astrophysical Journal*, 744:148–157, 2012.

R.A. Laing, C. R. Jenkins, J. V. Wall, and S.W. Unger. Spectrophotometry of a Complete Sample of 3CR Radio Sources: Implications for Unified Models. In *ASP Conference Series, The First Stromlo Symposium: The Physics of Active Galaxies*, volume 54, page 201, 1994.

A. Lawrence, S. J. Warren, O. Almaini, A. C. Edge, N. C. Hambly, R. F. Jameson, et al. The UKIRT Infrared Deep Sky Survey UKIDSS. *Monthly Notices for the Royal Astronomical Society*, 379:1599–1617, 2007.

B. Liu, R.E. Taam, E. Qiao, and Y. Weimin. Coronal Accretion: the origin of X-ray Emission in AGN. In *The Proceedings of the IAU 8th Asian-Pacific Regional Meeting*, 2015.

B.F. Liu, S. Mineshige, E. Meyer-Hofmeister, and T. Kawaguchi. Two-Temperature Coronal Flow above a Thin Disk. *The Astrophysical Journal*, 575:117–126, 2002.

N. Malavasi, S. Bardelli, P. Ciliegi, O. Ilbert, L. Pozzetti, and E. Zucca. The environment of radio sources in the VLA-COSMOS survey field. *Astronomy & Astrophysics*, 576: A101, 2015.

L.H. Manzer and M.M. De Robertis. The Effects of the Local Environment on Active Gaclactic Nuclei. *The Astrophysical Journal*, 788:140–156, 2014.

R.E. Mason. Dust in the Torus of the AGN Unified Model. *arXiv*, 2014.

S. Mateos, A. Alonso-Herrero, F. J. Carrera, A. Blain, M. G. Watson, et al. Using the Bright Ultrahard XMM–Newton survey to define an IR selection of luminous AGN based on WISE colours. *Monthly Notices for the Royal Astronomical Society*, 426: 3271–3281, 2012.

T. Mauch and E.M. Sadler. Radio sources in the 6dFGS: local luminosity functions at 1.4 GHz for star-forming galaxies and radio-loud AGN. *Monthly Notices for the Royal Astronomical Society*, 375:931–950, 2007a.

T. Mauch and E.M. Sadler. Radio sources in the 6dFGS: local luminosity functions at 1.4 GHz for star-forming galaxies and radio-loud AGN. *Monthly Notices for the Royal Astronomical Society*, 375:931–950, 2007b.

A. Merloni, S. Heinz, and T. Di Matteo. A Fundamental Plane of black-hole activity. *Monthly Notices for the Royal Astronomical Society*, 345:1057–1076, 2003.

C.J. Miller, R.C. Nichol, P.L. Gómez, A.M. Hopkins, and M. Bernardi. The Environment of Active Galactic Nuclei in the Sloan Digital Sky Survey. *The Astrophysical Journal*, 597:142–156, 2003.

N. Mohan and D. Rafferty. PyBDSM: Python Blob Detection and Source Measurement, 2015.

R.D.A. Newton and S.T. Kay. A study of AGN and supernova feedback in simulations of isolated and merging disc galaxies. *Monthly Notices for the Royal Astronomical Society*, 434:3606–3627, 2013.

S. P. O'Sullivan, B. M. Gaensler, S. van Velzen M. A. Lara-L'opez and, J. K. Banfield, et al. The Magnetic Field and Polarization Properties of Radio galaxies in different accretion states. *The Astrophysical Journal*, 806:83–100, 2015.

F. Panessa, X. Barcons, L. Bassani, M. Cappi, F. J. Carrera, et al. The X-ray and radio connection in low-luminosity active nuclei. *Astronomy & Astrophysics*, 467:519–527, 2007.

C. Park and Y.Y. Choi. Combined effects of galaxy interactions and large-scale environment on galaxy properties. *The Astrophysical Journal*, 691:1828–1845, 2009.

P. J. E. Peebles. *Principles of Physical Cosmology.* Princeton University Press, 1993.

R. Perley. The jansky very large array – new capabilities, new science, 2013.

S. Rawlings and R. Saunders. Evidence for a common central-engine mechanism in all extragalactic radio sources. *Nature*, 349:138–140, 1991.

R.R.R. Reis, M. Soares-Santos, J. Annis, S. Dodelson, J. Hao, D. Johnston, J. Kubo, H. Lin, H.J. Seo, and M. Simet. The Sloan Digital Sky Survey Co-add: A Galaxy Photmetric Redshift Catalog. *The Astrophysical Journal*, 747:59–70, 2012.

C.S. Reynolds. Unwrapping the X-ray Spectra of Active Galactic Nuclei. *arXiv*, 2015.

M. Ryle and A.R. Sandage. The optical identification of three new objects in the 3C 48 class. *The Astrophysical Journal*, pages 419–421, 1964.

J. Sabater, P. N. Best, and M. Argudo-Fernández. Effect of the interactions and environment on nuclear activity. *Monthly Notices for the Royal Astronomical Society*, 430: 638–651, 2013.

J. Sabater, P. N. Best, and T. M. Heckman. Triggering optical AGN: the need for cold gas, and the indirect roles of galaxy environment and interactions. *Monthly Notices for the Royal Astronomical Society*, 447:110–116, 2015.

Peter Schneider. *Extragalactic Astronomy and Cosmology: An Introduction*. Springer, 2006.

SDSS. Glossary - sdss dr7. http://classic.sdss.org/dr7/shared_images/sdssgeom.jpg, 2007a. Accessed: 2016-01-08.

SDSS. Sky coverage - sdss dr7. http://classic.sdss.org/dr7/dr7photo_big.gif, 2007b. Accessed: 2016-01-08.

Gregory A. Shields. A Brief History of AGN. *arXiv*, 1999.

J. D. Silverman, P. Kampczyk, K. Jahnke, R. Andrae, S. J. Lilly, M. Elvis, et al. The impact of Galaxy Interactions on Active Galactic Nucleus Activity in zCOSMOS. *The Astrophysical Journal*, 743:2–12, 2011.

E.P. Smith, T.M. Heckman, and G.D. Illingworth. Stellar dynamics of powerful radio galaxies. *The Astrophysical Journal*, 356:399–415, 1990.

G. Sorrentino, M. Radovich, and A. Rifatto. The environment of active galaxies in the SDSS-DR4. *Astronomy & Astrophysics*, 451:809–816, 2006.

M. Suganuma, Y. Yoshii, Y. Kobayashi, T. Minezaki, K. Enya, H. Tomita, et al. Reverbation Measurements of the Inner Radius of the Dust Torus in Nearby Seyfert 1 Galaxies. *The Astrophysical Journal*, 639:46–63, 2006.

C. N. Tadhunter, R. Morganti, A. Robinson, R. Dickson, M. Villar-Martin, and R. A. E. Fosbury. The nature of the optical–radio correlations for powerful radio galaxies. *Monthly Notices for the Royal Astronomical Society*, 298:1035–1047, 1998.

C. Tasse, P. N. Best, H. Röttgering, and D. Le Borgne. Radio-loud AGN in the XMM-LSS field II. A dichotomy in environment and accretion mode? *Astronomy & Astrophysics*, 490:893–904, 2008.

C. Tasse, H. Röttgering, and P.N. Best. The dependence of X-ray AGN activity on host galaxy properties and environment. *Astronomy & Astrophysics*, 525:A127:1–17, 2011.

Mark Taylor. Topcat, 2015a.

Mark Taylor. Stilts, 2015b.

Y. Terashima and A.S. Wilson. Chandra snapshot observations of low-luminosity active galactic nuclei with a compact radio source. *The Astrophysical Journal*, 583:145–158, 2003.

Alar Toomre and Juri Toomre. Galactic bridges and tails. *178*, 623:623–666, 1972.

E. Treister, K. Schawinski, C.M. Urry, and B.D. Simmons. Major Galaxy Mergers only Trigger the Most Luminous Active Galactic Nuclei. *The Astrophysical Journal Letters*, 758:L39–44, 2012.

C.M. Urry and P. Padovani. Unified schemes for radio-loud active galactic nuclei. *Publications o fthe Astrononical Society of the Pacific*, 107:803–845, 1996.

S. Verley, S. Leon, L. Verdes-Montenegro, F. Combes, J. Sabater, et al. The AMIGA sample of isolated galaxies, V. Quantification of the isolation. *Astronomy & Astrophysics*, 472:121–130, 2007.

M.J. West. Groups of galaxies and large scale structure. *The Astrophysical Journal*, 344: 535–542, 1989.

E.L. Wright, P.R.M. Eisenhard, A.K. Mainzer, M.E. Ressler, R.M. Cutri, T. Jarrett, et al. The Wide-Field Infrared Survey Explorer (WISE): Mission Description and Initial On-orbit Performance. *The Astronomical Journal*, 140:1868–1881, 2010.

D.G. York, J. Adelman, J.E. Anderson Jr., S.F. Anderson, J. Annis, et al. The Sloan Digital Sky Survey: Technical Summary. *arXiv*, 2000.